Fall 2018

Modeling of air entrainment and oxide inclusion formation during pouring of metal castings

Seyyed Hojjat Majidi
University of Iowa

MODELING OF AIR ENTRAINMENT AND OXIDE INCLUSION FORMATION DURING POURING OF METAL CASTINGS

by

Seyyed Hojjat Majidi

A thesis submitted in partial fulfillment
of the requirements for the Doctor of
Philosophy degree in Mechanical Engineering
in the Graduate College of
The University of Iowa

December 2018

Thesis Supervisor: Professor Christoph Beckermann

Graduate College
The University of Iowa
Iowa City, Iowa

CERTIFICATE OF APPROVAL

_____

Ph.D. THESIS

_____

This is to certify that the Ph.D. thesis of

Seyyed Hojjat Majidi

has been approved by the Examining Committee for the thesis requirement for the Doctor of Philosophy degree in Mechanical Engineering at the December 2018 graduation.

Thesis Committee:

_____
Christoph Beckermann, Thesis Supervisor

_____
H.S. Udaykumar

_____
Pablo M. Carrica

_____
James H.J. Buchholz

_____
Corey D. Markfort

To My Lovely Family

ACKNOWLEDGEMENTS

First and foremost, I would like to express my sincere gratitude to my academic adviser, Professor Christoph Beckermann, for his valuable guidance and precious comments. The thesis would not have come to a successful completion without his help and continuous support. Also my sincere thanks go to my thesis committee members, Professor Udaykumar, Professor Carrica, Professor Buchholz, and Professor Markfort for their time and insightful comments on my dissertation.

I would like to extend my gratitude to Dr. Marc Schneider and the software development team at MAGMAsoft for their support and collaboration in my research.

I would also like to thank my dear friends at the Solidification Lab for all their help and encouragement. We had great discussions and fun times during the past years.

Last but not the least, I would like to thank my wonderful family. I owe a lot to my devoted parents, Jamileh and Reza, my sister and my brother, for their spiritual and unconditional support throughout my study at the University of Iowa and during my entire life.

Thank you all!

ABSTRACT

Oxide inclusions are among the most commonly reported defects in ferrous and non-ferrous castings. They affect the surface quality, machinability, and mechanical performance of a cast part. Air entrainment during mold filling is the main source of the oxygen that is consumed in inclusion formation. A quantitative understanding of the formation mechanisms or the prediction of final amounts and locations of oxide inclusions in metal castings is not available. Ductile iron experiments are conducted to study the formation of oxide inclusions during pouring. Oxide inclusions are measured by serial sectioning of the solidified castings. The effect of different gating systems, section thicknesses, and surface orientations on the inclusion formation and final distribution is studied. In addition, a computational model is developed for predicting the formation, motion and final location of oxide inclusions during pouring of metal castings, with the focus on the important mechanism of generation of oxide inclusions due to air entrainment during mold filling. The developed model calculates the local air entrainment rate as a function of the turbulent kinetic energy and the magnitude of the normal velocity gradient of the liquid metal at the liquid-air interface. The turbulent kinetic energy is estimated from the sum of the squares of the fluctuating velocity components relative to a spatially averaged mean velocity. The air entrainment model is implemented in a casting simulation software and validated by comparing its predictions to experimental air entrainment measurements for a circular water jet plunging into a quiescent pool. The liquid velocity, diameter and the turbulence intensity dependence is determined by a single entrainment coefficient. Oxide inclusions are then generated at the liquid-air interface, transported with the melt flow under the combined influences of drag and buoyancy, and captured by the solidifying casting surface. The developed model provides a powerful technique for predicting the oxide inclusion formation and final location.

The air entrainment model is validated with water modeling experiments. Water modeling experiments are useful in understanding the effect of pouring conditions and gating system designs on the characteristics of the liquid metal flow, consequently air entrainment. The predictions compare favorably with the experimental measurements. The model capabilities are then demonstrated by simulating the flow in typical casting filling systems and calculating the air entrainment rates. The results reveal how pouring conditions and gating system designs affect the oxide inclusion formation. Results show that producing clean castings requires reducing the turbulence intensity, head height and the pouring time during mold filling.

PUBLIC ABSTRACT

Cast metals have wide range of applications from heavy equipment to aerospace and automotive industries. Defects affect the mechanical properties of the casting and may cause repair or rejection of the cast part. Oxide inclusions are among the most frequently reported casting defects. Air entrainment is the major source of oxide inclusion formation during pouring of metal castings. In this study, a computational model is developed to predict the air entrainment and oxide inclusion formation during mold filling. The model capabilities are shown by simulating the flow in typical casting filling systems and calculating the air entrainment rates. The computer simulation model developed in this study is a powerful technique to evaluate different gating designs and pouring parameters before the first casting is poured.

TABLE OF CONTENTS

LIST OF TABLES

LIST OF FIGURES

LIST OF NOMENCLATURE

A	area (m^2)
C	constant (-)
C_1	non-dimensional constant (-)
d	diameter (m)
$\boldsymbol{F}$	force vector
f	frequency (Hz)
Fr	Froude number ($=u/\sqrt{gd}$)
g	gravitational acceleration ($m\ s^{-2}$)
H	head height (m)
h	falling height (m)
I	turbulence intensity (-)
k	turbulent kinetic energy ($m^2\ s^{-2}$)
L	length (m)
l	characteristic length (m)
M	molecular weight ($g\ mol^{-1}$)
m	mass (g)
P	pressure (Pa)
q	volumetric flow rate per unit interfacial area ($m\ s^{-1}$)
Q	volumetric flow rate ($m^3\ s^{-1}$)
$\overline{\mathrm{R}}$	gas constant (= 8.314×10^6 $J\ mol^{-1}\ K^{-1}$)
Re	Reynolds number ($=\rho ud/\mu$)
r, R	radius (m)
T	temperature (K)
t	time (s)
u	velocity ($m\ s^{-1}$)

$\boldsymbol{u}$	velocity vector
u'	fluctuation velocity (m s^{-1})
V	volume (m^3)
We	Weber number ($=\rho u^2 d / \sigma$)
x	mass fraction (-)
$\boldsymbol{x}$	position vector
y	mole fraction (-)
α	volume fraction (-)
δ	disturbance size (m)
μ	dynamic viscosity (kg m s^{-1})
ρ	density (kg m^{-3})
σ	surface tension (m^3)
ω	angular frequency (rad s^{-1})

Subscripts

a	air
agg	agglomeration
b	bubble
bs	sprue base
cnv	conversion
cr	critical
cup	pouring cup
e	eddy
ent	entrainment
f	friction
fill	filling
gen	generation

in	ingate
inc	inclusion
inc,N	new generated inclusion
j	liquid jet at impact
l	liquid, ladle
liq	liquidus
n	normal
N	nozzle
N,eff	effective at nozzle exit
N,th	theoretical at nozzle exit
NE	nozzle extension
$pour$	pouring
r	runner
s	interfacial, steel
sm	Sauter mean
so	stopper opening
$sprue$	sprue
w	water
x , y , z	coordinate

CHAPTER 1: INTRODUCTION

1.1 Motivation

Producing clean and defect-free metals has been a major concern for metalcasters. Oxide inclusions are among the most commonly reported defects which can cause casting rejection. They affect the surface quality, machinability and mechanical performance of a cast part [1,2]. Inclusions form when the liquid metal comes into contact with oxygen during mold filling. In low alloy steel castings, the reaction between the deoxidized steel and oxygen is responsible for the formation of round reoxidation inclusion (Figure 1.1 (a)), while in light metals, including aluminum alloy castings, solid oxide films are generated (Figure 1.1 (b)). In ductile iron castings, dross inclusions (magnesium silicates) form when the magnesium and silicon in the melt react with oxygen (Figure 1.1 (c)). The removal of inclusions from castings, if possible, can be very costly. Numerous efforts have been made to minimize inclusions in castings, but methods to predict inclusion formation and generally valid gating design guidelines are currently not available.

Air entrainment during mold filling is known to be a major source of oxide inclusion formation in metal castings. Air entrainment is the exchange of air between the atmosphere and the flowing liquid. In free surface flows, air is entrained at surface discontinuities. Such surface discontinuities are created, for example, by a liquid jet plunging into a pool, breaking waves, or a hydraulic jump, in which a fast moving liquid discharges into a low velocity atmosphere. In the plunging jet case (Figure 1.2 [3]), the air is entrained in a thin layer around the perimeter of the jet where it enters the pool. The air entrainment rate depends primarily on the jet velocity, diameter and turbulence level. Air entrainment commences only above a certain critical jet velocity (approximately 1 m s^{-1} for turbulent water). For jet velocities at the point of impact of the order of 5 m s^{-1}, relative air entrainment rates of one cubic meter of air per cubic meter of liquid are easily reached.

During mold filling, several types of free surface flows can occur that entrain air. Liquid metal plunging into the sprue, jets emanating from ingates or falling over edges inside of the casting cavity, and returning waves in runners are some of the most important examples of such flows. Therefore, air entrainment during pouring depends on the gating system design. The gating system is all of the channels through which liquid metal passes to enter the casting cavity. Gating systems are composed of a pouring basin, sprue (down runner), sprue well, runner, and ingate where the gating system connects to the casting (Figure 1.3). The gating ratio of a filling system is the ratio of the sprue base area to the runner cross section area to the ingate cross section area: $A_{bs}: A_r : A_{in}$. Based on the cross section area of the sprue, runner and ingates, gating systems are categorized into non-pressurized and pressurized gating systems. For the non- pressurized filling systems, the minimum cross section area is located at the sprue base, while for the pressurized gating systems the local choke is at the ingate. Poor design of gating systems results in air entrainment during mold filling. Air entrainment at free surface discontinuity increases the exposure of melt to oxygen. Once air is entrained, the oxygen in that entrained air will almost immediately react with elements in the liquid metal to form solid, liquid, and/or gaseous oxides. Therefore, the oxide inclusion formation is governed by the oxygen content entrained into the liquid metal, and the prediction of oxide inclusion formation requires a model for predicting local air entrainment during pouring of metal castings. While the gaseous oxides can often escape from the casting cavity, liquid and solid oxides are transported with the liquid metal and ultimately end up as inclusions in the solidified casting. Inclusions can appear on the cope surface of the castings or they can stick to the mold or core walls before floating to the top surface.

1.2 Objectives of the Present Study

In the present work, experiments are conducted to study dross formation in ductile iron castings. In the experiments, castings with different filling systems, section thickness

and surface orientations are studied to investigate the dross formation and final distribution in castings. The different filling systems investigated in the experiments are common gating designs in ferrous and non-ferrous castings. Moreover, the effect of filters in the filling system is studied for two different casting geometries. Dross inclusions are measured by serial sectioning of the solidified castings.

Simulation software is now routinely used in the foundry industry to model not only solidification, but also the filling of the mold with the liquid metal. Such filling simulations are usually one-sided, meaning that they only calculate the flow of the metal but not of the air. Hence, air entrainment is not predicted. Even if the air were included in the calculations, air entrainment and the movement of air bubbles would be difficult to simulate directly because these phenomena occur on such a small scale that they cannot be resolved by a typical computational mesh used in a casting simulation (of the order of millimeters). For avoiding excessive computational time, approximate or sub-grid models have been developed, that attempt to calculate air entrainment as part of a one- or two-sided computational fluid dynamics simulation on a relatively coarse mesh, i.e., one that does not resolve the turbulent eddies and air bubbles directly. In the present study, the sub-grid model of Ma et al. [4] is implemented into a standard (one-sided) casting filling simulation code to calculate local air entrainment rates. An approximate method is proposed to estimate the turbulent kinetic energy without solving a separate turbulence model. The model is validated and calibrated by comparing predicted air entrainment rates for a plunging water jet with previously obtained experimental data. The model capabilities are demonstrated by simulating the flow in typical casting filling systems and calculating the air entrainment rates. It is shown how different pouring conditions and gating designs affect the air entrainment rate, hence, the formation of oxide inclusions.

Based on the volume of entrained air, a model is developed to predict the formation of oxide inclusions during mold filling. The generated oxide inclusions are then carried away with the melt flow to their final location.

1.3 Outline of the Text

First, in Chapter 2 the experimental studies and models developed for predicting the air entrainment and oxide inclusion generation are reviewed in detail. In Chapter 3, dross formation and the experiments conducted for studying dross inclusions in ductile iron casting are presented. Chapter 4 explains the developed model for predicting the local air entrainment and oxide inclusion formation and motion. The effects of different gating systems and pouring conditions on the air entrainment are simulated and shown in Chapter 5. Finally, the conclusions and future work are presented in Chapter 6.

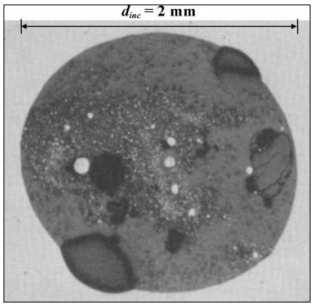

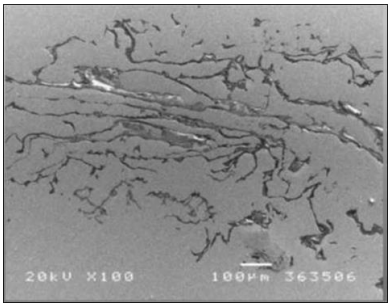

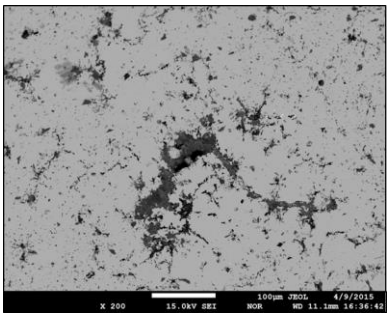

(a) (b) (c)

Figure 1.1 Oxide inclusions in metal castings: (a) reoxidation inclusion in steel castings, (b) double oxide film (bi-film) in aluminum casting, and (c) dross stringer in ductile iron casting.

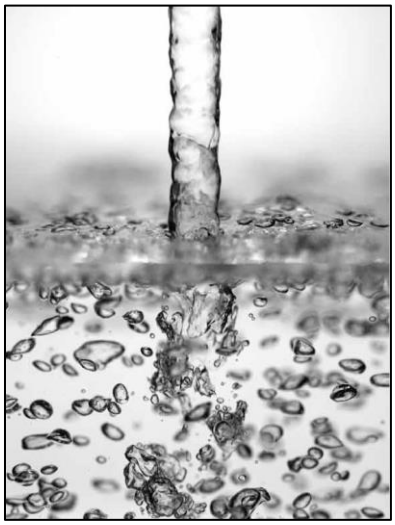

Figure 1.2 Air bubbles near a plunging liquid water jet by "Jesse Belden (NUWC) and Tadd T. Truscott (BYU)" [3].

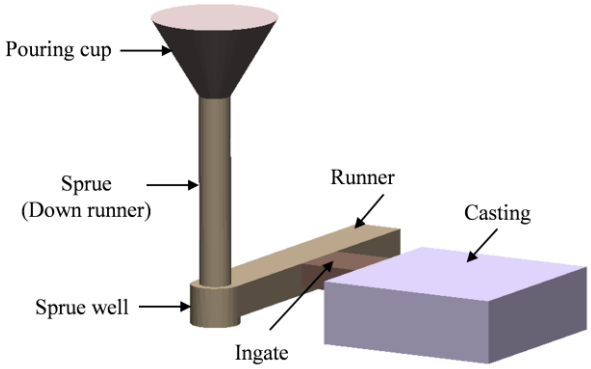

Figure 1.3 Components of a gating system.

CHAPTER 2: LITERATURE REVIEW

2.1 Introduction

In this chapter, first, the experiments for measuring the air entrainment in free surface flows are reviewed. Then, previous studies that have modeled the air entrainment in free surface flows are reviewed. While a number of models are developed for predicting the air entrainment in air-water structures, few attempts have been made to model the entrainment of air/oxides during pouring metal castings. Models developed for generating and tracking inclusions are reviewed at the end of this chapter.

2.2 Air Entrainment Measurements

Several experiments have been conducted to measure the air entrainment rate in free surface flows. The results of experimental studies have shown that for a plunging liquid jet (Figure 1.2), air entrainment does not occur below a certain liquid jet velocity. Once the inertial force of the impinging liquid jet overcomes the restraining forces, i.e. surface tension and buoyancy forces, air is entrained at the intersecting perimeter of the liquid jet and the quiescent pool. For laminar viscous jets, Lin and Donelly suggested a correlation for the entrainment onset in impinging circular liquid jets: $\mathrm{We}_e = 10\mathrm{Re}_e^{0.74}$ [5], where subscript *e* refers to entrainment onset. As reported in Ref. [6], Ciborowski and Bin proposed a simple statement for the turbulent liquid jets produced from short cylindrical nozzles: $\mathrm{We}_e = 400$. Ervine et al. [7] showed that the onset of the air entrainment for a plunging liquid jet depends on the turbulence level of the liquid jet. According to the measured entrainment onset values from numerous experiments, Chanson proposed a dimensionless correlation [8] which accounts for the dependency of entrainment onset on the turbulence intensity of the liquid jet: $u_e \mu_l / \sigma = 0.0109 \times [1 + 3.375 \times \exp(-70u'/u_e)]$.

Experimental measurements have shown that the volumetric air entrainment rate depends on the velocity and diameter, falling height, and the turbulence intensity of the liquid jet. The air entrainment mechanism depends on the liquid jet velocity at impact. While for low jet velocities, i.e. jet velocity at impact less than approximately 5 m s^{-1}, air is entrained along the surface disturbances of the free water jet, at high jet velocities an air cavity is formed along the periphery of the liquid jet at impact which is responsible for air entrainment [9,10]. Most of the air entrainment correlations are expressed in terms of the liquid jet velocity at impact location as $Q_a / Q_w \propto u_j^n$, where n shows the dependency of relative air entrainment to jet velocity at impact. Due to the different experimental conditions, several values of n are suggested for both low and high liquid jet velocities. However, the dependency power, n, is shown to be in the range of $1.25 \le n \le 2$ for low liquid jet velocities, and $0.5 \le n \le 1.5$ for higher liquid jet velocities [9,11,12,13]. Measurements have also pointed out that the relative air entrainment increases with the increase of the falling height and decreases with the increase of liquid jet diameter [6,9,12,13]. Moreover, the turbulence level of the liquid flow at the nozzle exit has a significant effect on the air entrainment rate [7]. The turbulence intensity along with the liquid jet velocity and diameter affects the disturbance size on the periphery of the liquid jet. Ervine et al. [7] correlated the relative air entrainment rate, Q_a / Q_w, to the size of these disturbances, δ / r: $Q_a / Q_w = 1.4 \times [(\delta / r)^2 + 2(\delta / r) - 0.1]^{0.6}$.

Water modeling experiments are useful in understanding the effect of various gating designs and pouring conditions on the air entrainment. Comparison between the results of water modeling experiments to those in liquid metal requires dynamic similarity. In steel, the kinematic viscosities of liquid steel and water are very similar. However, a full scale water model is necessary to accurately simulate molten steel flow behavior. A full scale water model will produce similar Reynolds and Froude numbers compared to molten steel. Water is commonly used to model steel flow by the wrought steel industry. However, few water modeling experiments have been conducted to correlate the pouring parameters and conditions to air entrainment during the pouring of

metal castings. The results of the water modeling studies conducted by Wanstall et al. [14] and Bates and Griffin [15] showed that a throttled bottom pour ladle entrains significantly more air compared to an open nozzle (unthrottled) configuration. In addition, results from this study indicate that shorter falling heights and filling times reduce the amount of entrained air. Through a series of experiments, Kuyucak [16] showed that using an offset pouring basin with a step before the sprue entrance allows the entrained air to escape to the atmosphere before entering the sprue. Additionally, the use of a nozzle extension submerged into the pouring basin significantly reduced the amount of entrained air during pouring. Afsharpour et al. [17] suggested that a conical pouring cup entrains large amount of bubbles, and using an offset step pouring basin and a small sprue reduces the air entrainment to a great extent.

2.3 Models for Predicting Air Entrainment

Sub-grid models have been developed to calculate the local air entrainment in free surface flows. In the model developed by Moraga et al. [18] air is entrained beneath a free surface once the normal velocity of liquid becomes larger than the rising velocity of bubbles. Though the model fails to quantitatively measure the air entrainment, it is advantageous in predicting the location of air entrainment in bubbly flows. A correlation is added to the model developed by Moraga to predict the bubbly flow in the vicinity of the plunging liquid jet [13]. The correlation for air entrainment rate is derived from the previous work of Sene et al. [9], where the air entrainment correlation depends on the liquid jet velocity at impact, u_j; the volumetric air entrainment rate is a function of u_j^3 and $u_j^{1.5}$, for low jet and high jet velocities, respectively. This model is only capable of predicting the location of air entrainment.

Models have been developed which correlate the air entrainment rate to the shear production rate of turbulent kinetic energy and turbulent kinetic energy dissipation rate at the air-water interface. The models developed by Shi et al. [19] and Ma et al. [20] define a threshold production rate and dissipation rate, respectively. In these models, air is

entrained once the production rate or dissipation rate at locations beneath the free surface exceeds a threshold value. The entrainment model is then combined with coalescence and breakup models to predict the void fraction for a surf-zone breaking wave. Results compare favorably with the experimental measurements, though discrepancies were observed in the predicted values as well as the location of entrained air.

Numerous studies have pointed out that at relatively low liquid jet velocities, air entrainment at surface discontinuities is associated with large values of the turbulent kinetic energy [19, 21]. Xiang et al. [21] developed a model to calculate the air entrainment rate as a function of the local turbulent kinetic energy and the jet velocity at the location of the surface discontinuity. A critical velocity is used in the model to determine the occurrence of air entrainment. Ma et al. [4] predict the rate of air entrainment as a function of the turbulent kinetic energy and the normal velocity gradient of the liquid at the liquid-air interface. Air is entrained only when the normal velocity at the interface increases in the direction normal to the interface. The model is used along with a turbulent two-phase computational fluid dynamics code to predict bubble void fractions in the bulk liquid. The model is validated by comparing the predicted void fraction profiles to the experimental measurements for hydraulic jumps [22], plunging jets [23] and surface ships [24]. For the hydraulic jump case, comparing the RANS and DES turbulence models indicate that while RANS model is unable to capture the air entrainment due to the wavy nature of the free surface at the upper roller region, the DES can capture the entrainment both at the toe region of the jump and at the upper roller region (Figure 2.1 (a)). For the plunging jet case (Figure 2.1 (b)), the model has been successfully implemented for one-way coupling, where the effect of the gas phase on the continuous liquid phase is neglected, and also for two-way coupling. Results show that the model is able to predict the location and rate of air entrainment. With a constant air entrainment coefficient for each free surface flow, e.g. hydraulic jump or plunging jet, the

model is able to capture the velocity dependence of the air entrainment rate on the liquid velocity. In this model, the entrainment constant depends on the free surface flow type.

Souder and Hirt [25,26] determine the air entrainment rate from the difference between the turbulent kinetic energy and the energy of surface stabilizing forces, i.e., surface tension and gravity. As in the study by Ma et al. [4], a separate turbulence model is solved to predict the mean flow characteristics, including the local turbulent kinetic energy. In this model, it is assumed that entrainment occurs over half of the free surface; hence, the model constant is set to 0.5. Comparison between predicted air entrainment rates and experimental data collected for plunging liquid jets, drop shafts, hydraulic jumps and spillways shows overall good agreement.

The most recent air entrainment model accounts for the interaction of vortices with the free surface [27]. Bubbles are entrained into the bulk liquid when the vortices within a certain distance are strong enough to drag the bubbles down into the bulk liquid. The entrainment onset and intensity is a function of the free surface stabilizing forces, i.e. surface tension and buoyancy forces, and the surface destabilizing forces, the inertial and gravity forces. The entrainment model, along with the breakup and coalescence models, is then implemented in the bubble number density equation for predicting the void fraction profiles. A single model constant is used for predicting the bubbly flow in two cases, 2D breaking wave and surface ships. Comparison between the predicted and measured void fraction profiles indicate that the developed model is capable of predicting the location and magnitude of the air entrainment in free surface flows.

While the above studies are aimed at predicting air entrainment in any kind of free surface flow, some models have been developed specifically for application in mold filling simulations for metal casting. A number of models have been developed which are capable of determining the extend of the free surface turbulence during liquid aluminum filling. In aluminum casting, an extremely thin solid oxide film covers the liquid metal surface, and surface turbulence has been found to be the main cause of the entrainment of

oxide films into the bulk liquid [1,28]. The oxide films are ceramic, mainly alumina (Al_2O_3). This makes these solid oxide films extremely stable (the melting point of alumina is 2000 °C). The dry side of these oxide films is exposed to the surrounding atmosphere and the wet side is in contact with the melt. As the liquid metal experiences surface turbulence, the dry side of the oxide becomes in contact with the dry side of the other oxide (Figure 2.2). Since the dry sides of the oxides are not bond together they form a discontinuity in the liquid metal bulk, which eventually acts as porosity or crack initiation site. Lai et al. [29,30] compare the modeled instantaneous free surface area of the melt to the instantaneous free surface area assuming the liquid metal fills the mold quiescently. The difference between these two free surface areas is used to determine the oxide entrainment magnitude. The results indicate that the instantaneous free surface area increases significantly above 0.4- 0.5 m s^{-1} ingate velocity, comparing favorably with Campbell's findings [28]. The model is then applied for different stages of filling, where results show that a majority of entrainment events occurs during filling the crucible and the pouring basin. Although this model appears to work for simple geometries, it is difficult to apply to complex filling systems. Furthermore, the model does not provide insight into the location of air entrainment. Though the balance between the inertial force and surface tension force acting on the liquid metal has suggested critical velocity for the onset of entrainment: $u_{cr} = 2(\rho\sigma / g)^{1/4}$ [1,28,29], several recent studies have pointed out the importance of non-dimensional numbers for predicting the free surface breakup in filling of mold cavity [30,31]. While the Weber number is found to be a proper criterion for vertical running systems, the Froude number has been suggested to be more appropriate for horizontal running systems. Such distinctions are difficult to apply to complex mold geometries. Determining the magnitude of air entrainment solely based on non-dimensional numbers also fails to account for the local turbulence intensity of the flow and the physical scale of the entraining phenomena [30].

Several criteria have been suggested for predicting entraining events in aluminum casting based on velocity vectors, free surface normals and liquid volume fractions in free surface computational cells [30,32,33]. These models are explained in detail in the next section.

2.4 Oxide Inclusion Generation and Tracking Models

A number of models have been developed to predict the generation and advection of oxide inclusions during filling of castings. Though tracking inclusions at each time step significantly increases the computational time, the models developed for this purpose are useful in predicting the final location of inclusions.

As mentioned earlier, the oxide entrainment in aluminum castings requires the dry side of oxides to be in contact with each other, which demands the velocities of these two overlaid flowing streams be opposite. This criterion is used in the 2-D Oxide Film Entrainment Tracking (OFET) model developed by Yang et al. [32] and Dai et al. [34] to judge the occurrence of entrainment and fold over of oxide films. Particles are generated at the free surface at a defined frequency, representing the solid oxide films. The local Weber number, i.e. ratio of the local inertial and surface tension forces, determines the expansion of the free surface. Upon the expansion of the free surface new particles are introduced. The model assumes that oxide films entrapped inside the bulk liquid are no longer exposed to the air; therefore, no new particles are introduced once these entrapped oxide films are expanded. This assumption fails to account for the case when the entrapped oxide films are exposed to the entrained air. Two filling systems with different runners are studied to validate the model (Figure 2.3). Results indicate that the ingate velocity affects the number and the distribution of oxide films generated during filling. Furthermore, the results show that the vortex runner has higher reliability compared to the traditional rectangular runner, which is in agreement with the bending strength results of experiments.

Sato et al. developed a model for predicting the entrapment of solid oxide films into the liquid aluminum during mold filling [35]. During mold filling, oxides covering the melt can collide with each other or the mold wall, break and be entrained into the bulk liquid. The model places marker particles at the free surface where the oxides collide and break (Figure 2.4). Each marker has two main parameters, the number of entrained oxides and the average free surface area of each oxide. In this model while the number of entrained oxides is a function of the alloy composition and collision velocity, the average free surface area is a function of the surface area of oxides involved in the collision and further the number of entrained oxides. According to this model, more smaller oxide films form at larger collision velocities. The collision of the free surface depends on the velocity vectors, distances between particles, dimensionless distances of the downward flow and upward flow and time step. The model can capture the entraining events of impinging flows, colliding fronts, returning waves and other free surface flows.

Following the model developed by Sato et al. [35], Reilly et al. classify the entraining events into three categories: flows with colliding fronts, shear fronts and impinging flows [33,36]. This model uses the velocity vectors, free surface normals and liquid volume fractions in free surface cells to define a series of Boolean logic criteria for predicting the occurrence of entraining events. The customized code used with Flow-3D utilizes free surface normals to identify the relative movement of the liquid free surface in each computational stencil. Once entrainment occurs, a particle with constant diameter, density and coefficient of restitution is generated at the location of entrainment to represent the entrained oxide. The particles are then tracked to their final location. To avoid generating large number of particles, the occurrence of entraining events for each computational stencil was evaluated based on a user-defined generation frequency. The model is validated with experiments of gating systems with and without filter. The results indicate that the sample taken from the filtered gating had fewer particles compared to the sample from the unfiltered gating system. This is in good agreement with the bending

strength test results of the experimental specimens. The results of the simulations also show the majority of entrainment events occur due to the impinging liquid metal on the bottom of the pouring basin and further down at the bottom of the sprue. While the model is able to predict the entrainment of oxides, it is unable to estimate the transport of the entrained oxides. The model is further applied three different gating systems: direct pour, vertical bottom gate and horizontal side gate, to study the entrainment of oxide using this model. The results show that for a constant head height, the filling system with the plunging jet (direct pour) entrained more air compared to the two other filling systems. Therefore, castings produced by the plunging jet flow type (direct pour) are less reliable compared to castings produced by the rising jet flows (vertical bottom gate) and returning wave (horizontal side gate). The bending strength results from experiments showed a similar trend (Figure 2.5). By providing a single quantity, i.e. the total number of particles, the model is able to compare different gating systems. However, treating free surface turbulence events differently increases the computational time of a single simulation.

The model developed by Melendez et al. [2] predicts the entire life cycle of reoxidation inclusions in steel castings, including the generation and final location of the inclusions. In this model, inclusions are released either at the inlet to the mold or generated at the free surface as spheres with constant density and diameters. In addition to the inclusions released at the inlet, which represent those inclusions entering the mold from the ladle, inclusions are further generated at the free surface during filling the mold cavity. These inclusions are generated at the free surface based on the user defined spacing length. Comparison between the user defined spacing length and the average spacing between existing inclusions at the beginning of each time step determines whether inclusions must be generated or not. Since the generated inclusions have an extremely small diameter, the total volume of the generated inclusions is negligibly small. In this model, the number of generated inclusions on the free surface depends on

the user defined spacing length, free surface evolution and the tendency of inclusions to be swept away from the interface. The growth of inclusions is controlled by the oxygen transfer through the melt/air interface and also the agglomeration of inclusions. The inclusions are tracked by solving the equation of motion for each inclusion at each time step. For the inclusions in the vicinity of walls, a slip coefficient is adjusted by comparing the simulation results to the measured results in steel production parts. Comparison between the simulation results and measurements made from steel production parts indicate that the model is able to predict the approximate final location of inclusions (Figure 2.6). Parametric studies are performed to study the effect of grid size, agglomeration length and slip coefficient on the final location of inclusions. This model does not account for the local free surface turbulence.

While these models provide insight into the location of entrainment, they fail to quantify the amount of entrained air or oxide inclusions.

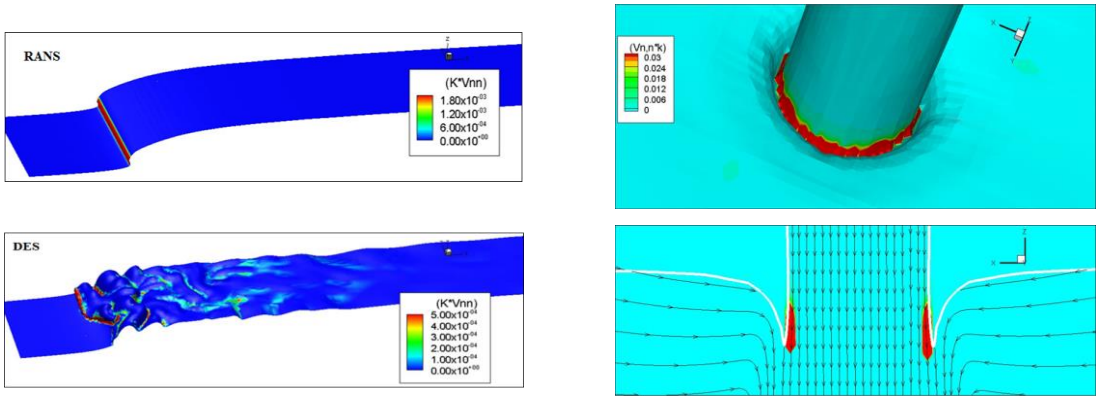

(a) (b)

Figure 2.1 Precited local air entrainment in the model developed by Ma et al. for (a) Hydraulic jump [22], and (b) Plunging jet [23].

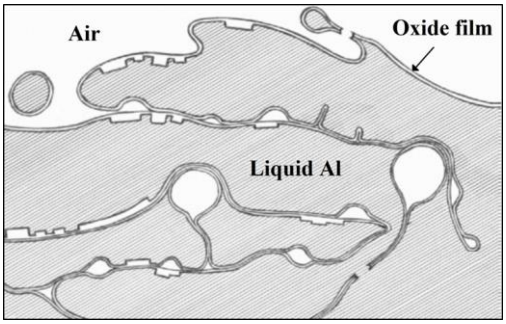

Figure 2.2 Entrainment of oxide films and air bubbles in liquid aluminum casting. Adapted from [28].

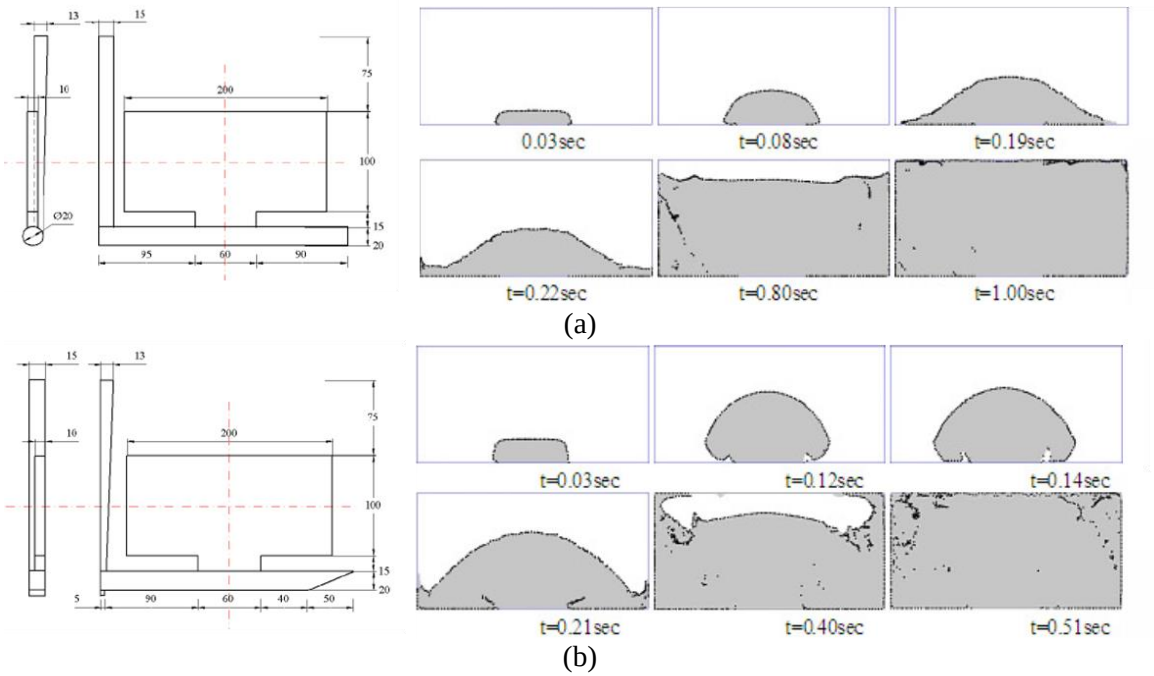

Figure 2.3 Predicted oxide film defect distribution in castings with different runner systems by using the OFET numerical algorithm: (a) vortex-flow runner, and (b) rectangular runner. All dimensions are in mm. [34]

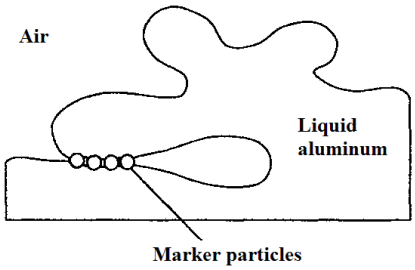

Figure 2.4 Generation of marker particles on the collision of free surface with fluid or mold. Adapted from Sako et al. [35].

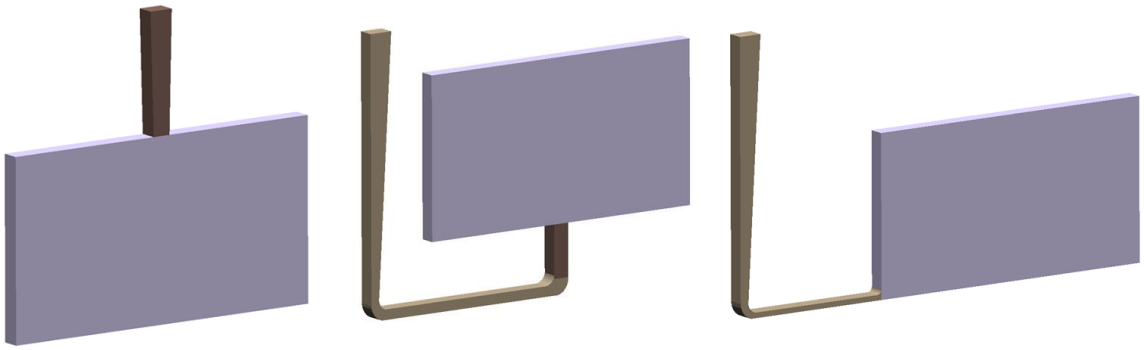

(a) (b) (c)

Figure 2.5 Three different flow configurations: (a) plunging jet type flow, (b) returning wave, and (c) rising jet. Adapted from Yue [36].

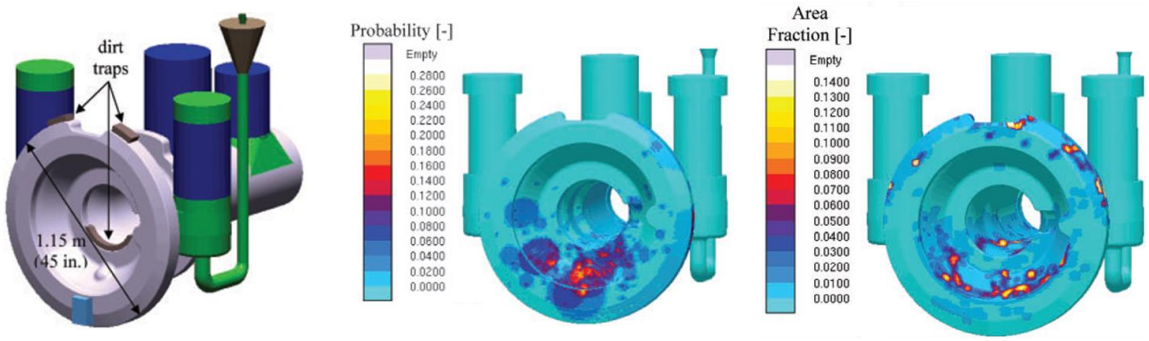

(a) (b) (c)

Figure 2.6 Measured and predicted inclusion distribution from the model developed by melendez et al. [2] in a spindle casting: (a) schematic of the spindle casting, (b) measured inclusion probability plot, and (c) predicted inclusion area fraction. [2]

CHAPTER 3: DROSS FORMATION IN DUCTILE IRON CASTINGS

3.1 Introduction

Ductile iron has a wide range of applications from automobile parts to wind turbine components. Sand inclusions and dross inclusions are the most frequently reported oxide inclusions in ductile iron castings. While sand inclusions are solely composed of silica, SiO_2, dross inclusions mainly consist of magnesium silicates. Dross inclusions can form during different stages of ductile iron casting, including metal treatment (nodularization) and post inoculation, transferring and holding stage, and also during pouring as a result of air entrainment. Dross inclusions which are allowed to enter the mold cavity, can be entrained into the bulk liquid, and appear at the casting surface. In addition, depending on the moisture content of the sand, oxidation through the water vapor inside the mold can also contribute to inclusion formation during pouring. The chemical composition of oxide inclusions will change as a result of the Mg addition and temperature drop. The important parameters affecting dross formation are the oxygen content entrained into the melt, pouring temperature, and the magnesium and silicon contents [37]. Air entrainment during filling provides the oxygen required for dross formation.

Dross inclusions can appear in ductile iron castings as large and gross inclusions or as filamentary shaped inclusions [38,39,40] (Figure 3.1). The shape of dross inclusions depends on the pouring temperature: Higher pouring temperatures favor stringer and filamentary dross while at lower pouring temperatures large solid dross inclusions are formed. Since liquid ductile iron is usually poured at relatively high temperatures (1340-1420 °C), the dross inclusions reported in iron foundries mostly have a filamentary shape. Experiments are conducted to study the effect of different parameters on the formation and final location of inclusions in ductile iron castings. Before presenting the ductile iron experiments, the mechanism of dross formation in ductile iron is reviewed in detail.

3.2 Dross Formation

Pouring temperature, element contents inside the melt and the oxidizing agents are important factors affecting the inclusion formation and composition. Though magnesium silicates (mostly forsterite- Mg_2SiO_4), magnesium oxide and silicon oxide are the main constituents of dross, traces of aluminum oxide, iron oxide, manganese oxide and sulfides can also be found in the composition of dross inclusions. Magnesium oxide mostly forms during magnesium treatment, and later during pouring, while other oxides, including silica, forms during cooling of the melt inside the ladle or during filling [38]. The subsequent reaction between magnesium oxide and silicon oxide results in dross formation [41].

The Ellingham diagram (Figure 3.2 [42]) indicates the standard free energies of formation of oxides from the elements as a function of temperature, and is an approximate method for predicting the reduction reaction temperature of the oxides. This method, which is purely based on the Gibbs free energy of reactions, ignores the kinetics of the reaction. Based on the Ellingham diagram, the intersection of the carbon monoxide formation line with oxides determines the temperature at which reduction occurs: below this temperature the metal oxides are stable while above this temperature carbon monoxide gas is the stable component. According to the Ellingham diagram, the reduction of melt constituents is in the following order: calcium, aluminum, magnesium, silicon, manganese and iron, starting with calcium at higher temperatures and ending with iron at below the liquidus temperature.

Ductile iron casting requires an additional step compared to grey iron. In grey iron, the graphite has flake shape, while the morphology of graphite in ductile iron is spheroidal (nodular). For changing the graphite shape from flake to spheroidal nodularizer- usually MgFeSi alloy- is added to the base iron prior to pouring. Since magnesium oxidizes spontaneously at high temperatures, i.e. $1450 < T(^{\circ}C) <$ 1550-

temperature at which melt is treated, once magnesium reacts with the base iron melt, most of the magnesium reacts with the oxygen to form magnesia (MgO) and some of the magnesium remains dissolved inside the melt [41].

The reaction between the carbon in the melt with the oxygen in the surrounding air forms carbon monoxide (CO) gas. In addition, large volume of air is entrained during tapping liquid iron into the ladle. Based on the Ellingham diagram at high temperatures, $T > 1500$ °C, the majority of oxygen content in the melt is in the form of carbon monoxide gas and CO gas is the stable compound which covers the melt, avoiding oxide inclusion formation. As the temperature decreases during the holding, transferring and pouring, patches of silica film starts forming according to the following reaction [38]

$$2CO(g) + [Si] \rightarrow 2[C] + SiO_2(s) \quad (3.1)$$

where the square brackets refer to the dissolved element, and the (g) and (s) refer to the gas and solid states of the oxide. The temperature at which silicon reduction reaction occurs is a function of the chemical composition of the melt (Figure 3.3 [43]). As mentioned earlier the Ellingham diagram does not take into account the content of each element in determining the reduction reaction temperatures. The diagram in Figure 3.3, shows the effect of carbon and silicon contents on the silica reduction reaction temperature. According to this diagram, reducing the carbon content and increasing the silicon content increases the reduction reaction temperature.

The subsequent reaction between MgO and SiO_2 forms magnesium silicate film, which from a thermodynamics viewpoint, i.e. according to Gibbs free energy, is more stable than the silica film. As silica starts to form it reacts with the MgO and reaction (3.2) will occur:

$$MgO(s) + SiO_2(s) \rightarrow MgSiO_3(s) \quad (3.2)$$

The enstatite ($MgO.SiO_2$) formed in this stage is not stable and due to the high diffusivity of Mg^{2+} compared to Si^{4+}, MgO continues to react with the enstatite to form forsterite ($2MgO.SiO_2$):

$$MgO(s) + MgSiO_3(s) \rightarrow Mg_2SiO_4(s) \quad (3.3)$$

Theoretically, in the case of excess silica, forsterite can react with silica and form enstatite, however, this is not thermodynamically favorable.

At high temperatures, dross inclusions mostly consist of patches of forsterite film (Figure 3.4 [44]); however, as the temperature decreases to lower temperatures, the high carbon content in the form of carbon monoxide starts reacting with the dissolved manganese and forms manganese oxide:

$$CO(g) + [Mn] \rightarrow [C] + MnO(l) \quad (3.4)$$

Further temperature drop to liquidus temperature (T_{liq}), about 1220 °C, the CO gas reacts with iron (FeO) and forms iron oxide:

$$CO(g) + [Fe] \rightarrow [C] + FeO(l) \quad (3.5)$$

Hence, at lower temperatures both manganese and iron oxidize spontaneously, increasing the MnO and FeO contents of the oxide inclusions; this reduces the melting temperature of the inclusions. The amount of MnO and FeO formed during temperature drop depends on the Mn and Fe contents of the melt and also the available oxygen. The manganese content is usually low (mostly remained from raw material); therefore, only traces of MnO are observed in the composition of dross inclusions in ductile iron castings. On the other hand, due to the large content of iron (iron content exceeds 93% of ductile iron composition) and also, since iron oxidizes more readily as the temperature decreases, the iron oxide increases during the temperature drop. The iron oxide will then mix with magnesium silicates (forsterite), resulting in iron oxide-rich dross inclusions. While at high temperatures inclusions are fluid films, at lower temperatures (below 1350 °C), crusty and solid dross is bonded by a more fluid phase [43].

Inoculation/ post-inoculation is another step in ductile iron casting for increasing the nucleation sites of the graphite during solidification. The reaction between the ferrosilicon treatment alloy with the oxygen content produces iron oxide and silica. MgO, SiO_2 and FeO formed during the nodularization and holding stage will float to the surface of the melt to form ladle dross. Some of the oxygen in the melt comes from the rust of the raw material and also surface oxidation of iron during melting the raw material.

Dross inclusions in final cast parts are usually observed along with carbon monoxide gas defects. These gas holes can be either in the form of small pinholes or large subsurface blowholes which can be round or have irregular shapes usually having smooth inside surface. Hydrogen solubility in liquid iron is lower than in steel, therefore hydrogen gas holes are not important sources of gas defects in iron castings [43]. By the time which solidification starts, any gas formed at high temperatures during filling has escaped through the vents and/or the sand mold. At temperatures close to the liquidus, $1220 < T_{liq}(°C) < 1280$, MgO, SiO_2 (and forsterite) and MnO are stable compounds, and according to the Ellingham diagram, only iron oxide can be reduced by carbon at these low temperatures. Two necessary conditions are required for the formation of the CO gas holes [43,45]:

1. Reaction between iron oxide and the carbon (graphite) available inside the melt (Reaction (3.5) reversed towards left).
2. At the time of reaction, the dross must be fluid so it can completely wet the graphite, a condition necessary for increasing the reactivity of the inclusions. At these low temperatures, the dross becomes a mixture of solid magnesium silicate bonded by a fluid phase high in MnO and FeO phases.

Based on the abovementioned reaction, first the graphite precipitates in the melt at liquidus temperature. Then, the inclusion rich in iron oxide reacts with the graphite resulting in CO gas.

Dross inclusions can also be associated with exploded graphite. The magnesium responsible for spherodizing the graphite reacts with the oxygen entrained into the melt; hence no magnesium is available to ensure nodular graphite [37].

Experiments have been conducted to study the effect of gating system on the formation of dross inclusions during pouring of ductile iron castings. Using an offset pouring basin, tapered sprue and avoiding local chokes in the gating system are recommended for reducing dross inclusions during pouring [38,41,46]. Heine and Loper [38] experiments revealed that though pouring iron with less turbulence is necessary for the production of clean ductile iron castings, pouring at low temperatures masks the effect of gating system. Latona et al. [40] showed that dross formation during filling is mostly affected by the liquid iron velocity inside the runner. In this study, the castings were cut in mid-pane for dross evaluation. The results conclude that a gating system with a ratio of 4:8:3, where the melt velocity at the runner is the least in the entire gating, is beneficial in reducing dross inclusions. While the castings used in this study include a riser connected to the casting, the authors do not indicate how much of dross has swept into the riser.

3.3 Experimental Setup

Experiments were conducted to study the effect of gating system on the formation of dross inclusions. In addition, castings with complex geometries were poured to study the effect of inclined surfaces and sudden area changes on the final distribution of dross inclusions. Moreover, the effect of placing filter in the gating system was also studied. Table 3.1 summarizes the main purpose of each trial.

3.3.1 Casting Procedure

Experimental casting trials were performed at the University of Northern Iowa's Metal Casting Center. For the majority of experiments the molds were printed with a 3D

printing machine. Only for one set of experiments (Heat #2) the cope and drag were hand packed and manually rammed. To build the molds (i.e., cope and drag), first, the sulphonic acid, 0.3% of the mold weight, was added to Unimin® IC55 silica lake sand. Then the mixture was bonded with a furfuryl alcohol binder system (1.25% of mold weight). In the first trial (Heat #1), large gases were trapped in the casting; therefore, in trials 2, 3 and 4 molds were vented for avoiding these gases.

For all of experiments the target chemistry was En-GJS-400-18-LT (EN-JS1025, in US system 60-40-18) grade of ductile iron. Raw materials were melted in a 300 lb heat induction furnace. Due to the heat loss encountered during melt treatment, holding and transferring from the furnace to pouring ladle, before tapping the iron the melt was heated to approximately 1520 °C. The temperature inside the furnace and ladle was measured with B-type thermocouples. Immediately before tapping the melt to the magnesium treatment box, all the impurities and slag were skimmed from the melt surface in the furnace.

The iron was tapped into a treatment box, where it reacted with the nodularizer (MgFeSi alloy) and inoculants (FeSi alloy). After reacting with the magnesium, liquid ductile iron was led to the ladle from bottom of the treatment box. In Heats #3 and #4, some of the nodularizer and inoculant were placed at the bottom of the ladle and covered, therefore, part of the nodularization and inoculation took place inside the ladle. After the magnesium treatment and inoculation during the holding and transferring stages, large chunks of dross was formed prior to pouring as a result of melt elements reaction with the surrounding oxygen available in the air (Figure 3.5). Table 3.1 indicates whether for each heat the ladle dross was removed prior to pouring or not. For all of the trials the total time of nodularization, transferring and holding was approximately 2 minutes. Before pouring the test castings, a coin size specimen was taken from the melt to analyze the chemical composition of the ductile iron (Table 3.2). During pouring, the pour time for each experiment was recorded by a stopwatch. The pouring of the molds was arranged in a

way that the pouring temperature would not affect the final conclusion. Table 3.3 shows the pouring temperature and total temperature drop for each set of experiments. At the end of each set of experiment, a sample was extracted from the casting to study the microstructure of the iron. The graphite nodules shown in Figure 3.6 indicate that the poured iron was ductile iron.

The castings were remained in the mold overnight and allowed to cool down to the room temperature. After cooling to the room temperature the castings were cleaned and evaluated at the cope surface, and at the mid-plane for dross inclusions. Some of the castings were further examined by sectioning the top surface of the castings in 1 mm steps down to a depth of 8 mm.

3.3.2 Effect of gating system design

As mentioned earlier, the gating system design affects the liquid metal flow inside the mold, hence the air entrainment during pouring. For studying the effect of free surface turbulence on dross formation, castings with different filling systems were poured. The geometries of different gating systems are shown in Figure 3.7. Gating systems studied in the experiments are common filling systems used in ferrous and non-ferrous castings. For the first three gating systems the casting has a length and width of 152.4 mm (6”) and a height of 50.8 mm (2”) height. Gating A is a non-pressurized gating where the flow entering the casting experiences water fall effect, resulting in plunge point air entrainment. In gating B, the liquid iron entering the casting experiences surface turbulence at the ingate. For the third gating, gating C, liquid iron fills the casting from the bottom of the block via a vertical fan ingate. Similar to gating A, gating D is a non-pressurized gating, and the casting length and width are 203.2 mm and the height is 76.2 mm. This gating is a simple bad gating system in which the liquid iron impinges on the sprue well and further on the bottom of the casting. Gating E is similar to gating C, but with a larger casting and opened up gating. The main purpose of this gating was to study

a gating system with quiescent filling. Table 3.4 shows the average pouring time and gating ratio for each gating system. For each of the gatings A, B and C, two castings were poured and for gatings D and E, one casting was poured.

In gating A, the liquid iron impinging on the sprue base further experiences water fall effect as the liquid metal enters the casting cavity. This results in plunge point air entrainment. As the filling proceeds, the height which liquid impinges on the pool inside the casting reduces, reducing the air entrainment rate. Due to the reduced ingate cross-sectional area in gating B, the liquid iron jet emanates from the ingate once it enters the casting, therefore, the liquid metal area exposed to the air increases, increasing the air entrainment. As the casting is filled, the effect of surface turbulence vanishes and air entrainment reduces. For bottom-gated castings where the gates are horizontal (gating B), the returning wave from the end of the casting entrains air; while for the castings with vertical bottom gates (gating C), the fountain flow at the gate is responsible for the air entrainment. Figure 3.8 shows the top surface of the casting after 2.5 mm milling. The milling results do not show significant difference between three different gating configurations. This can be due to the dimensions of the designed castings which have resulted in pouring times less than 10 seconds (Table 3.4). This time is believed not to be sufficient for the formation of dross inclusions, hence, distinguishing between different gating systems. For this trail, the ladle dross was removed prior to pouring.

In gating D large amounts of inclusions is observed at the cope surface and at the vicinity of the cope surface (Figure 3.9), pointing out that the impinging liquid iron at the sprue well and further at the bottom of the casting, increases the air entrainment, resulting in more inclusions. In addition, since the ladle dross was not removed prior to pouring, large chunks of dross inclusions are observed in the milling results. Compared to gating D, the mid-plane of gating E (Figure 3.10) shows few subsurface dross inclusions indicating that gating D is a good gating where the free surface turbulence is minimized during pouring.

3.3.3 Complex geometries and Effect of filter

The main purpose of this set of experiment was to study the effect of casting geometry on the final location of inclusions and also the effect of filter on blocking oxide inclusions. In all of the following experiments, the ladle slag and dross was not removed prior to pouring. Two different complex castings were studied for this purpose, casting with inclined surface (Figure 3.11) and casting with thin section connected to heavy section (Figure 3.12). In addition, for each of these geometries a casting was poured with filter placed in the gating system.

Figure 3.11 shows the geometry of the gating system for the castings with inclined surface. Two castings were poured for casting A (castings A1 and A2), and one for each of the castings B and C. The milling results (Figure 3.13) for the casting with inclined surface indicate that majority of oxide inclusions stick to the larger horizontal part before entering the inclined surface. Only few inclusions are observed on the inclined portion, and barely any inclusions can be found at the vicinity of the ingate. The inclusions still exist at lower sections of the horizontal portion of the casting. Therefore, it can be concluded that for castings with inclined surface, the inclusions are cleaned from the melt before the returning wave reaches the inclined portion of the casting. The top surface of the larger horizontal part acts as the cope surface and inclusions stick to the top of the larger horizontal part before entering the inclined surface. The results show the occurrence of oxide inclusions is not restricted to the cope surface of the castings, which is in agreement with previous findings [2].

As it can be seen in the mid-plane view (Figure 3.14) and also in the milling results, dross inclusions are accompanied by carbon monoxide gas holes; these gas holes form early during the solidification and get trapped beneath the solidified surface not being able to escape through vents or sand mold. As mentioned earlier, during early solidification, the inclusions rich in iron oxide react with the precipitated carbon in the

melt to from carbon monoxide gas. High contents of carbon along with lower pouring temperature are the main reason for large amount of gas holes in the casting. The effect of pouring temperature can be seen by comparing castings A1 (Figure 3.14 (a)), poured at high temperature, and casting A2 (Figure 3.14 (b)), poured at lower temperature. Dross inclusions are usually accompanied with carbon monoxide gas holes. As mentioned in section 3.2, lowering the temperature increases the FeO content of inclusions, increasing the reaction with the graphite inside the melt and eventually producing larger carbon monoxide gas holes. The castings shown in Figure 3.14 are from Heat #3, and according to Table 3.2, the carbon content in Heat #3 is larger than the other trials. Increase in carbon content reduces the surface tension making the gas bubble nucleation easier [43], increasing the CO gas holes. The thin solidified layer above the gas holes proves that CO gas is formed early during the solidification stage.

Comparison between the cases without filter and with filter (Figure 3.15) shows that the filter blocks a large portion of the inclusions from entering the casting. However inclusions still exist inside the casting for gating systems with filter (Figure 3.15 (b)). This is due to the air entrainment occurring beyond the filter. Air is entrained once the liquid metal impinges on the large horizontal part at the bottom of the inclined surface. In addition, the returning wave at the end of the horizontal part contributes to air entrainment. Due to the lower carbon content and relatively higher pouring temperatures, small amount of carbon monoxide gas are formed compared to the previous trials.

The geometry of the casting with thin section is shown in Figure 3.12. Two castings were poured for the configuration without filter (Casting A) and one casting for the gating with filter (Casting B). Significant amount of dross inclusions is observed at the vicinity of the thin section (Figure 3.16 (a)). Dross formed in the ladle and further during filling enters the mold cavity. Due to the sudden change in the area at the joint location of the block and the fin, majority of inclusions are not able to enter the fin, therefore these inclusions stick to top surface of the block adjacent to the fin. Those

inclusions which are able to enter the fin, cannot flow all over the way to the top of the fin and stick to the walls of the fin close to the bottom of the fin. Inclusions which are not able to enter the fin, are swept away from the fin towards the ingate and riser neck. Figure 3.16 (b) indicates that, similar to the casting with inclined surface, filters block the already formed dross inclusions during the metal treatment and in the gating prior to entering the casting. Barely any inclusion can be found in casting with filter.

3.4 Calculation of Dross Properties

Samples were extracted from the castings to study the dross inclusion shape, size and composition under the scanning electron microscope (SEM). The SEM device was equipped with Energy- Dispersive X-ray spectroscopy (EDS) to analyze the oxide inclusion composition. The SEM-EDS analysis was conducted at Central Microscopy Research Facility center at university of Iowa. Elemental mapping of the inclusion area further proves the existence of magnesium silicates (combination of oxygen, magnesium and silicon) in dross composition (Figure 3.17).

Conversion of the air entrainment volume to inclusion volume requires the molecular weight and density of inclusions to be known. The density and molecular weight of inclusions can be calculated from the chemical composition of the inclusions. The chemical composition of dross inclusions is calculated based on the EDS/WDS analysis (Table 3.5). The density of the oxide inclusions is calculated based on the density of the individual oxides at $T = 1400\ ^{\circ}C$ [47,48,49]. No data were available for the density of iron oxide, calcium oxide and manganese oxide at $T = 1400\ ^{\circ}C$, therefore, the density of the oxides at $T = 25\ ^{\circ}C$ is used. Based on the average weight percentage of these oxides (in total, FeO, CaO and MnO account for approximately 25% of the inclusion composition), this assumption will not significantly affect the average density of the inclusions.

$$\rho_{inc} = \frac{1}{\sum_{k=1}^{n}(\frac{x_k}{\rho_k})} \Rightarrow \rho_{inc} = 3140 \text{kgm}^{-3} \tag{3.6}$$

where ρ_{inc}, ρ_k, x_k and n are the inclusion density, oxide density, the weight percentage of each oxide, and the number of oxides, respectively. The molecular weight of dross inclusion is calculated as

$$M_{inc} = \sum_{k=1}^{n}(y_k.M_k) \Rightarrow M_{inc} = 109.5 \text{gmol}^{-1} \tag{3.7}$$

where M_{inc}, M_k, and y_k are the molecular weight of the inclusion and individual oxide, the molar fraction of each oxide, respectively. In the calculations the carbon monoxide gas content is not taken into account.

The conversion constant is the ratio of the inclusion volume to entrained air volume:

$$V_{\text{inc}} = C_{cnv} V_a \tag{3.8}$$

$$\frac{V_{inc}}{V_a} = \frac{\frac{m_{inc}}{\rho_{inc}}}{\frac{V_{O_2}}{0.2095}} = \frac{\frac{n_{inc} M_{inc}}{\rho_{inc}}}{\frac{n_{O_2} \overline{R} T}{0.2095 \times P}} \tag{3.9}$$

Equation (3.9) indicates that the conversion constant is a function of the temperature and pressure of entrained air, and also the number of inclusion mole per mole of oxygen. By assuming air at atmospheric pressure and pouring temperature of T= 1400 °C, the conversion constant is calculated as

$$C_{cnv} = \frac{V_{inc}}{V_a} = 5.3 \times 10^{-5} \frac{n_{inc}}{n_{O_2}} \tag{3.10}$$

The ratio of inclusion mole to oxygen moles depends on whether the carbon monoxide gas is considered in the inclusion composition or not. Assuming inclusion composition without CO gas: $C_{cnv} = 4.3 \times 10^{-5}$.

3.5 Summary

Ductile iron experiments are conducted for studying the effects of filling system on dross formation. The gating system design affects the liquid metal flow inside the gating system, hence the inclusion formation. Reducing oxide inclusions during filling requires a smooth flow where the liquid metal experiences less free surface turbulence. Results show that bottom gated pressurized filling systems are beneficial in reducing the air entrainment, hence inclusion formation during mold filling. Local chokes in traditional gating systems, result in local surface turbulence, which increases the volume of entrained air and inclusion formation. In addition, castings with different section thicknesses and surface orientations were studied. Results show the geometry of the casting affects the final location of the inclusions; in castings with inclined surface, the inclusions stick to mold walls before the melt reaches the inclined section of the casting. For castings with sudden area reduction, such as castings with fin, the majority of inclusions are observed at the vicinity of the region with sudden area change. Filters block the inclusions from entering the mold cavity, and are considered as the least costly method for avoiding/controlling inclusions. Though filters capture inclusions formed prior to the ingates in castings, the liquid metal experiencing surface turbulence beyond the filter leads to the formation of new oxide inclusions. In addition, some already existing inclusions, which can pass the filter, increase in size as the flow experiences surface turbulence.

Table 3.1 Ductile iron trials poured for studying dross formation.

	Purpose
Heat #1	Effect of gating system
Heat #2	Effect of gating system
Heat #3	Complex geometry/ Effect of gating system
Heat #4	Complex geometry/ Effect of filter

Table 3.2 Chemical composition wt.%, (balance Fe) for each set of experiment.

	C	**Si**	**Mn**	**P**	**S**	**Ni**	**Mg**
Target Heat	3.6	2.65	0.15	0.016	0.02	0.029	0.036
Heat #1	3.52	2.41	0.32	0.022	0.008	0.059	0.035
Heat #2	3.4	2.38	0.057	0.035	0.011	0.026	0.055
Heat #3	4.03	1.84	0.143	0.002	0.002	0.019	0.055
Heat #4	3.64	2.09	0.132	0.016	0.007	0.017	0.06

Table 3.3 Pouring temperature and temperature drop for each trial.

	Pouring temperature (°C)	**Total temperature drop (°C)**
Heat #1	1401	55.4
Heat #2	1382	-
Heat #3	1402	112
Heat #4	1374	92

Table 3.4 Filling time for each gating system.

	Heat #	Average Pouring time (s)
Gating A	1	8.7
Gating B	1	8.4
Gating C	1	10.1
Gating D	2	17
Gating E	3	14

Table 3.5 Properties of individual oxides available in dross composition.

Oxide	Molecular weight M_k (g mol^{-1})	Density ρ_k (kg m^{-3})	Mass Fraction (x_k)	Mole Fraction (y_k)
Mg_2SiO_4	100.4	3040	0.739	0.575
SiO_2	60.1	2210	0.073	0.132
FeO	140.7	5740	0.093	0.10
Al_2O_3	71.8	3850	0.037	0.142
CaO	102	3350	0.052	0.04
MnO	56.1	5370	0.008	0.011

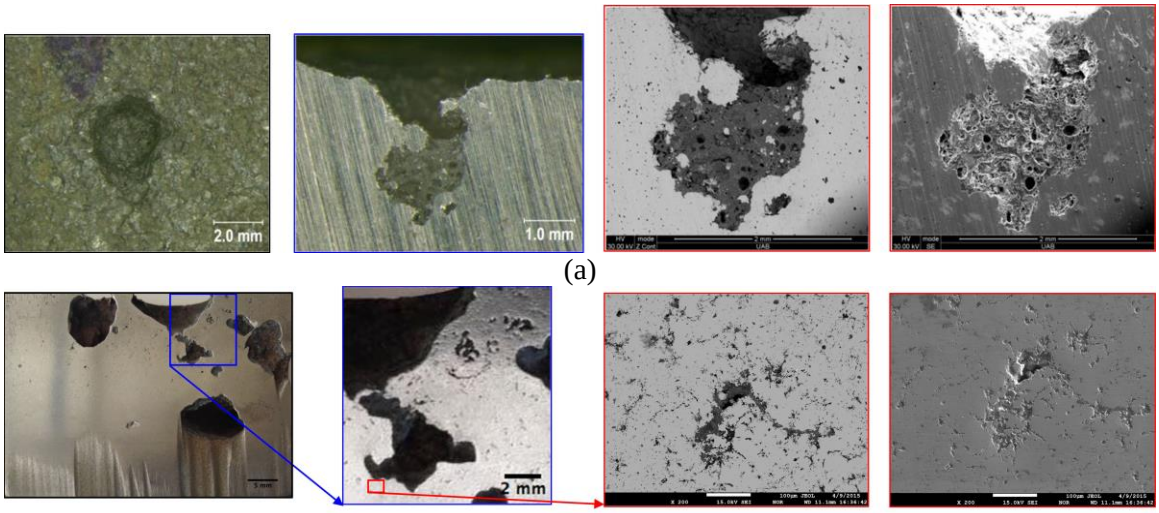

Figure 3.1 Dross inclusions in different shapes: (a) round, and (b) filamentary shape.

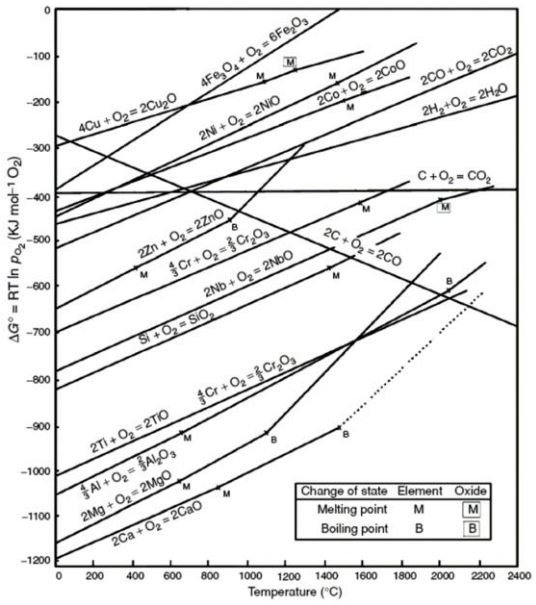

Figure 3.2 Ellingham Diagram showing the oxidation of elements.

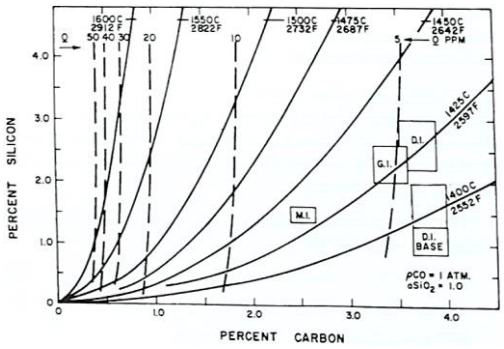

Figure 3.3 Silica reduction temperature as a function of the carbon and silicon contents [43].

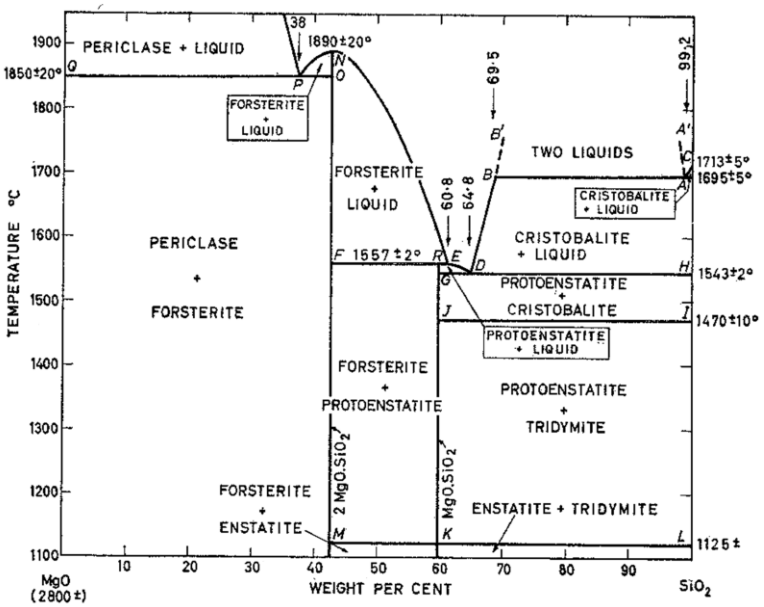

Figure 3.4 Phase diagram of magnesium oxide and silicon oxide [44].

Figure 3.5 Ladle dross formed after magnesium treatment and inoculation.

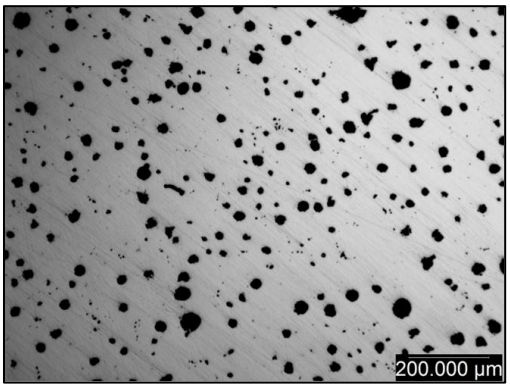

Figure 3.6 Optical micrograph of a specimen showing the graphite nodules in the microstructure of the ductile iron.

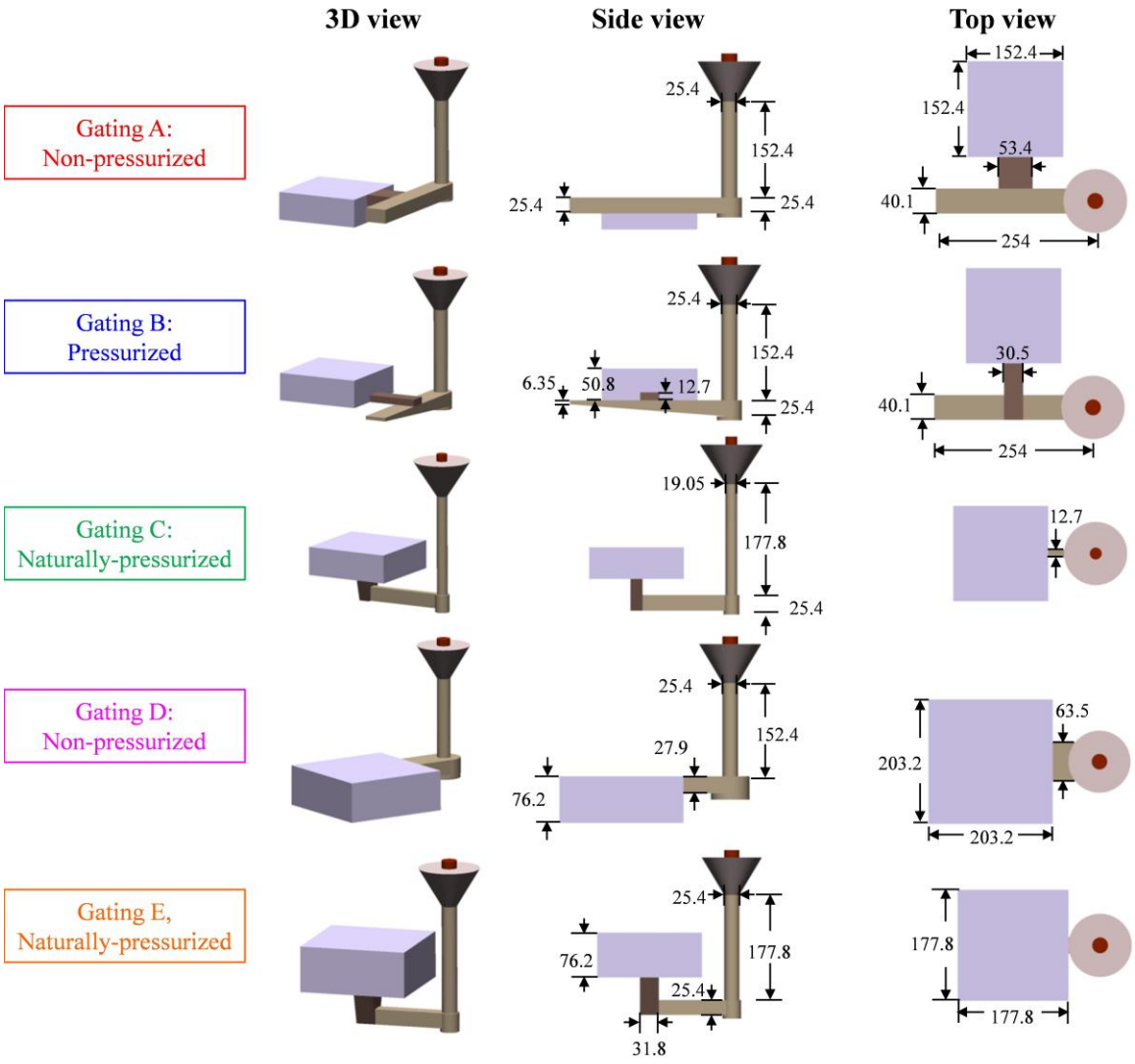

Figure 3.7 Design of different gating systems. All dimensions in mm.

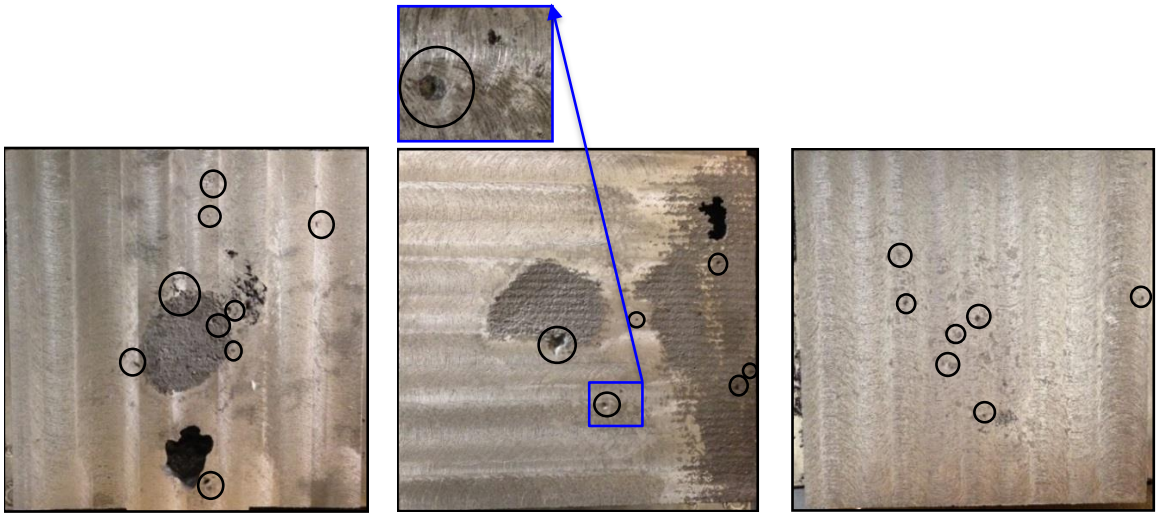

(a) (b) (c)

Figure 3.8 Top surface after 2.5 mm sectioning: (a) Gating A (b) Gating B, and (c) Gating C.

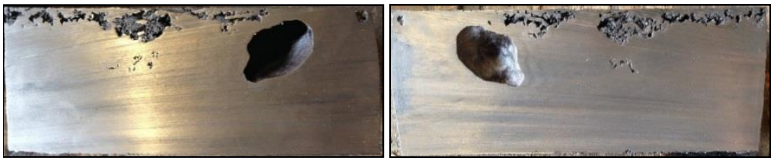

(a)

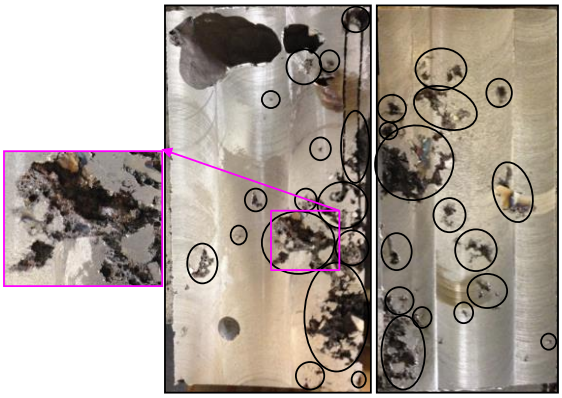

(b)

Figure 3.9 Dross inclusions in gating D: (a) Mid-plane view of the block before milling, and (b) top surface of the block after 5 mm milling.

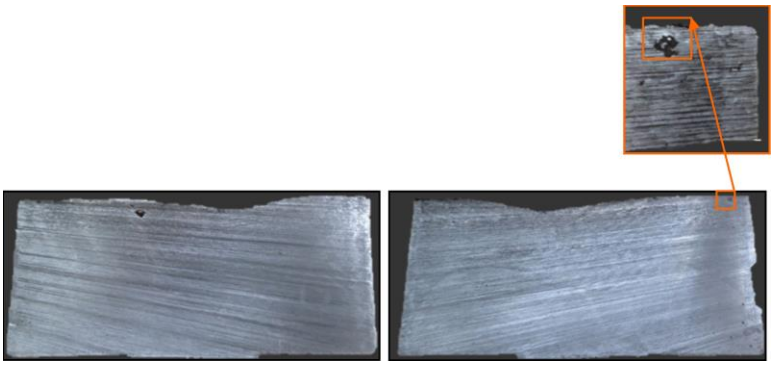

Figure 3.10 Mid-plane view of the block in gating E.

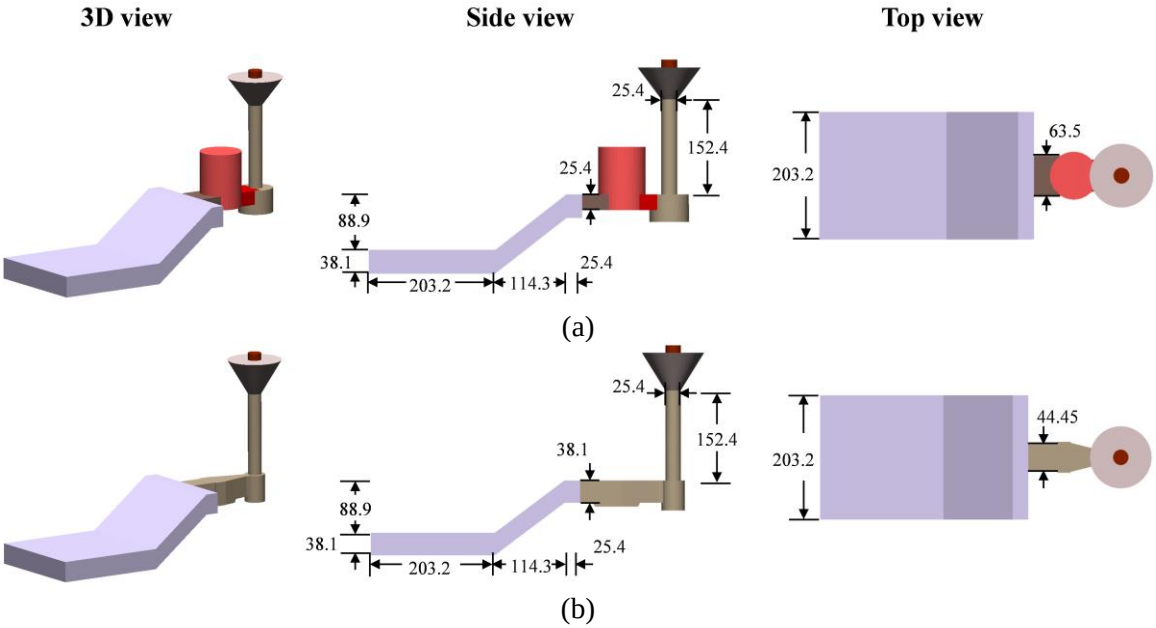

Figure 3.11 Geometry of casting with inclined surface (a) with riser, and (b) without riser. All dimensions in mm.

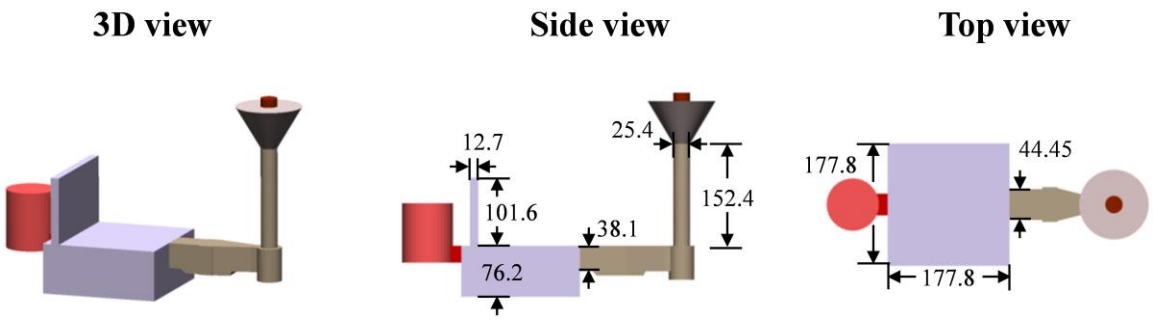

Figure 3.12 Geometry of casting with thin section. All dimensions in mm.

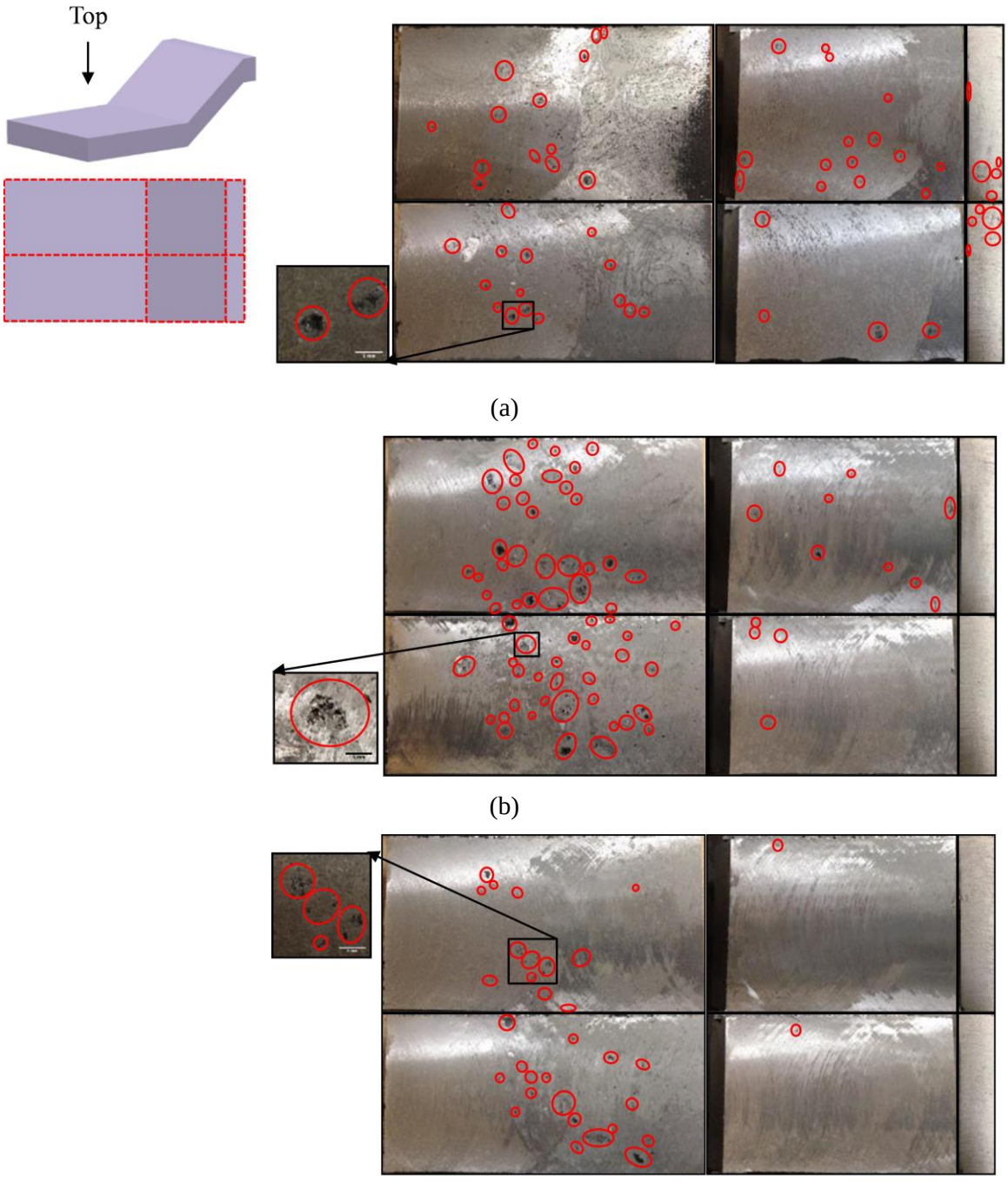

Figure 3.13 Milling results of casting with inclined surface, casting A. Top surface milled: (a) 1mm (b) 4 mm, and (c) 7 mm.

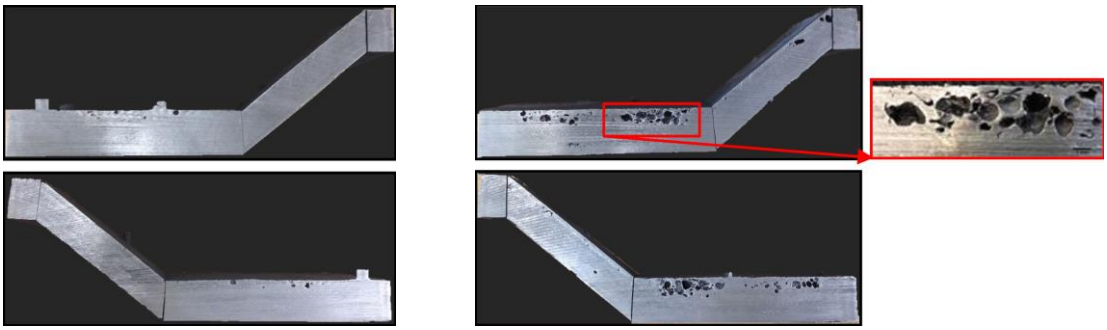

(a) (b)

Figure 3.14 Mid-plane views of castings with inclined surface (a) Casting poured at higher pouring temperature, and (b) casting poured at lower pouring temperature. Castings are poured from the same heat (Heat #3).

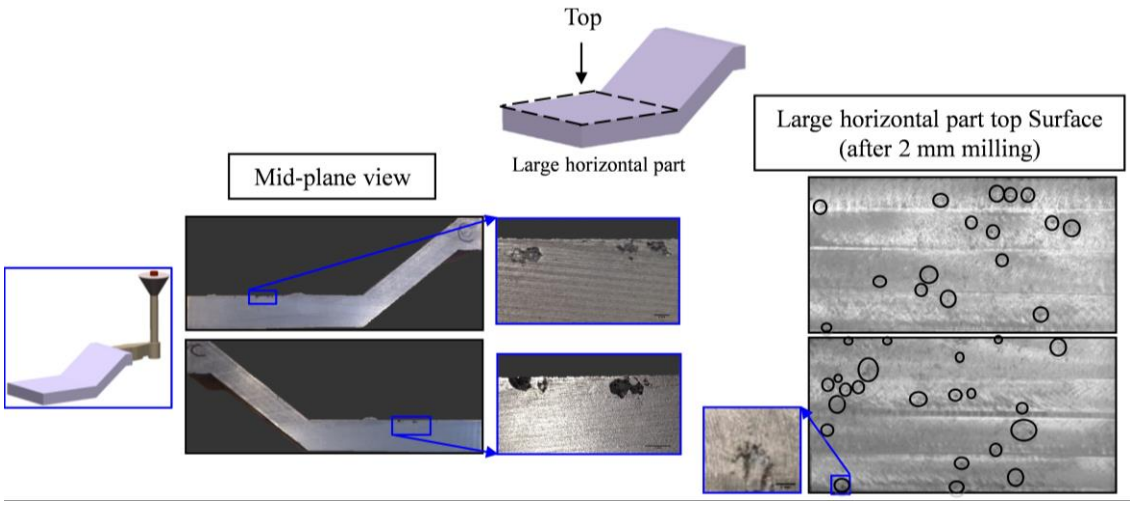

(a)

(b)

Figure 3.15 Castings with inclined surface (a) Casting without filter, and (b) casting with filter.

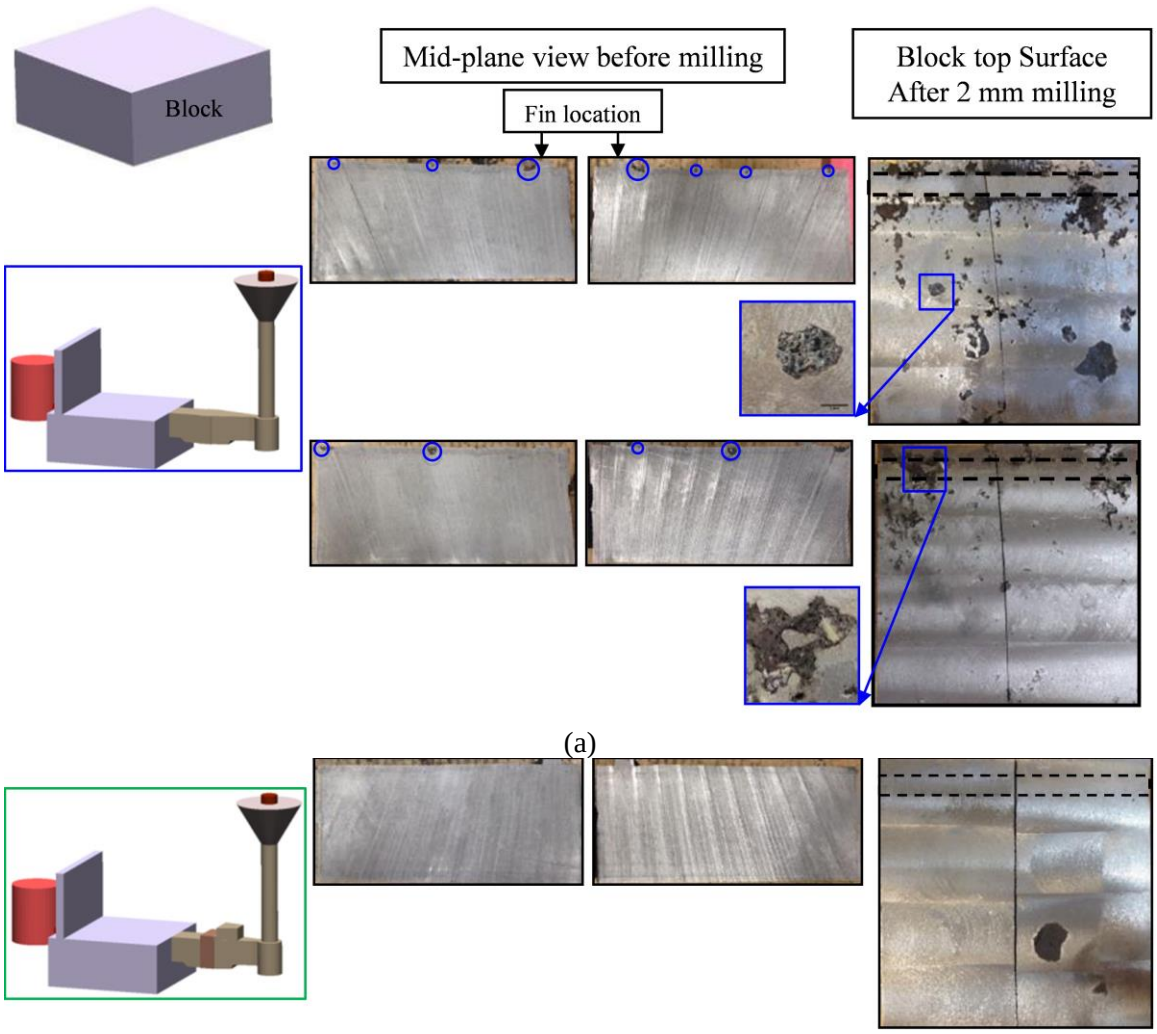

Figure 3.16 Castings with thin section (a) Casting with filter, and (b) casting without filter.

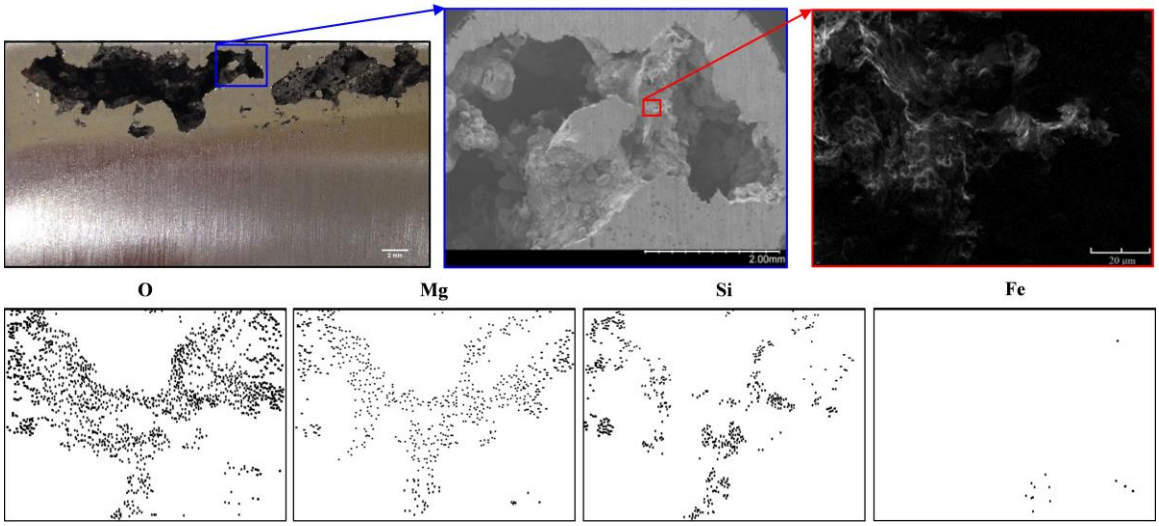

Figure 3.17 Elemental mapping of a region with dross inclusion.

CHAPTER 4: AIR ENTRAINMENT AND OXIDE INCLUSION FORMATION MODEL

4.1 Introduction

Predicting oxide inclusion formation during pouring requires a model for predicting the air entrainment. The following section describes the sub-grid model developed for calculating the local air entrainment rate as part of a one-sided computational fluid dynamics simulation. Validation of the air entrainment model is presented for a water jet impinging on a stationary pool. Section 4.4 describes the model for generation and motion of oxide inclusions.

4.2 Air Entrainment Model Description

The air entrainment calculations described here are performed as part of a standard casting filling simulation [50]. The filling simulation calculates the melt velocity by solving the Navier-Stokes equations for an incompressible flow at each time step, and the geometry of the free surface at each time step is determined using a volume tracking method (VOF method). MAGMAsoft uses a single sided VOF to track the free surface during mold filling, and the momentum equation is solved only for the liquid side, and boundary conditions are applied at the free surface.

The present model is based on the recent work of Ma et al. [4,22-24], in which the local air entrainment rate is calculated as a function of the size of the free surface disturbances. In fluid mechanics, as the inertial force dominates the viscous force the flow becomes turbulent. In turbulent flows, eddies exist in a wide range of spatial and temporal scales; these eddies can move, rotate, stretch and breakup. The largest spatial scales are of the order of the characteristic length scale of the geometry, while the smallest spatial scales can be in the order of microns. For a turbulent liquid jet, eddies raise small liquid elements at the periphery of the jet (Figure 4.1). Air is trapped beneath

these disturbances, and at the impact location the trapped air is drawn into the bulk liquid, then broken into smaller bubbles and diffused into the liquid. As shown in Figure 4.1, for a turbulent eddy of size l_e and velocity u_e the disturbance size δ is of the order of

$$\delta \sim \frac{u_e^2}{2g} \quad \rightarrow \quad \delta \sim \frac{k}{g} \tag{4.1}$$

where k (m^2 s^{-2}) is the turbulent kinetic energy and g (m s^{-2}) is the gravitational acceleration [51]. Assuming that all of the air entrainment occurs in a layer close to the interface where the disturbances exist, the volumetric rate of entrained air per unit interfacial area, q (m s^{-1}), can be estimated by the air quantity passing the inward surface Γ_e in Figure 4.1 as [4]

$$q(\boldsymbol{x}) \propto u_n(\boldsymbol{x} + \boldsymbol{n} C_1 \delta) - u_n(\boldsymbol{x}) \tag{4.2}$$

where u_n is the liquid velocity normal to the liquid-air interface, $\boldsymbol{n}$ is the unit normal vector towards the liquid, C_1 is a non-dimensional constant of $\mathrm{O}(1)$, and $\boldsymbol{x}$ is an arbitrary point on the interface.

Using the definition of a derivative

$$\frac{\partial u_n}{\partial n} = \lim_{\delta \to 0} \frac{u_n(\boldsymbol{x} + \boldsymbol{n} C_1 \delta) - u_n(\boldsymbol{x})}{C_1 \delta} \tag{4.3}$$

and combining Equations (4.1)-(4.3), the rate of air entrainment per unit interfacial area can be estimated as

$$q(\boldsymbol{x}) = \frac{C_{\mathrm{ent}}}{g} k(\boldsymbol{x}) \frac{\partial u_n}{\partial n}(\boldsymbol{x}) \tag{4.4}$$

where C_{ent} is a dimensionless entrainment coefficient that is still to be determined and $\partial u_n / \partial n$ is the normal derivative of the normal component of the liquid velocity at the interface (s^{-1}). The sign of $\partial u_n / \partial n$ determines whether air is entrained or not:

- $\partial u_n / \partial n < 0$: normal velocity decreases in the direction normal to the interface; the interface is moving with a higher velocity than the inward surface; therefore, air will be detrained rather than entrained.
- $\partial u_n / \partial n = 0$: normal velocity remains constant in the direction normal to the interface; the interface is moving with the same velocity as the inward surface; air will not be entrained or detrained.
- $\partial u_n / \partial n > 0$: normal velocity increases in the direction normal to the interface; the inward surface is moving with a higher velocity than the interface; the normal velocity if increasing away from the interface, and drawing the air pockets trapped beneath the disturbances into the liquid.

Hence, only positive values of $\partial u_n / \partial n$ will lead to air entrainment. This indicates that air entrainment occurs only when air pockets trapped in the disturbances are drawn into the bulk liquid with a rate faster than the downward motion of the liquid gas interface. Equation (4.4) indicates that the rate of air entrainment per unit interfacial area is a function of the disturbance size and the normal derivative of the normal velocity at the interface. Earlier studies have pointed out the importance of turbulent kinetic energy and differential velocity in determining the rate of air entrainment [52]. The gravitational acceleration, *g*, should be only considered as a constant in the air entrainment model, not as a factor of balance between forces.

The volumetric air entrainment rate, Q_a ($m^3\ s^{-1}$), is calculated by integrating the rate of air entrainment per unit interfacial area over the interfacial area

$$Q_a = \iint_{A_s} q \mathrm{d}A \tag{4.5}$$

where A_s is the interfacial area.

4.2.1 Turbulent Kinetic Energy

The local turbulent kinetic energy, k (m^2 s^{-2}), is the kinetic energy per unit mass associated with all eddies within the turbulent flow and is defined as

$$k = \frac{1}{2}(\overline{u_x'^2} + \overline{u_y'^2} + \overline{u_z'^2}) \tag{4.6}$$

where u_x', u_y' and u_z' are the fluctuating components of the velocity. They are defined as

$$u_x' = u_x - \overline{u_x} \tag{4.7a}$$

$$u_y' = u_y - \overline{u_y} \tag{4.7b}$$

$$u_z' = u_z - \overline{u_z} \tag{4.7c}$$

where the overbar indicates an average. In fluid mechanics, turbulence models are used for estimating the mean flow characteristics of turbulent flows. These turbulence models calculate the local turbulent kinetic energy of the flow field by solving additional equations. When using turbulence models, temporal average values are used. The method suggested here does not require any turbulence model, and for averaging purposes, it uses spatial averaging instead of temporal averaging. The spatial average is calculated as the mean value of a variable over a 27 point computational stencil in three dimensions (Figure 4.2). For the velocity components, this can be expressed as

$$\overline{u_x} = \frac{\sum_{p=1}^{27} u_{x,p}}{27} \tag{4.8a}$$

$$\overline{u_y} = \frac{\sum_{p=1}^{27} u_{y,p}}{27} \tag{4.8b}$$

$$\overline{u_z} = \frac{\sum_{p=1}^{27} u_{z,p}}{27} \tag{4.8c}$$

and

$$\overline{u_x'^2} = \frac{\sum_{p=1}^{27} u_{x,p}'^2}{27} \tag{4.9a}$$

$$\overline{u_y'^2} = \frac{\sum_{p=1}^{27} u_{y,p}'^2}{27} \tag{4.9b}$$

$$\overline{u_z'^2} = \frac{\sum_{p=1}^{27} u_{z,p}'^2}{27} \tag{4.9c}$$

4.2.2 Normal derivative of the normal component of velocity at the interface

In the casting filling simulation, the free surface is tracked using the VOF method. In this method, the computational cells in which the liquid-air interface resides have a certain liquid volume fraction, α_l, which varies from zero to unity across the interface. Using the liquid volume fraction, the normal vector at the interface and the normal velocity can be calculated, respectively, as

$$\boldsymbol{n} = \frac{\nabla \alpha_l}{|\nabla \alpha_l|} \tag{4.10}$$

$$u_n = \boldsymbol{u} \cdot \boldsymbol{n} \tag{4.11}$$

Then, the normal derivative of the normal velocity at the interface can be calculated from

$$\frac{\partial u_n}{\partial n} = \boldsymbol{n} \cdot \nabla u_n \tag{4.12}$$

With the turbulent kinetic energy $(\boldsymbol{k})$ and normal derivative of the normal velocity $(\partial u_n / \partial n)$ being calculated as described above, the entrainment coefficient, C_{ent}, is the only unknown in Equation (4.4). Based on the predicted flow velocity and the geometry of the

free surface of liquid metal from the filling simulations, the turbulent kinetic energy and the magnitude of the normal velocity gradient of the liquid metal at the liquid-air interface are calculated at each time step. The entrainment coefficient is determined by comparing predictions of the air entrainment model with experimental measurements for water.

4.2.3 OpenFOAM Simulations

The air entrainment calculations described above were first implemented in OpenFOAM [53]. OpenFOAM results are briefly discussed in the thesis. OpenFOAM is an open source toolbox which provides libraries and applications with source codes written in C++ language for the solution of continuum mechanics problem, including computational fluid dynamics. interFOAM is the multi-phase flow solver used for two immiscible and isothermal fluids. Assuming a Newtonian fluid, interFoam calculates the fluid velocity by solving the Navier-Stokes equations at each time step

$$\frac{\partial \boldsymbol{u}}{\partial t} + \boldsymbol{u} \cdot \nabla \boldsymbol{u} = -\frac{1}{\rho}(\nabla p + \mu \nabla^2 \boldsymbol{u} + \boldsymbol{f_b}) \tag{4.13}$$

while the free surface is tracked using a volume tracking method (VOF method)

$$\frac{\partial \alpha_l}{\partial t} + \nabla \cdot (\alpha_l \boldsymbol{u}) = 0 \tag{4.14}$$

where $\boldsymbol{u}$, p , and α_l are the fluid velocity vector, modified pressure scalar, and liquid volume fraction respectively. The fluid domain consists of a mixture of phases, and the liquid volume fraction value lies within the range of $0 \le \alpha_l \le 1$, where $\alpha_l = 0$ and $\alpha_l = 1$ correspond to computational stencils with continuous fluid (liquid), and dispersed fluid (air). interFoam solves a single momentum equation for the mixture of two phases. The density, ρ , and kinematic viscosity, μ , in the momentum equation are calculated based on the weighted contributions of fluid volume fraction as

$$\rho = \rho_l \alpha_l + \rho_a (1 - \alpha_l) \tag{4.15a}$$

$$\mu = \mu_l \alpha_l + \mu_a (1 - \alpha_l) \tag{4.15b}$$

In Equation (4.13), $\boldsymbol{f_b}$ is the body force term acting on the fluid; this term includes the gravity and surface tension forces. In interFoam calculations, a modified pressure is defined which accounts for the gravity force: $p_d = p - \rho \mathbf{g} \cdot \boldsymbol{x}$. The surface tension force is a function of the surface tension, σ, and the mean curvature of the free surface, κ:

$$\boldsymbol{f}_s = \sigma \kappa \nabla \alpha_l \tag{4.16}$$

$$k = -\nabla \cdot \boldsymbol{n} \tag{4.17}$$

where $\boldsymbol{n}$ is calculated according to Equation (4.10). Interface diffusion is a problem encountered when using the VOF method. To avoid this diffusion in the numerical simulations, usually a sub-grid level reconstruction of the liquid- gas interface is utilized using linear or quadratic polynomials [54]. However, in interFoam this is accomplished by modifying the advection term in Equation (4.14):

$$\frac{\partial \alpha_l}{\partial t} + \nabla \cdot (\alpha_l \boldsymbol{u}) + \nabla \cdot (\boldsymbol{u}_c \alpha_l (1 - \alpha_l)) = 0 \tag{4.18}$$

where $\boldsymbol{u}_c$ is an artificial compressive velocity term. According to this equation, the compression term is only activated at the interface; away from interface $\alpha_l = 0$ or $\alpha_l = 1$. An interface compression constant, C_α, appears in the discretized form of Equation (4.18). In all of the simulations, this constant was kept constant as C_α=1.

Three filters were applied in OpenFOAM simulations. First, a filter was applied on the normal vector and turbulent kinetic energy, k, to avoid numerical noise in the simulations: the normal vector and turbulent kinetic energy were set to zero for $\alpha_l < 0.05$ and $\alpha_l > 0.95$. Therefore, air entrainment calculations are limited to computational stencils where $0.05 \le \alpha_l \le 0.95$. According to Figure 4.3 the applied noise filter has a significant effect on removing the noise from the domain. In addition, since interFoam calculates the flow parameters in both the air and the liquid side and according to this fact

that air is entrained only at the interface and at the liquid side, an interface filter is applied as following:

- Filtering air side: If the liquid volume fraction of a computational stencil is less than 0.5 ($\alpha_l < 0.5$), then the stencil is located at the air side, and $\partial u_n / \partial n$ is set to zero.
- Filtering diffuse interface at liquid side: For interface stencils with $\alpha_l \geq 0.5$, if all the 26 neighboring stencils have liquid volume fraction larger than 0.5, $0.5 \leq \alpha_l \leq 1$, $\partial u_n / \partial n$ is set to zero; in other words, if at least one neighboring computational stencil exists with a liquid volume fraction of $\alpha_l < 0.5$, then $\partial u_n / \partial n$ is not set as zero.

Finally, the entrainment criterion is applied for interface stencils. As mentioned in section 4.2, air is entrained only for positive values of $\partial u_n / \partial n$. Therefore, the air entrainment calculations are only continued for stencils with $\partial u_n / \partial n > 0$.

Two filters were applied in MAGMAsoft simulations. To avoid numerical noise in the simulations, a filter was applied on the turbulent kinetic energy and the normal derivative of the normal velocity, and these parameters were set to zero for $\alpha_l < 0.01$ and $\alpha_l > 0.99$. The second filter is the entrainment criterion, where the air entrainment calculations are only continued for computational stencils with $\partial u_n / \partial n > 0$. Since MAGMAsoft calculates the flow parameters only for the liquid, the interface filter is not necessary.

4.3 Model Calibration and Validation for a Plunging Water Jet

Air entrainment associated with a circular water jet plunging into a quiescent pool has been studied experimentally by numerous researchers [7,9]. Their experimental data are used here to validate the present air entrainment model and to determine the entrainment coefficient, C_{ent}. The plunging water jet simulations were performed for a tank with length and width of 20 cm (8”). The quiescent pool has a height of 20 cm. The

jet enters the computational domain at the top through an inlet that represents a nozzle. The falling height (h_j) is the distance between the nozzle exit and the impact location (Figure 4.4 (a)). An overflow is designed to keep the falling height constant during a simulation. A base case result for a plunging water jet is shown in Figure 4, with the velocity distribution in the jet and the pool plotted in Figure 4.4 (a). The computed local air entrainment rate per unit of entrainment coefficient contours plotted in Figure 4.4 (b) indicate that, as expected, air entrainment is predicted to take place at the periphery of the jet where it impacts the pool. The variation of the total air entrainment rate (per unit of entrainment coefficient) in the entire computational domain is depicted in Figure 4.4 (c). It can be seen that after the initial impact of the jet, the total air entrainment rate reaches a steady state, although some fluctuations persist. For the comparison with experimental measurements shown below, the total air entrainment rate per unit of entrainment coefficient, Q_a / C_{ent}, of the plunging jet is taken as the average value during the steady state period, as illustrated in Figure 4.4 (c). This average value is divided by the volumetric flow rate of the water, Q_w, to obtain the relative air entrainment rate per unit of entrainment coefficient for a plunging jet. Figure 4.5 shows the OpenFOAM simulation results of the local air entrainment rate for two nozzle diameters at two different times. The air entrainment results shown from this section are all results obtained from MAGMAsoft.

Before determining the entrainment coefficient and comparing the present model to experiments, a computational mesh dependency study was performed. In all cases, a uniform mesh was utilized that consists of cubes of a certain side length. Figure 4.6 shows that for the plunging water jet base case just discussed, the calculated Q_a / C_{ent} values experience a slight decrease as the mesh is refined from a 3.6 mm to a 1.6 mm grid spacing. This relatively minor mesh dependency was deemed acceptable. At least four grid points are required to numerically resolve the jet itself. A uniform grid spacing of 2 mm is used for all of the following plunging water jet cases.

Studies have shown that, in addition to the turbulence level, the rate of air entrainment in plunging jets is primarily a function of the jet velocity, u_j, and diameter, d_j, at the location of the impact with the pool [7,9,13]. The liquid jet velocity, liquid jet diameter and the turbulence intensity affect the disturbance size, hence the amount of entrained air. In the simulations, they are controlled by the jet velocity and diameter at the nozzle (inlet), u_N and d_N, respectively, as well as by the falling height between the nozzle and the pool, h_j. All of these variables are indicated in Figure 4.4 (a). They are related by

$$u_N = \sqrt{u_j^2 - 2gh_j} \tag{4.19}$$

$$d_N = d_j \sqrt{\frac{u_j}{u_N}} \tag{4.20}$$

Simulations were conducted for jet velocities in the range $1 \le u_j (\mathrm{m\,s^{-1}}) \le 6$ and jet diameters in the range $10 \le d_j (\mathrm{mm}) \le 25$. The lower limit of the jet velocity range corresponds approximately to the onset of air entrainment, while the upper limit is a transition point above which air entrainment is no longer controlled by interface disturbances [13].

The air entrainment coefficient, C_{ent}, was determined by comparing the predicted steady state relative air entrainment rates to experimental measurements. In this study, the following experimental correlation for a low turbulence plunging jet proposed by Ervine and Ahmed (1982), as reported in Reference [9], is used in the calibration

$$\frac{Q_a}{Q_w} = 0.003 Fr_j^2 \tag{4.21}$$

where the jet Froude number at impact, Fr_j, is defined as

$$Fr_j^2 = \frac{u_j^2}{g d_j} \tag{4.22}$$

By minimizing the root mean square error between the predicted relative air entrainment rate values and the above experimental correlation, the entrainment coefficient was determined to be equal to $C_{ent} = 0.039$. Comparison of predicted results in OpenFOAM with measured air entrainment values gave an entrainment coefficient of $C_{ent} = 0.01$. Since OpenFOAM solves the momentum equation for both phases of air and liquid, this value seems to be a reasonable value. Figure 4.7 shows the velocity contour and the relative air entrainment rate for different liquid jet velocities. As mentioned earlier, the relative air entrainment is the time average value during the steady state period. Increasing the liquid jet velocity increases the turbulent kinetic energy, consequently increasing the disturbances size at the liquid jet periphery, therefore, increasing the relative air entrainment rate. The effect of liquid jet diameter on the relative air entrainment rate is shown in Figure 4.8. An increase in the liquid jet diameter increases the perimeter of the liquid jet, which increases the air pockets on the periphery of the liquid jet, hence the volumetric air entrainment rate. The increase in the volumetric air entrainment rate is a function of the perimeter of the liquid jet at impact location, $Q_a \propto d_j$. The relative air entrainment is the ratio of the volumetric air entrainment rate divided by the volumetric flow rate, $Q_w \propto 1/d_j^2$ for a circular liquid jet; therefore, $Q_a / Q_w \propto 1/d_j$, increasing the liquid jet diameter reduces the relative air entrainment rate.

As shown in Figure 4.9 (a), the resulting agreement between measured and predicted relative air entrainment rates is excellent over the entire Froude number range investigated in the present study. The experimental correlation indicates that the relative air entrainment rate varies with the square of the plunging jet velocity at impact. Figure 4.9 (b) shows that this trend is correctly predicted by the present model. For a jet velocity of $u_j = 1$ m/s, the air entrainment rate is measured and predicted to become negligibly small. For a jet velocity of $u_j = 6$ m/s (and $d_j = 13.5$ mm), the relative air entrainment rate approaches unity. Experimental correlation specifies that the relative air entrainment

rate is inversely proportional to the jet diameter. Figure 4.9 (b) shows that the present computations predict this trend as well. Overall, the good agreement between measurements and predictions, for a single value of the air entrainment coefficient, lends considerable confidence to the present model and computations.

Next the effect of the turbulence level of the plunging jet on the relative air entrainment rate is studied using the experimental data of Ervine et al. [7]. The turbulence intensity is defined as

$$I = \frac{\sqrt{\overline{u_N'^2}}}{\overline{u_N}} \tag{4.23}$$

As mentioned earlier, u_N is the velocity of the jet at the nozzle, and the prime and the overbar indicates the fluctuating and mean components of the velocity, respectively. In the present simulations, turbulence was induced by applying the following time-dependent sinusoidal velocity profile at the nozzle (inlet)

$$u_N = \overline{u_N} + u_N' = \overline{u_N}\left[1 + I \times \sin(\omega t)\right] \tag{4.24}$$

where ω and t are frequency and time, respectively. In accordance with the experimental study of Ervine et al. [7], the frequency was set to $\omega = 65\pi$ and the turbulence intensity to $I = 0.05 = 5\%$. Simulations were conducted for four different mean jet velocities. The effect of turbulence intensity on air entrainment is shown in Figure 4.10 for a configuration with Fr_j = 13.2. For the high turbulence intensity case, the velocity fluctuations at the nozzle exit have resulted in significant fluctuations in the relative air entrainment plot. According to Figure 4.10, the difference of relative air entrainment rate between the zero turbulence intensity and low turbulence intensity ($I = 0.004 = 0.4\%$) can be neglected. Moreover, the results in Figure 4.10 show the increase in both turbulent kinetic energy and the normal derivative of the normal component of the liquid velocity at the interface increases the air entrainment rate significantly for high turbulence intensity. Figure 4.11 shows that good agreement is obtained between the measured and

predicted relative air entrainment rates for a turbulent plunging jet. For a turbulence intensity of 5%, the relative air entrainment rate increases by a factor of approximately three relative to the low turbulence data of Ervine and Ahmed (1982). Clearly, turbulence is a major factor in air entrainment.

4.4 Modeling Oxide Inclusion Formation

The present air entrainment model is used to generate oxide inclusions by assuming that the oxygen available inside the entrained air reacts immediately with the melt constituents to form oxide inclusions. For generating inclusions and tracking them to their final location, the inclusion diameter, density, initial location and initial velocity must be known. In this model inclusions are generated based on a generation frequency, f_{gen}, at locations where air is entrained, and initialized with the local flow velocity. After generating inclusions, they are allowed to advect inside the melt with the flow. In the developed model, the inclusions are tracked in a Lagrangian sense.

4.4.1 Inclusion generation

With the volumetric air entrainment rate being calculated, the total volume of entrained, V_a (m^3), in each computational stencil in a certain period of time, Δt_{gen}, is calculated by integrating the volumetric air entrainment rate over Δt_{gen}:

$$V_a = \int_{t}^{t+\Delta t_{gen}} Q_a(t)dt \qquad (4.25)$$

The time period which the air entrainment rate is integrated, Δt_{gen}, is a user defined parameter and parametric study must be performed to study the effect of different generation frequencies on the final location of inclusions. Finally, the results should not depend on the generation frequency.

$$f_{gen} = \frac{1}{\Delta t_{gen}} \tag{4.26}$$

Based on the chemical composition of the oxide inclusions, the temperature and pressure of entrained air, a conversion constant was calculated for converting the entrained air volume into the inclusion volume. According to the calculations in section 3.4 for dross inclusion in ductile iron: $C_{cnv} = 4.1\times10^{-5}$.

$$V_{\text{inc}} = C_{cnv} V_a \tag{3.8}$$

Assuming a spherical inclusion, the inclusion diameter of each stencil after time period of Δt_{gen} is calculated according to Equation (4.27):

$$d_{inc} = (\frac{6}{\pi} V_{inc})^{\frac{1}{3}} \tag{4.27}$$

The inclusions are generated at the stencil center and localized with the flow velocity of the stencil (Figure 4.12).

4.4.2 Inclusion tracking and agglomeration

After generating inclusions, the inclusions are allowed to move with the flow. The final location of inclusions is determined by solving the equation of motion for each inclusion at each time step. In the present model, drag and buoyancy forces are the only considered forces acting on the inclusions:

$$\frac{\mathrm{d}\boldsymbol{u}_{inc}}{\mathrm{d}t} = \frac{1}{\rho_{inc}} \frac{18\mu_l}{d_{inc}^2} (\boldsymbol{u}_l - \boldsymbol{u}_{inc})(1+0.15\mathrm{Re}_{inc}^{0.687}) + (1-\frac{\rho_l}{\rho_{inc}})\mathbf{g} \tag{4.28}$$

where the *l* and *inc* subscripts indicate the quantities associated with the liquid and inclusion, respectively. Re_{inc} is the Reynolds number of the inclusion and is defined based on the magnitude of relative velocity between the melt and inclusion as

$$\mathrm{Re}_{inc} = \frac{\rho_l |u_{inc} - u_l| d_{inc}}{\mu_l} \tag{4.29}$$

The location of each inclusion is determined by solving Equation (4.30) for each inclusion at each time step:

$$\boldsymbol{u}_{inc} = \frac{\mathrm{d}\,\boldsymbol{x}_{inc}}{\mathrm{d}t} \tag{4.30}$$

where $\boldsymbol{x}_{inc}$ is the position vector of inclusion.

During their movement, inclusions can grow and stick to mold walls. Once an inclusion comes in contact to a mold wall, it is assumed to stick to the wall. As the filling proceeds the number of generated inclusions increases; tracking large number inclusions at each time step becomes computationally expensive. In addition, since larger inclusions are observed in production castings, an agglomeration algorithm is defined to reduce the computational time and further increase the size of the inclusions. In the developed model inclusions are allowed to agglomerate only at the generation times. All the inclusions within the agglomeration length are agglomerated into single new inclusion (Figure 4.13). The density of the new agglomerated inclusion is assumed to be the same as the individual inclusions involved in the agglomeration. The diameter, location and velocity of the new agglomerated inclusion is calculated according to the mass conservation, mass center equation, and linear momentum conservation, respectively:

$$d_{inc,N} = \left(\frac{6}{\pi}\sum_{j=1}^{n} V_j\right)^{\frac{1}{3}} \Rightarrow d_{inc,N} = \left(\sum_{j=1}^{n} d_j^3\right)^{\frac{1}{3}} \tag{4.31}$$

$$\boldsymbol{x}_{inc,N} = \frac{\sum_{j=1}^{n} m_j \boldsymbol{x}_j}{\sum_{j=1}^{n} m_j} \tag{4.32}$$

$$\boldsymbol{u}_{inc,N} = \frac{\sum_{j=1}^{n} m_j \boldsymbol{u}_j}{\sum_{j=1}^{n} m_j} \tag{4.33}$$

After the generation of new inclusions, all the inclusions involved in the agglomeration

are removed.

For finding a reasonable agglomeration length, L_{agg} , a similarity has been suggested between the bubble size distribution and inclusion size distribution; each inclusion in the melt corresponds to a bubble in the flow. In this model only the agglomeration of inclusions is considered, and the breakup of inclusions is neglected.

By assuming spherical bubbles, first the bubble diameter, d_b, is calculated from the entrained air volume in Equation (4.25). Then the bubbles are allowed to advect through the water. The agglomeration algorithm is applied at generation times. Different frequencies and agglomeration lengths are studied to determine the appropriate agglomeration length. The inclusion generation model is implemented in OpenFOAM [53] platform. A study has been performed in the next section to determine a reasonable agglomeration length.

4.5 Calibration of the inclusion generation and tracking model

To find an appropriate agglomeration length, L_{agg} , a set of plunging water jet experiments were selected where the bubble size distribution was provided [55]. The simulations were performed in slightly smaller tank with length and width of 20 cm. The quiescent pool has a height of 20 cm. The bubble size distribution is available for three different falling heights and seven different volumetric flow rates of water. The smallest falling height is selected and six different agglomeration lengths are studied. The generation frequency, f_{gen} , is set to 1.

Sauter mean diameter, d_{sm} , is an important mean in studying particle size distribution, it is defined as

$$d_{sm} = \frac{\sum_{i=1}^{n} d_i^3}{\sum_{i=1}^{n} d_i^2} \tag{4.34}$$

where n is the number of bubbles involved in the coalescence.

For the small falling height, $h_j = 5$ mm, the Sauter mean diameter and the maximum bubble size suggest an agglomeration length of $L_{agg} = 2$ mm (Figure 4.14). This agglomeration length is used for the three different falling heights. The Sauter mean and the maximum bubble diameter are compared in Figure 4.15. Results show that though $L_{agg} = 2$ mm gives a reasonable Sauter mean diameter for different falling heights and flow rates, the maximum bubble diameters are larger than the measured values. This is a result of considering only the bubble coalescence (agglomeration) without taking into account the bubble breakup.

Assuming ductile iron properties, a plunging jet case is selected to further study the inclusion generation and agglomeration model. According to Equation (3.6), the inclusion density $\rho_{inc} = 3140\ \text{kg m}^{-3}$ is assumed for the simulations. Parametric study is conducted for the agglomeration length and generation frequency. Figure 4.16 shows the inclusion generation at the end of $t = 2$ s for four different generation frequencies for an agglomeration length of $L_{agg} = 2$ mm.

Figure 4.17 shows the maximum and average inclusion diameters at the end of $t = 2$ s. Results indicate that the maximum inclusion diameter does not change that much above the generation frequency of 1. Eventually, the maximum inclusion diameter must be independent of the generation frequency. The average inclusion diameter is mostly affected by smaller inclusions, hence slight changes are observed for different generation frequencies.

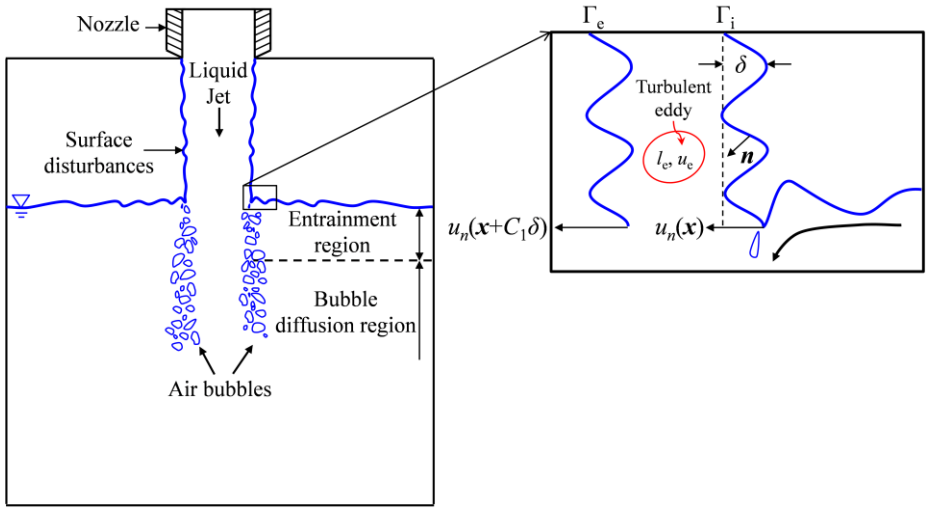

Figure 4.1 Air entrainment along the periphery of a liquid jet plunging into a quiescent pool. Adapted from Refs. [4] and [9].

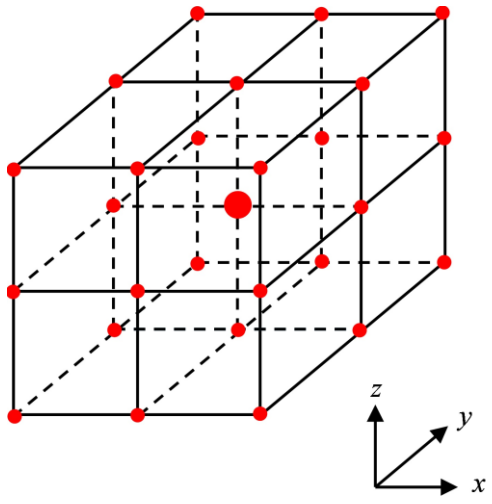

Figure 4.2 Spatial averaging for a 3D configuration. Each dot represents a computational stencil center.

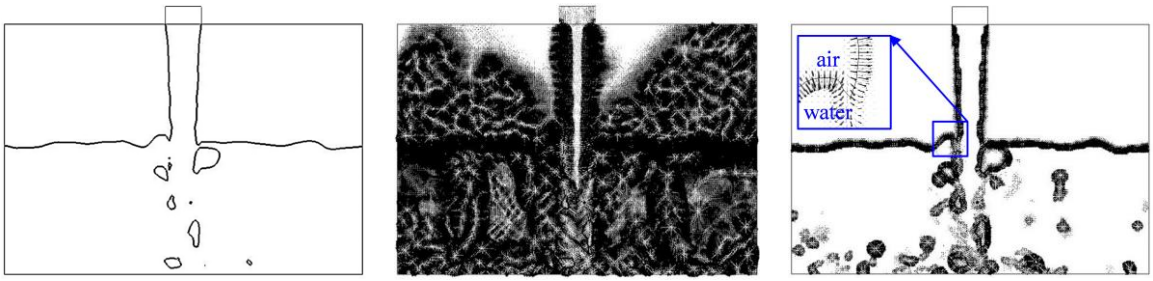

(a) (b) (c)

Figure 4.3 Effect of the applied noise filter on the normal vector, $\boldsymbol{n}$, domain: (a) Original domain showing the free surface, (b) before, and (c) after the filter is applied.

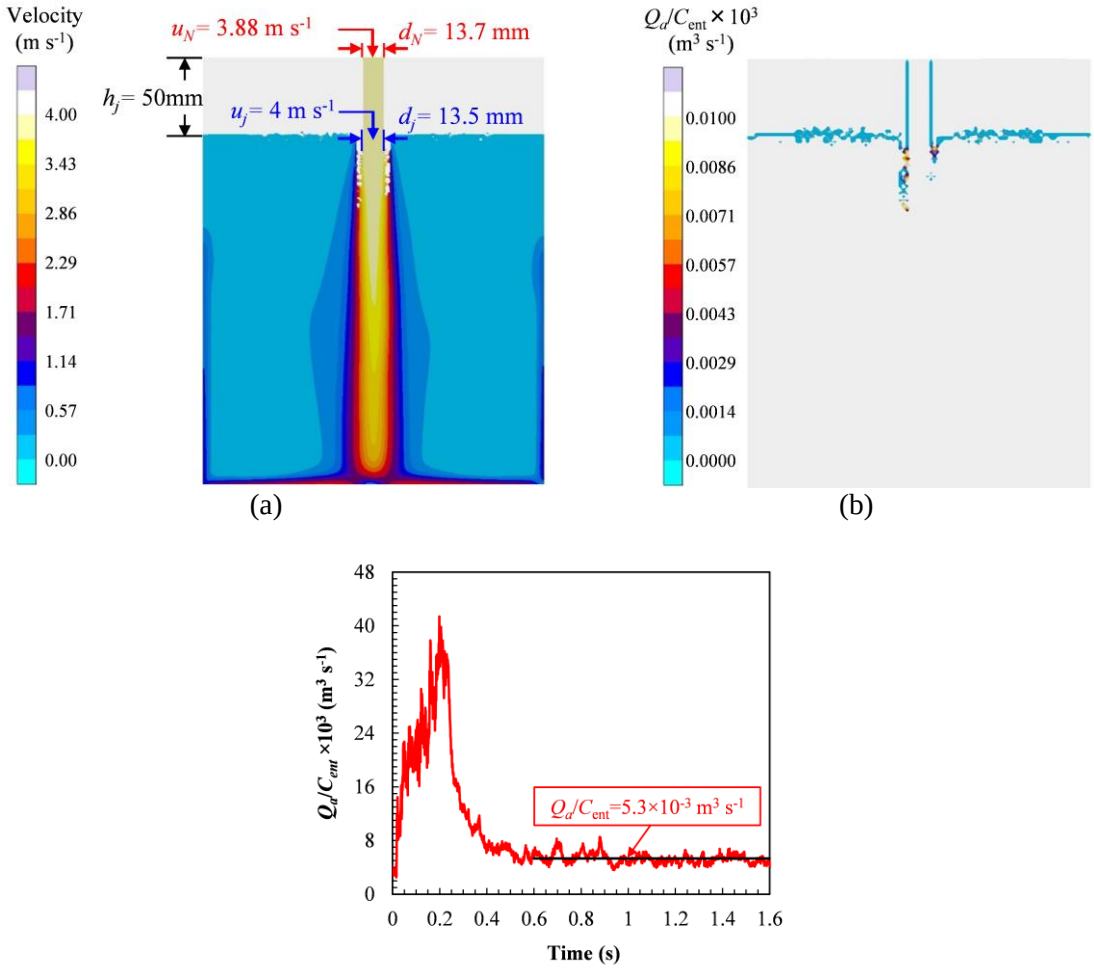

Figure 4.4 Base case plunging water jet simulation with $u_j = 4$ m s^{-1}, $d_j = 13.5$ mm, and $h_j = 50$ mm: (a) velocity contours at $t = 5$ s at the mid plane, (b) local air entrainment rate per unit of entrainment coefficient contours at $t = 5$ s at the mid plane, and (c) total air entrainment rate per unit of entrainment coefficient as a function of time.

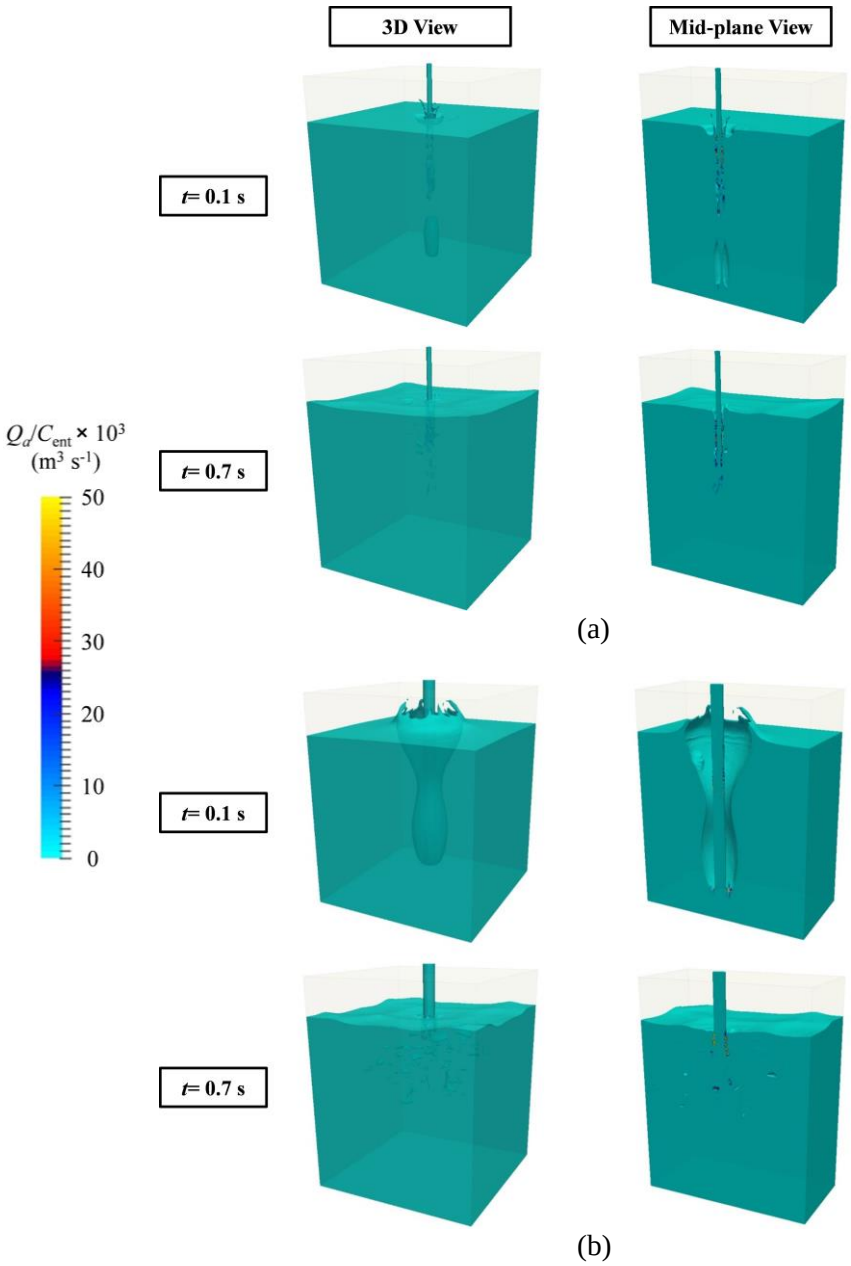

Figure 4.5 OpenFOAM simulation results of local volumetric air entrainment rate per unit interfacial area for two nozzle diameters with $u_j = 4.2$ m s^{-1}, and $h_j = 50$ mm at two different times of $t = 0.1$ s and 0.7 s: (a) $d_N = 6$ mm, and (b) $d_N = 14$ mm.

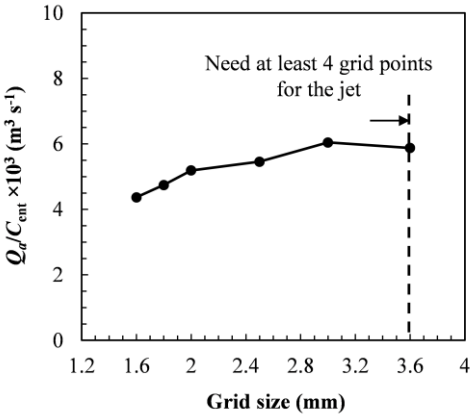

Figure 4.6 Calculated air entrainment rate per unit of entrainment coefficient as a function of grid spacing for the plunging water jet base case.

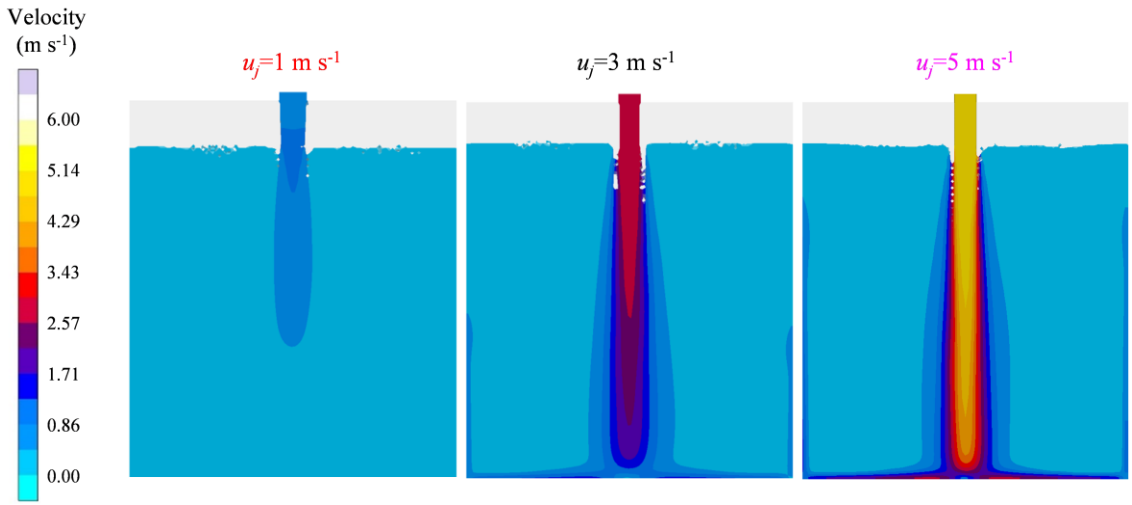

(a)

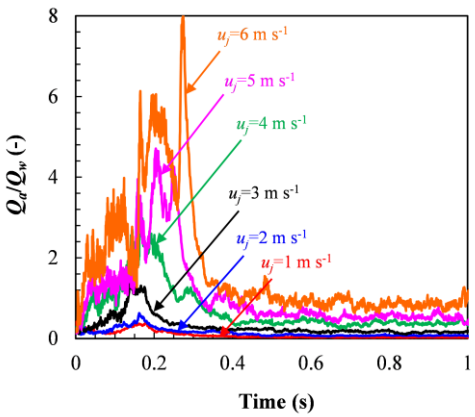

(b)

Figure 4.7 Effect of liquid jet velocity at impact, u_j: (a) velocity contours and (b) relative air entrainment.

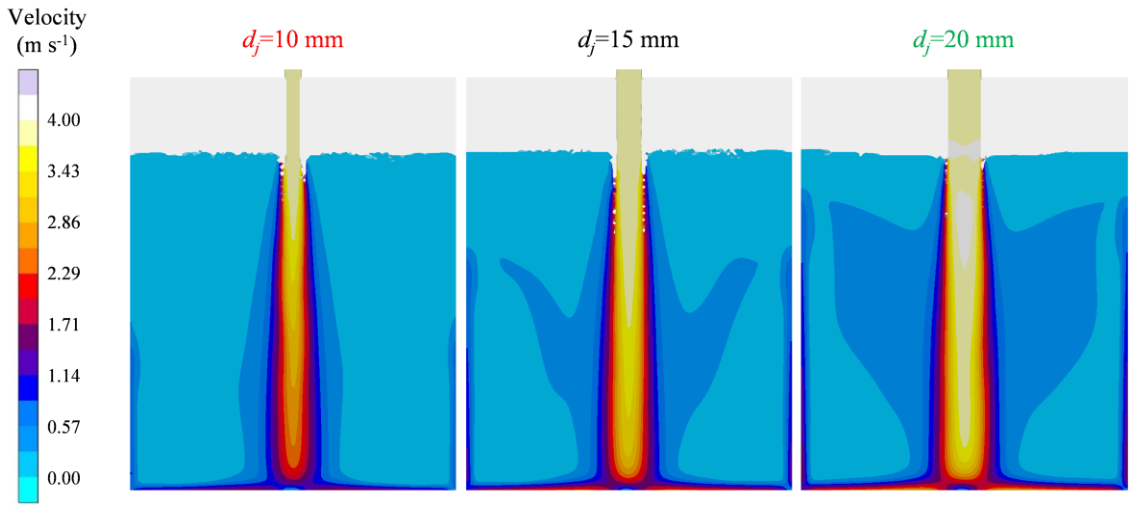

(a)

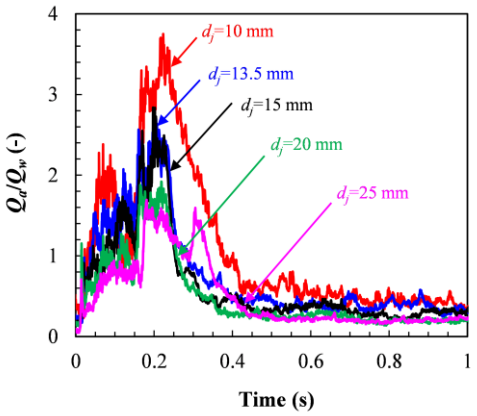

(b)

Figure 4.8 Effect of liquid jet diameter at impact, d_j: (a) velocity contours and (b) relative air entrainment.

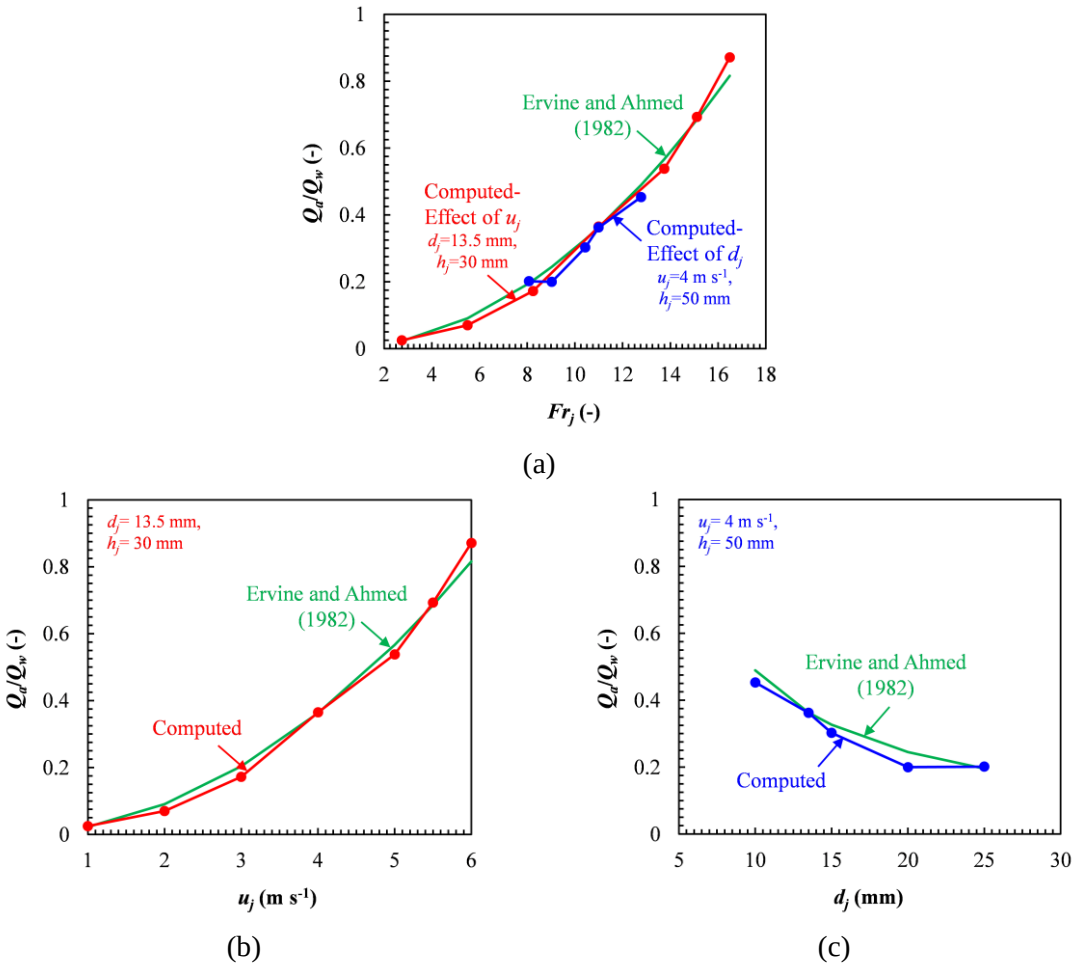

Figure 4.9 Relative air entrainment rate for a low turbulence plunging jet as a function of (a) Froude number, (b) jet velocity at impact and (c) jet diameter at impact.

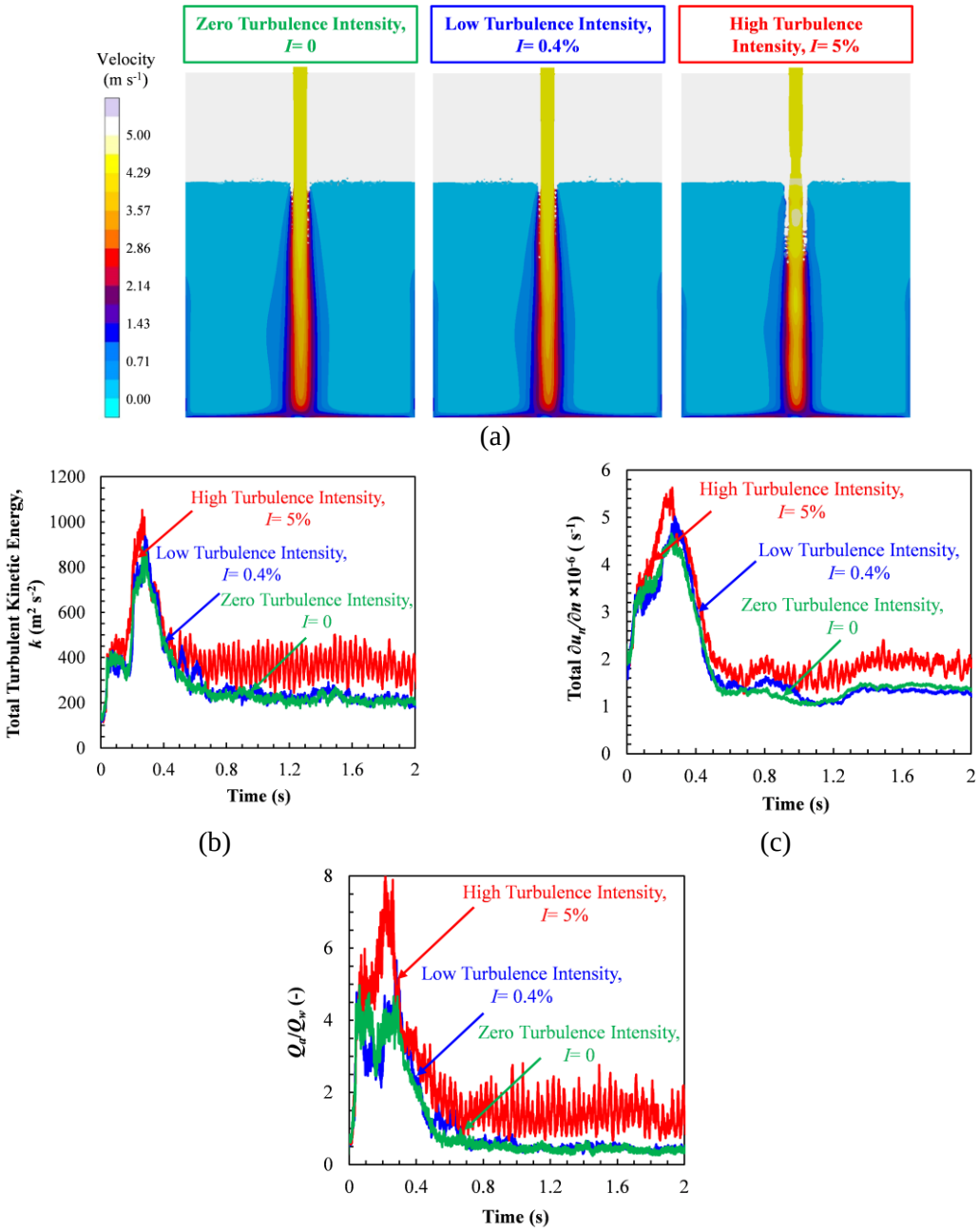

Figure 4.10 Effect of turbulence intensity on air entrainment rate for a configuration with Fr_j=13.2, u_j= 4.54 m/s and h_j= 0.1 m: (a) velocity contours shown at t =1 s for for three different turbulence intensities, (b) total turbulent kinetic energy, (c) total normal derivative of the normal component of the liquid velocity at the interface, and (d) relative air entrainment rate.

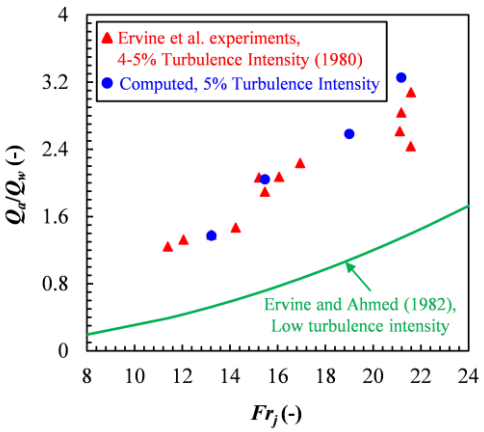

Figure 4.11 Comparison between measured and predicted relative air entrainment rates for a plunging jet with high turbulence intensity.

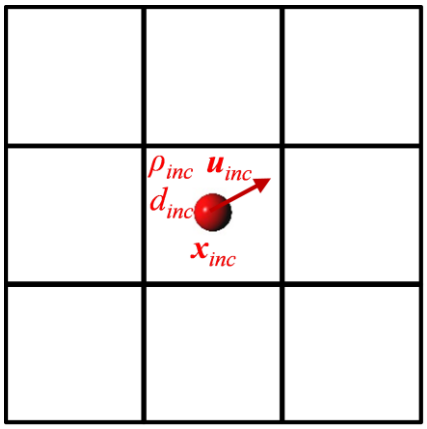

Figure 4.12 Inclusion generation at the center of a computational stencil.

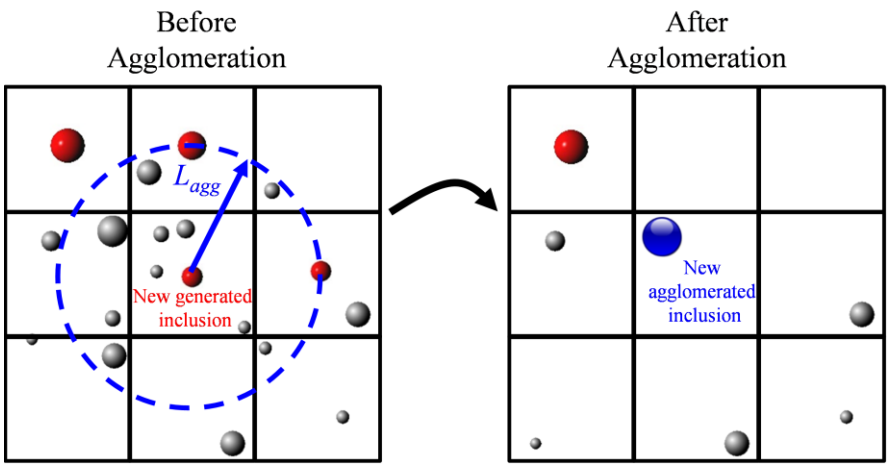

Figure 4.13 Inclusion agglomeration algorithm.

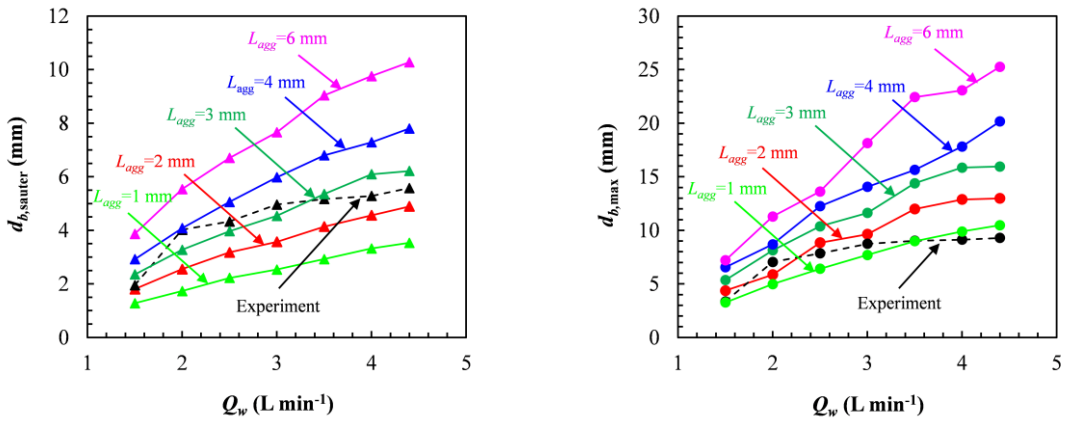

Figure 4.14 Bubble size distribution for small falling height (a) Sauter mean diameter, and (b) maximum bubble diameter.

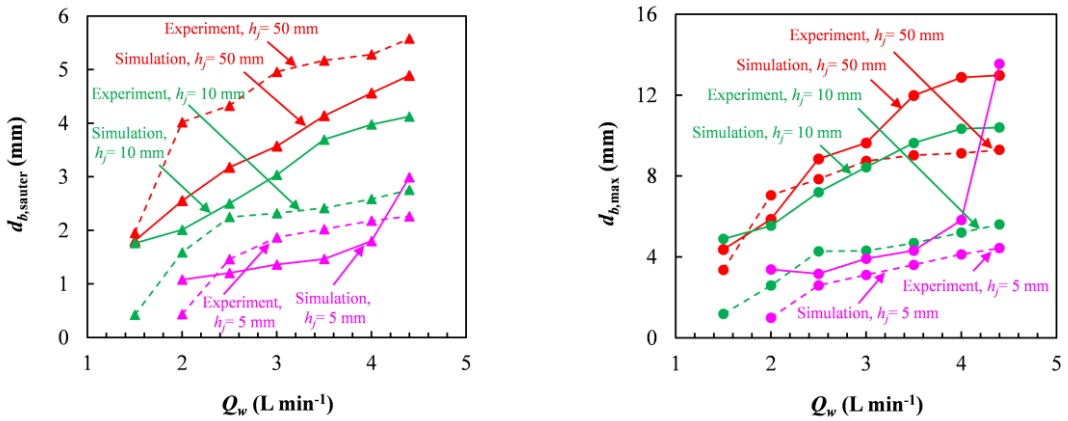

Figure 4.15 Bubble size distribution for different falling heights: (a) Sauter mean diameter, and (b) maximum bubble diameter.

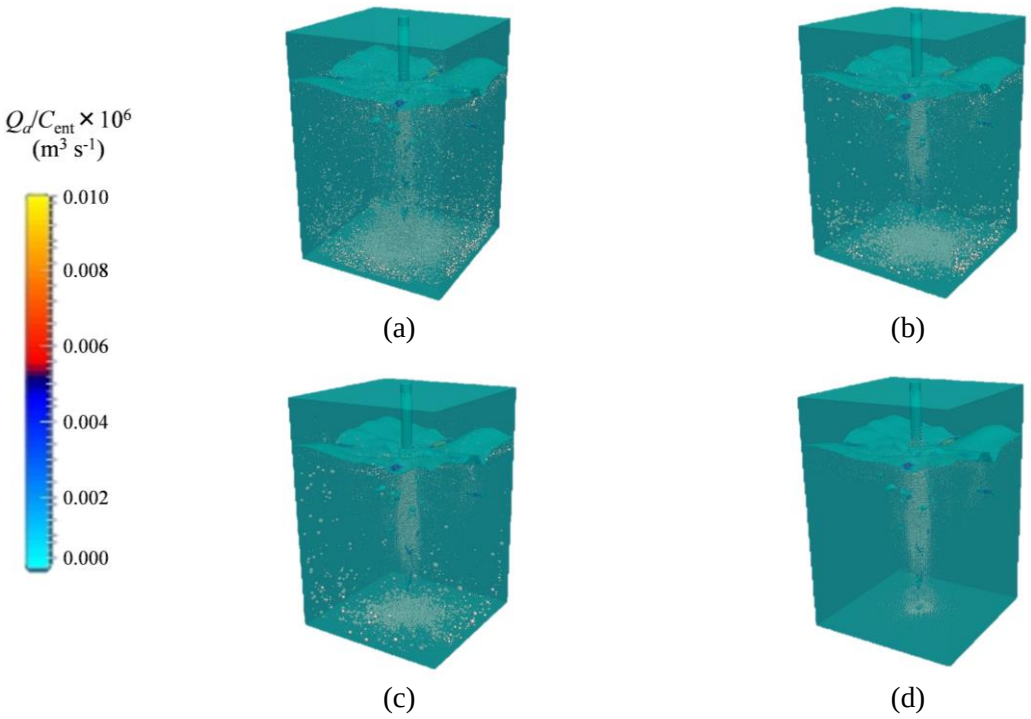

Figure 4.16 Inclusion tracking at the end of $t = 2$ s for: (a) $f_{gen} = 5$ Hz, (b) $f_{gen} = 2$ Hz, (c) $f_{gen} = 1$ Hz, and (d) $f_{gen} = 0.5$ Hz.

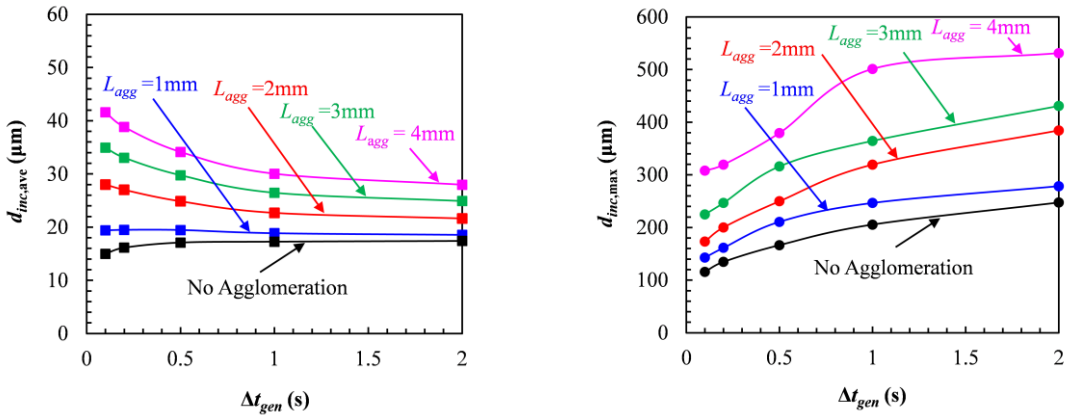

(a) (b)

Figure 4.17 Inclusion size characteristics for different generation frequencies and agglomeration lengths: (a) average inclusion diameter, and (b) maximum inclusion diameter.

CHAPTER 5: MODEL VALIDATION AND APPLICATION

5.1 Introduction

Pouring condition and gating systems affect the liquid metal flow, affecting the air entrainment, hence the formation of oxide inclusions. Using the developed air entrainment model, different filling systems and pouring conditions can be evaluated before the first casting is poured. In this chapter, first the developed air entrainment model is validated by comparing the predicted relative air entrainment volumes with measured data from water modeling experiments. Then the effect of different pouring conditions and practices on the air entrainment is studied, and finally the results of the air entrainment analysis are shown for the ductile iron experiments. The filling simulations were conducted using a commonly available casting simulation code [50] in which the present air entrainment model was implemented.

5.2 Comparison of Air Entrainment Simulations with Water Modeling Experiments

5.2.1 Water Modeling Studies

In the water modeling experiments [14,15], water was poured using a bottom pour ladle to study the effects of different variables on air entrainment.

5.2.1.1 Experimental Apparatus

For the trials, a 508 mm (20") square by 660 mm (26") deep acrylic ladle with an effective volume of approximately 0.113 m^3 (4 ft^3) was used (Figure 5.1 (a)). The ladle had a hole at the bottom where nozzles of different diameters were inserted.

The tank into which water was poured consisted of an acrylic box with a height and width of 457 mm and a length of 914 mm. Water was directly poured into the tank through the sprue. Water exiting the submerged sprue impinged on the quiescent water

pool's surface. The water tank had a removable cover plate where sprues with different lengths and diameters could be inserted. The cover plate was sealed to the tank to prevent air leakage during pouring.

5.2.1.2 Measurements

The ladle weight was measured for each pour using a 454 kg (1000 pound) load cell attached to the ladle sling. Signals from the load cell, after amplification with a precision amplifier, were sent to a data acquisition board in a desktop computer. The difference between the static weight of the ladle at the beginning and at the end of the pour provided the total water volume poured. The pouring time was measured using an electronic switch, which was installed on the lever of the stopper rod. The signals from the switch were sent to the data acquisition unit at the beginning and end of the pour, and the time difference between the start and end of each pour determined the pouring time.

Air is entrained when the water jet impinges on the quiescent pool surface. In addition to the entrained air, the impinging water caused some air displacement. The displaced and entrained air were vented into a sealed bag at the top of the tank. Before each experiment, the bag was isolated from the water tank and a vacuum pump was used to remove air from the bag. The vacuum pressure was monitored with a water manometer. At the end of the pouring, the bag was again isolated from the fill box and the vacuum pump was used to pull air from the bag through a wet test meter to measure total volume of air. The pump was stopped once a low vacuum was detected. The wet gas meter was calibrated using air displaced by a known volume of water. The volume of entrained air was estimated as the difference between the total volume of collected air and the displaced air volume (determined from the volume of water poured).

The initial water level in the tank was 25.4 mm above the bottom of the sprue (h_{sub}) to seal the entrained air in the tank. All the experimental results were expressed as the relative entrained air volume, i.e. the ratio of the entrained air volume to the volume of water poured. Based on the precision of measurement devices, the relative air entrainment precision was between 2% (at the higher air entrainment rates) and 12% (at

the lowest observed rates). The experiments were repeated three times for each configuration to measure data variability under similar pouring conditions.

5.2.1.3 Experimental Variables

A variety of pouring parameters were studied. These parameters affect the velocity, diameter, falling height and the turbulence intensity of the liquid jet. For each parameter, a high and a low value was considered. The effects of nozzle opening (open nozzle vs throttled nozzle), ladle depth, h_l, nozzle diameter, d_N, nozzle extension, h_{NE}, sprue length, h_{sprue}, were studied (Figure 5.1 (a)). Table 5.1 Overview of the measured and simulated configurations for bottom pour ladle water modeling experiments.lists all of the cases studied for the bottom pour ladle. In all of the bottom pour ladle configurations, the distance between the ladle and the pouring cup was 76.2 mm. The nozzle opening was controlled by changing the stopper opening distance, h_{SO}, in Figure 5.1 (a). For the open nozzle configurations, h_{SO} = 63.5 mm, and h_{SO} = 6.35 mm for the throttled configurations. To study the effect of total head height on the air entrainment, two different ladle depths and two sprue lengths were studied. For the full ladle and half-full ladle, the liquid height inside the ladle was 660 mm and 279 mm, respectively. For the small nozzle diameter configurations (d_N = 47.6 mm) a sprue diameter of d_{sprue} = 50.8 mm was used, while the sprue diameter was d_{sprue} = 76.2 mm for large nozzle diameter configurations (d_N = 65.1 mm). For all configurations with the nozzle extension, a h_{NE} = 127 mm extension with the same diameter as the nozzle was added to the nozzle exit. For this purpose, the ladle was raised to maintain the height between the ladle and the pouring cup. The pouring times in Table 5.1 are calculated based on the three measured pouring time for pouring 0.029 m^3 (1 ft^3) of water. The standard deviations in Table 5.1 are calculated based on the three measured pouring times for each configuration. According to Table 5.1, the standard deviations of the measured pouring times for the throttled nozzle configurations are significantly larger than the open nozzle cases. More details of the experiments can be found in References [14,15].

5.2.2 Simulation of Water Modeling Experiments

The developed air entrainment model was applied to the water modeling studies explained in the previous section. For reducing the simulation time a smaller water tank was utilized; the height and width (457 mm) were the same as the height and width of the water tank used in the above experiments, while the length of the tank was reduced from 914 mm to 660 mm (Figure 5.1 (b)) for the simulations. However, the tank size was sufficiently large that the boundaries had no influence on the impact location at the water pool surface, where air entrainment occurs. Though the simulated water tank fills faster than the water tank used in the experiments, the water level difference at the end of pouring is small (approximately 25.4 mm), and does not affect the simulation results. Similar to the experiments, in all configurations the sprue was submerged approximately 25.4 mm into the water. For all the cases, instead of modeling the ladle, the volumetric flow rate of water was calculated and used as the input for the simulations. The thermo-physical properties of water at 298 K (25 °C) were used in the simulations.

Using the simplified energy conservation equation, Equation (4.19), and the continuity equation, an equation was derived for the liquid velocity at the nozzle exit, $u_{N,th}$:

$$u_{N,th}(t) = \sqrt{2g}\, h_{l,i}^{\frac{1}{2}} - g\,\frac{A_N}{A_l}\,t \qquad (5.1)$$

where $h_{l,i}$ (m) is the initial water height inside the bottom pour ladle, respectively, and A_N (m^2) is the nozzle cross sectional area. Based on the effective volume, V_l = 0.113 m^3, and height of the bottom pour ladle, h_l = 0.66 m, an equivalent ladle cross-sectional area was calculated as $A_l = V_l / h_l$ = 0.171 m^2.

In the simulations, a friction coefficient, C_f , was applied to the liquid velocity at the nozzle exit to account for the nozzle friction. The effective liquid velocity, $u_{N,eff}$, and volumetric flow rate,

$$u_{N,eff}(t) = C_f \times u_{N,th}(t) \tag{5.2}$$

$$Q_w(t) = \frac{\pi}{4} d_N^2 u_{N,eff}(t) \tag{5.3}$$

To estimate the friction coefficient, first, the total volume of water poured was calculated by integrating the volumetric flow rate, Q_w, over the pouring time, t_{pour}

$$V_w = \int_0^{t_{pour}} Q_w(t)dt = \frac{\pi}{4} d_N^2 \times C_f \int_0^{t_{pour}} u_{N,th}(t)dt \tag{5.4}$$

Then, based on the reported pouring time for 0.029 m^3 of water, the friction coefficient, C_f, was calculated for each configuration. The calculated friction coefficients are shown in Table 5.1. The further a friction coefficient is below unity, the more friction is present in a nozzle. According to the experimental observations of the throttled nozzle, the liquid at the nozzle exit had a large turbulence level. To model the throttled nozzle configurations, turbulence intensity (Equation (4.23)) was applied at the nozzle exit in the simulations. By applying turbulence intensity, the volumetric flow rate of water at the nozzle exit was calculated as

$$Q_w(t) = \frac{\pi}{4} d_N^2 u_{N,\text{eff}} \left[1 + I \times \sin(\pi \times f \times t)\right] \tag{5.5}$$

where f and t are the frequency of the fluctuations and time, respectively. To determine the turbulence intensity for the throttled nozzle configurations, two configurations: full ladle, long sprue, no nozzle extension, with small and large nozzle diameters, were simulated with different turbulence levels and compared with the experimental measurements. Figure 5.2 (a) compares the measured and predicted relative air entrainment for five different turbulence intensities at a frequency of f = 10 Hz. Results show that increasing the turbulence intensity above 50% does not significantly affect the relative entrained air volume. In addition, a frequency dependency was studied for the full ladle, small nozzle diameter, long sprue and no nozzle extension configuration

at a turbulence intensity of I = 70% (Figure 5.2 (b)). Results indicate that the relative air entrainment volumes are independent of the frequency in the range of $5 \le f(\text{Hz}) \le 15$. Finally, a turbulence intensity of I = 70% and frequency of f = 10 Hz were selected for all of the throttled cases. Figure 5.3 compares the volumetric flow rate of water for the theoretical (friction coefficient not applied), open and throttled nozzle for the full ladle, small nozzle diameter, long sprue and no nozzle extension configuration.

The large turbulence intensity at the nozzle exit generated large disturbances at the periphery of the liquid jet. The disturbances hitting the bottom of the pouring cup blocked the flow from entering to the sprue. This caused the water to overflow from the cup before the sprue was filled during the simulations for the small nozzle diameter configurations. Therefore, for the throttled small nozzle configurations, a sprue with slightly larger diameter, d_{sprue} = 63.5 mm, and a pouring cup with larger diameter was used in the simulations. Water did not overflow the cup in the simulations of the throttled large nozzle diameter cases; therefore, the diameter of the sprue and pouring cup was not changed for these configurations. Similar to the experiments, for all the bottom pour ladle trials the stream was centered above the sprue. For each of the open and throttled nozzles, the effects of ladle depth, nozzle diameter, sprue length, and nozzle extension were studied (Figure 5.1 (b) and Table 5.1).

5.2.3 Comparison of Measurements and Predictions

Figure 5.4 shows the predicted relative air entrainment rate for two ladle depths. The comparison is made for the open nozzle, small nozzle diameter, long sprue, and no nozzle extension case. A higher head height of liquid inside the ladle produces more hydrostatic pressure above the nozzle, and consequently, a higher liquid velocity at the nozzle exit. A higher exit velocity results in a higher liquid jet impact velocity, which leads to a higher air entrainment rate. After the initial spike, the relative air entrainment rate decreases as the water tank is filled. The decrease is more pronounced for the full ladle since the water tank is filled faster than the half-full ladle case.

Figure 5.5 compares the velocity contours and air entrainment predictions for the open nozzle and throttled nozzle. The comparison is made for the full ladle, small nozzle diameter, long sprue and no nozzle extension configurations. Throttling the nozzle reduces the liquid velocity at the nozzle exit (Figure 5.5 (a)); this is shown through the decrease in the friction coefficient in Table 5.1. On the other hand, throttling the nozzle increases the turbulence intensity of the liquid jet at the nozzle exit, which increases the size of the disturbances on the liquid jet periphery, thereby increasing the air entrainment rate at the impingement point. Figure 5.5 (b) indicates the effect of increased turbulence intensity outweighs the effect of reduced liquid jet velocity. Throughout the pouring, the air entrainment rate is significantly larger for the throttled nozzle than for the open nozzle configuration.

Figure 5.6 compares the total volume of entrained air per volume of water poured for all open (Figure 5.6 (a)) and throttled (Figure 5.6 (b)) bottom pour ladle cases. The standard deviations in Figure 5.6 are calculated based on the three measured relative air entrainment volumes for each configuration. The comparison between the predicted values and experimental measurements shows overall excellent agreement. However, some discrepancies can be observed for the throttled cases. The standard deviation from the experimental results, indicate that the throttled configurations have the largest variations in the measurements. Moreover, some of the measurement results of the throttled configurations contradict previous findings of different experiments. For example, an increase in the sprue length reduces the air entrainment for the full ladle, large nozzle diameter and also for the half-full ladle, small nozzle diameter without nozzle extension cases. The authors believe that the complex behavior of the throttling process cannot be solely modeled by applying a single turbulence intensity at the nozzle exit. In addition, a throttled nozzle reduces the effective nozzle cross sectional area, which has not been accounted for in the simulations.

Comparing Figure 5.6 (a) and Figure 5.6 (b), the throttled nozzle configurations entrain significantly more air than the open nozzle. Throttling the nozzle results in relative entrained air as high as 1 cubic meter of air per cubic meter of liquid poured. Obviously, the turbulence level of the plunging liquid jet has a significant effect on the

air entrainment. The results also show that due to the higher velocity at the nozzle exit, the full ladle configurations entrain more air than the half-full ladle cases. Comparison between the small nozzle diameter and large nozzle diameter configurations indicates that increasing the stream diameter reduces the relative air entrainment volume. A larger nozzle diameter produces a higher flow rate and reduces the filling time. Additionally, according to Table 5.1, the nozzle friction is greater for the large nozzle diameters than the small nozzle diameters. This results in even lower water jet velocities at the nozzle exit for the large nozzle diameter cases, which further reduces the air entrainment. Figure 5.6 also shows that increasing the drop height of the impinging water from the nozzle increases the relative air entrainment volume. A longer sprue implies a larger drop height, which increases the water jet velocity at the impact location and, hence, the volume of entrained air.

The nozzle extension affects the open nozzle and throttled nozzle cases differently. For the open nozzle configurations, adding an extension to the exit of the nozzle applies more friction to the plunging liquid jet. The calculated friction coefficients, presented in Table 5.1, reflect this fact. This reduces the velocity of the stream exiting the nozzle extension and, therefore, the air entrainment. For the throttled nozzle cases, a nozzle extension reduces the effect of turbulence intensity. This is because the walls of the nozzle extension eliminate the free surface disturbances on the liquid jet periphery, which are generated at the nozzle exit before the extension; this in turn reduces the air entrainment. On the other hand, for both the open and throttled configurations, when a nozzle extension was used, the ladle was raised to maintain the height of the free falling jet. This increases the liquid velocity at the extension exit, which increases air entrainment. Therefore, the advantages of lower velocities due to an increase in nozzle friction for the open nozzle configurations and the reduction of turbulence intensity for the throttled cases are reduced by the effect of higher velocities at the jet impingement point caused by the increase in total head height. The simulation results, in Figure 5.6, show that the relative air entrainment volume is larger for the configurations without a nozzle extension.

It is important to point out that the open nozzle configuration with half-full ladle, large nozzle diameter, and short sprue entrains the least amount of air. A comparison of the 24 bottom pour ladle configurations shows that the amount of entrained air differs by a factor of nearly 10 between the cases with least and most entrained air. Figure 5.6 (c) compares the average of the experimental measurements and predicted relative air entrainment of the bottom pour ladle cases. An excellent agreement is obtained between the average measured and predicted relative air entrainment volumes. The results indicate that throttling the nozzle can increase the entrained air by more than three times. Therefore, the turbulence level of the liquid at the ladle exit has the most notable effect on the air entrainment. The calculated standard deviations, shown in Figure 5.6, demonstrate the throttled nozzle configurations have the largest variations in the measurements and predictions.

5.3 Pouring Conditions and Practices

The developed air entrainment is applied to investigate the effect of various gating system designs and pouring parameters on air entrainment during mold filling. In all cases, the cast part is represented by a rectangular block with a length and width of 304.8 mm (12”) and a height of 177.8 mm (7”). The material properties were taken from the standard database of the software and correspond to a low alloy steel in a furan sand mold. Though the simulations are performed for steel casting, the final comparison between different gating systems and pouring parameters should not be affected by the metal type. The pouring temperature was set to 1600 °C (2912 °F). A uniform mesh consisting of cubes with a side length of 3 mm was used in all simulations. Table 5.2 lists all of the cases studied. First, a cone shaped pouring cup on top of a vertical down sprue with a cylindrical well and a bottom ingate is investigated. The effects of the gating system pressurization state, fill time (flow rate), location of the impact of the stream from the ladle, and the head height above the cup are studied. Second, air entrainment for an

offset step pouring basin is examined. Third, the effect of the location of the ingate is studied.

5.3.1 Cone Pouring Cup with Bottom Ingate

The geometry for the gating system with a cone shaped pouring cup and a bottom ingate is provided in Figure 5.7. The casting has a pour weight of 156 kg (344 lb). First, a non-pressurized and a pressurized gating system are compared. As shown in Figure 5.8, the non-pressurized gating system features an ingate that has twice the cross-sectional area of the sprue (1:2 sprue to ingate area ratio). For the pressurized gating system, the ingate is made smaller in an attempt to keep the upstream part of the gating system filled with liquid metal during the majority of the filling process; here the area ratio is 1:0.6 (sprue to ingate). The effect of the liquid metal flow rate and, hence, the mold filling time on air entrainment and inclusion generation has been a controversial topic in the foundry industry for some time. Higher flow rates cause higher velocities in the gating system, but also reduce the time the liquid metal is exposed to oxygen. The pressurization state or degree the gating system is filled with liquid metal during pouring also depends on the flow rate. The two flow rates that are studied here are $Q_s = 1\times10^{-3}$ m^3 s^{-1} ($t_{fill} = 20$ s) and $Q_s = 0.625\times10^{-3}$ m^3 s^{-1} ($t_{fill} = 32$ s). Air entrainment can also be expected to be affected by the location where the metal stream from the ladle impacts the cone pouring cup. As illustrated in Figure 5.9 (a), a side impact and a center impact are examined. Finally, the effect of the (head) height of the stream from the ladle above the pouring cup on air entrainment is studied. As can be seen in Figure 5.9 (b), heights of $H = 50.8$ mm (2") and $H = 203.2$ mm (8") are examined. Head heights far in excess of these values are common in the foundry industry, especially when bottom pour ladles are used. Therefore, the present results are only representative of lip pour ladles that are positioned relatively close to the pouring cup.

Figure 5.10 shows a comparison of the air entrainment predictions for the non-pressurized and pressurized gating systems. The comparison is made for both side impact (Figure 5.10 (a)) and center impact (Figure 5.10 (b)). In all cases, the initial impact of the

stream from the ladle onto the cone pouring cup (for side impact) or the bottom of the sprue (for center impact) causes a large spike in the relative air entrainment rate during the first second of filling. This spike is larger for center impact, because the initial falling height (and, hence, plunging jet velocity) is larger for center than for side impact. Smaller secondary spikes can be observed at later times, which can be associated with additional plunging and splashing events. After the initial spike, the air entrainment rate is relatively constant (aside from the fluctuations), although in some cases it decreases slightly until the end of filling. The fluctuations during this period are not due to turbulence of the incoming stream from the ladle, but are generated inside the mold cavity due to unsteadiness of the flow. They are generally larger for the non-pressurized than for the pressurized gating system, indicating that the flow is steadier for a pressurized gating system. Most importantly, during the vast majority of the filling process, the air entrainment rate is significantly smaller for the pressurized than for the non-pressurized gating system. This can be attributed to the fact that for a pressurized gating system, most of the sprue fills up with liquid metal early during the filling process, causing the falling height from the pouring cup into the sprue to be less on average. A smaller falling height reduces the plunging jet velocity at impact and, hence, the air entrainment rate. For the non-pressurized gating system, the liquid metal level in the sprue is low during the majority of the filling process, resulting in a large falling height, regardless of the impact location.

Figure 5.11 shows a comparison of the air entrainment predictions for the high and low pouring rates, $Q_s = 1\times10^{-3}$ $m^3 s^{-1}$ ($t_{fill} = 20$ s) and $Q_s = 0.625\times10^{-3}$ $m^3 s^{-1}$ ($t_{fill} = 32$ s), respectively. The comparison is made for the pressurized gating system and both side impact and center impact. It can be seen that for side impact (Figure 5.11 (a)), the relative air entrainment rate throughout the filling process is lower for the higher pouring rate. This can be attributed to the fact that for the higher flow rate the gating system fills up more quickly with liquid metal. In other words, for the higher flow rate the gating system

is more pressurized. For the lower flow rate, the ingate would need to be made smaller to achieve the same pressurization state as for the higher flow rate. As already explained in connection with Figure 5.11, a higher pressurization state causes smaller falling heights and, hence, smaller velocities and air entrainment rates. For center impact (Figure 5.11 (b)), the difference in the relative air entrainment rate between the two pouring rates is negligibly small. Hence, the effect of lower velocities due to a lower pouring rate is balanced by the effect of higher velocities in the sprue due to a larger falling height.

Figure 5.12 shows a comparison of the air entrainment predictions for the small and large head heights of the stream from the ladle above the pouring cup, $H = 50.8$ mm and $H = 203.2$ mm, respectively. The comparison is made for the pressurized gating system, the high flow rate, and both side impact (Figure 5.12 (a)) and center impact (Figure 5.12 (b)). As expected, a larger head height increases the relative air entrainment rate throughout the pouring process. This can be attributed to a larger falling height causing higher velocities at the point of impact of the stream.

For all of the configurations, the total volume of entrained air is calculated by integrating the volumetric air entrainment rate over the total filling time. Figure 5.13 shows a comparison of the total volume of air entrained per volume of steel poured for all 16 cases with a cone pouring cup and a bottom ingate. The following conclusions can be drawn. Side impact of the pouring stream on to the pouring cup significantly increases air entrainment compared to center impact, where the stream never impacts the pouring cup. Increasing the head height of the ladle above the pouring cup also increases the amount of air entrained. Reducing the filling time has a beneficial effect on air entrainment and will reduce the amount of inclusions generated. Finally, using a pressurized gating system by minimizing the ingate area and keeping the gating system filled with liquid metal throughout the majority of the mold filling process reduces air entrainment. Here, it should be kept in mind that the degree of pressurization of a given gating system depends on the flow rate during filling (fill time). For center impact, pressurization is not nearly as

beneficial as for side impact. The merits of gating system pressurization have also been noted by Campbell [1]. It is important to mention that the amount of air entrained differs by almost a factor of 10 between the best and worst case in Figure 5.13.

5.3.2 Offset Step Pouring Basin

Campbell [1] has suggested the use of an offset step pouring basin in gravity casting to reduce air entrainment. Figure 5.14 shows a design for an offset step pouring basin that was patterned after Ref. [1] and sized to fit with the present casting. Filling simulations were conducted for the offset step pouring basin with a bottom ingate and $Q_s = 1\times10^{-3}$ $\mathrm{m^3\,s^{-1}}$ and $H = 203.2\,\mathrm{mm}$.

Figure 5.15 shows a comparison of the air entrainment rate predictions for the offset step pouring basin with the cone pouring cup for both side and center impact. The comparison is made for both the pressurized (Figure 5.15 (b)) and the non-pressurized (Figure 5.15 (c)) gating system. In both cases, the air entrainment rate for the offset step pouring basin is significantly lower than for the cone pouring cup. During the first 4 seconds of filling, the relative air entrainment rate for the offset step basin shows two peaks. The first peak is due to the metal stream from the ladle impinging onto the offset portion of the basin, while the second peak is due to the liquid metal from the basin plunging into the empty sprue. The fluctuations in the air entrainment rate for the offset step basin are significantly less than for the cone cup, indicating that an offset step basin aids in making the filling flow steadier. Note that the filling process takes about 4 seconds longer for the offset step basin, since it is larger than the cone cup. Figure 5.15 (d) shows a comparison of the total volume of entrained air per volume of steel. For the non-pressurized gating system, the use of an offset step basin reduces the amount of entrained air by a factor of about 2 relative to a cone cup with center impact and a factor of about 3 relative to a cone cup with side impact. For the pressurized gating system, the beneficial effect of the offset step basin is not nearly as strong, but still a factor of about 2

relative to the cone cup with side impact and a factor of about 1.6 relative to the cone cup with center impact. The conclusion that an offset pouring basin entrains less air compared to a conical pouring cup was also reached in the water modelling study performed by Afsharpour et al. [17].

5.3.3 Ingate Location

Gating a casting from the bottom is preferred in the foundry industry, but it requires a relatively long sprue and special molding techniques (e.g., tiles). Sometimes, the ingates are located on the side of the casting to take advantage of the presence of the mold parting surface. Since the parting surface is usually near the mid-height of the casting, the liquid metal will often fall over considerable heights inside the casting cavity. Such "waterfalls" inside of the mold cavity can be a large source of air entrainment. Clearly, gating a casting from the top is the least desirable configuration from an air entrainment point of view, since it leads to the largest falling heights inside the mold cavity. In order to demonstrate the effect of different ingate locations on air entrainment, filling simulations were conducted for the three geometries shown in Figure 5.16 (a). The bottom gated configuration is the same gating system that was used in the previous parametric studies. The ingate for the side gated case casting is located at the mid-height of the casting, while the casting of the top gated configuration is gated at the top. The length of the sprue and all other features were kept the same for all three ingate locations in order to allow for a more direct comparison between the different cases. Figure 5.16 shows a comparison of the air entrainment rate predictions for the three different ingate locations. The comparison is made for the cone pouring cup with side impact, pressurized gating system, $Q_s = 1\times10^{-3}$ m^3 s^{-1} ($t_{fill} = 20$ s), and $H = 203.2$ mm. It can be seen that the ingate location significantly affects air entrainment during mold filling. For the side and top gated castings, a strong jet of liquid metal emanates from the ingate and plunges onto the bottom surface of the casting cavity during large portions of the filling process

(Figure 5.16 (a)). The associated splashing inside of the casting cavity causes very high rates of air entrainment (Figure 5.16 (b)). This air entrainment subsides once the jet from the ingate is fully submerged. Figure 5.16 (c) indicates that the total volume of entrained air for the side ingate is almost 2.5 times larger than for the bottom ingate. For the top ingate the entrained air volume is more than 5 times larger than for the bottom ingate. Clearly, to produce clean castings, large "waterfalls" inside of the casting cavity should be avoided. Bottom gating systems pressurized during the whole filling are beneficial in reducing the air entrainment, hence inclusion formation.

5.4 Ductile Iron Experiments

In this section, the simulation results of the different filling systems and castings studied in sections 3.3.2 and 3.3.3 are shown. For all cases, based on the filling time (Table 3.4) and the poured volume of liquid iron, an average flow rate is calculated for each gating, and is given as the input for simulations.

5.4.1 Effect of gating system design

The relative air entrainment rate for all of the gatings is shown in Figure 5.17. The initial peak in the plot indicates the impinging of the liquid metal on the sprue base. A longer sprue indicates a larger falling height, hence larger velocity at impinging point. This has resulted in larger initial peak for gating C compared to gatings A and B. One would expect the least air entrainment for the gating C, where the liquid iron fills the mold cavity quiescently from the bottom of the casting. However, simulations show that since gating C is not pressurized sufficiently, the sprue does not fill quickly during filling (Figure 5.17 (a)). During the entire filling, the liquid impinging on the sprue has a larger falling height compared to gating B. This has resulted in slightly larger air entrainment in gating C compared to gating B. During the entire of the filling, the relative air entrainment rate for the non-pressurized gating is slightly larger than the other two

gatings, however this small difference is negligible (Figure 5.17 (b)). This is in good agreement with the milling results of castings A, B and C (Figure 3.8). Comparison of the predicted results for gatings D and E (Figure 5.17 (c)) show that a casting with bottom-gated vertical gate entrains less air compared to the top gated casting. In gating D, air is entrained significantly at the sprue well, and further once liquid iron impinges on the bottom of the casting. For the bottom gated casting, gating E, once the liquid jet enters the casting, the fountain formed at the entry of the casting increases the volumetric air entrainment rate (approximately at $t = 1.2$ s- Figure 5.17 (c)) but the volumetric air entrainment rate reduces as the filling proceeds. Figure 5.17 (d) compares the relative air entrainment volumes for different gating systems. Results show that gating E entrains the least air during filling. This is in agreement with the experimental findings. The results further prove that air entrainment increases for non-pressurized gating systems. For gravity filling systems, bottom gated castings with slight pressurization are beneficial in reducing the total volume of entrained air, hence oxide inclusion formation.

5.4.2 Complex geometries and effect of filter

Figure 5.18 (a) shows the air entrainment results for the casting with inclined surface. The large initial spike at $t = 0.5$ s in the relative air entrainment plot corresponds to the impingement of the liquid iron on the sprue base. Once the liquid iron reaches the inclined portion, significant free surface turbulence occurs ($4 < t(\text{s}) < 5$), and the air entrainment starts increasing until it impinges on the end wall of the horizontal part. The returning and breaking waves further increase the air entrainment rate. Due to increased filling time, the casting with riser (Casting A) entrains slightly more air compared to the casting without riser. The small difference in the relative entrained air between castings B and C is due to the filter effect; one of the major effects of the filter is to reduce the velocity of the flow beyond the filter. The reduced flow velocity after the filter reduces the air entrainment rate.

The air entrainment results for the casting with thin section are shown in Figure 5.18 (b). The secondary peak in the air entrainment plot corresponds to the time when the liquid iron emanates from the gate and impinges on the bottom of the casting. Similar to the casting with inclined surface, due to the reduced velocity, the casting with filter entrains slightly less air compared to the casting without filter.

Overall, a good agreement is achieved between the predicted and experimental findings. The promising results obtained in this study further validate the developed air entrainment model.

Table 5.1 Overview of the measured and simulated configurations for bottom pour ladle water modeling experiments.

	Trial	Ladle depth	Nozzle diameter (mm)	Nozzle extension	Sprue length (m)	Pouring time, t_{pour} (s)	Standard deviation of pouring times, (-)	Friction coefficient, C_f (-)
Open Nozzle	1	Full	47.6	No	0.13	5.12	0.003	0.93
	2	Full	47.6	No	0.26	5.12	1.2×10^{-5}	0.93
	3	Full	47.6	Yes	0.13	5.68	0.002	0.85
	4	Full	47.6	Yes	0.26	5.67	0.005	0.85
	5	Full	65.1	No	0.13	3.91	0.007	0.68
	6	Full	65.1	No	0.26	3.91	1.8×10^{-6}	0.68
	7	Half-full	47.6	No	0.13	8.37	0.014	0.99
	8	Half-full	47.6	No	0.26	8.36	0.021	0.99
	9	Half-full	47.6	Yes	0.13	9.17	0.007	0.93
	10	Half-full	47.6	Yes	0.26	9.17	0.011	0.93
	11	Half-full	65.1	Yes	0.13	6.22	0.013	0.78
	12	Half-full	65.1	Yes	0.26	6.25	0.017	0.78
Throttled Nozzle	13	Full	47.6	No	0.13	12.2	0.106	0.48
	14	Full	47.6	No	0.26	12.2	0.013	0.48
	15	Full	47.6	Yes	0.13	10.0	0.021	0.52
	16	Full	47.6	Yes	0.26	9.95	0.007	0.52
	17	Full	65.1	No	0.13	7.9	0.003	0.42
	18	Full	65.1	No	0.26	7.85	0.055	0.42
	19	Half-full	47.6	No	0.13	21.2	0.141	0.59
	20	Half-full	47.6	No	0.26	20.6	0.019	0.60
	21	Half-full	47.6	Yes	0.13	16.4	0.051	0.64
	22	Half-full	47.6	Yes	0.26	18.5	0.033	0.61
	23	Half-full	65.1	Yes	0.13	13.8	0.053	0.60
	24	Half-full	65.1	No	0.26	13.9	0.265	0.60

Table 5.2 Overview of the cases simulated for studying the effect of pouring conditions and practices on the entrained air.

	Trial	Gating Arrangement	Pouring Cup/Basin	Impact Location	Pouring Rate, $Q_s \times 10^3$ ($m^3 s^{-1}$)	Head Height, H (mm)
Non-Pressurized	1	Bottom	Cone cup	Side	1	203.2
	2	Bottom	Cone cup	Side	1	50.8
	3	Bottom	Cone cup	Side	0.625	203.2
	4	Bottom	Cone cup	Side	0.625	50.8
	5	Bottom	Cone cup	Center	1	203.2
	6	Bottom	Cone cup	Center	1	50.8
	7	Bottom	Cone cup	Center	0.625	203.2
	8	Bottom	Cone cup	Center	0.625	50.8
	9	Bottom	Offset step basin	Side	1	203.2
Pressurized	10	Bottom	Cone cup	Side	1	203.2
	11	Bottom	Cone cup	Side	1	50.8
	12	Bottom	Cone cup	Side	0.625	203.2
	13	Bottom	Cone cup	Side	0.625	50.8
	14	Bottom	Cone cup	Center	1	203.2
	15	Bottom	Cone cup	Center	1	50.8
	16	Bottom	Cone cup	Center	0.625	203.2
	17	Bottom	Cone cup	Center	0.625	50.8
	18	Bottom	Offset step basin	Side	1	203.2
	19	Side	Cone cup	Side	1	203.2
	20	Top	Cone cup	Side	1	203.2

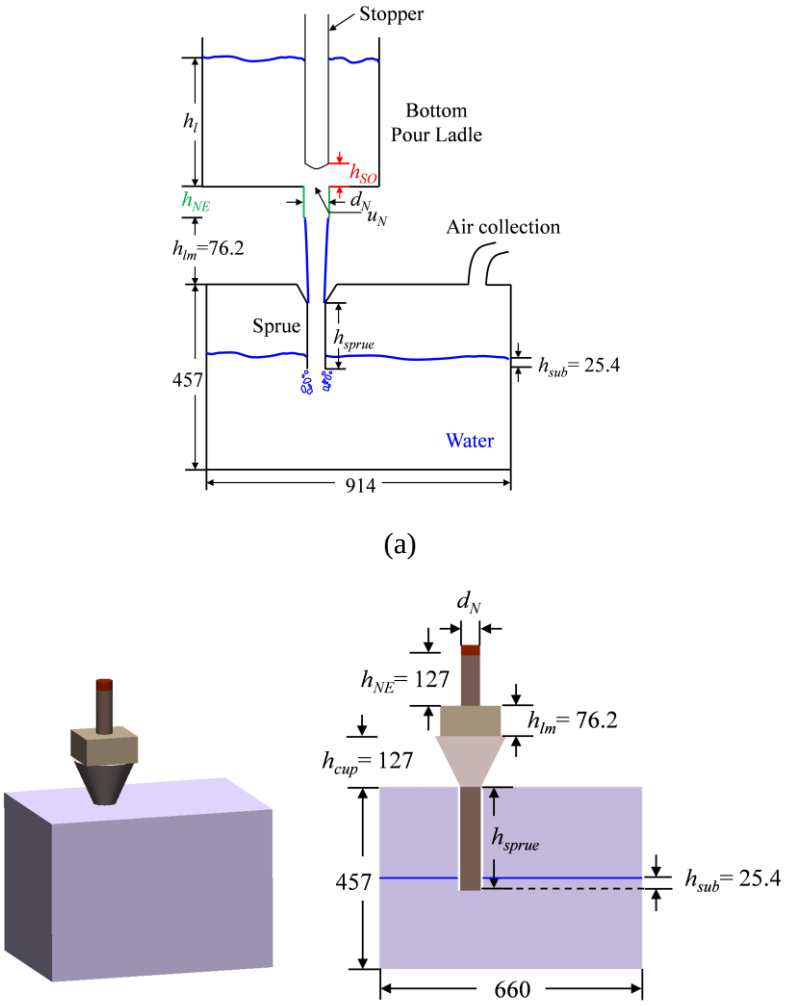

Figure 5.1 Bottom pour ladle: (a) Experimental configuration and (b) simulation setup (3D and mid-pane view). All dimensions in mm.

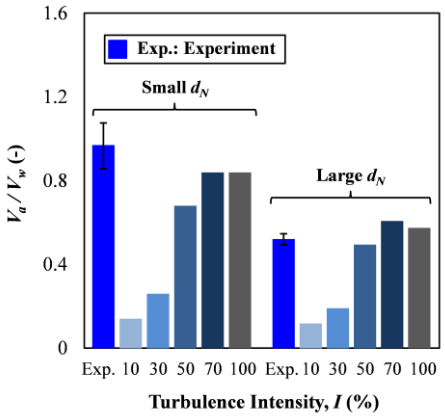

(a)

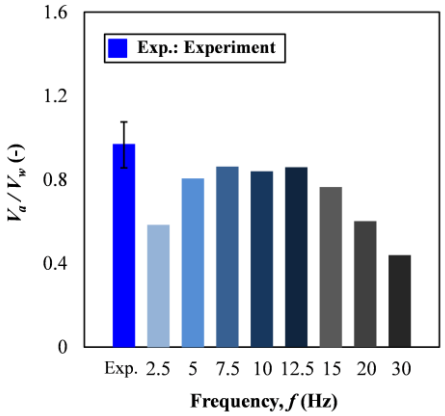

(b)

Figure 5.2 Predicted relative air entrainment rate volume as a function of: (a) turbulence intensity for the full ladle, long sprue ($h_{sprue} = 0.26$ m) and no nozzle extension configuration at a frequency of $f = 10$ Hz for small and large diameters., and (b) frequency for the full ladle, small nozzle diameter ($d_N = 47.6$ mm), long sprue ($h_{sprue} = 0.26$ m) and no nozzle extension configuration at a turbulence intensity of $I = 70$ %.

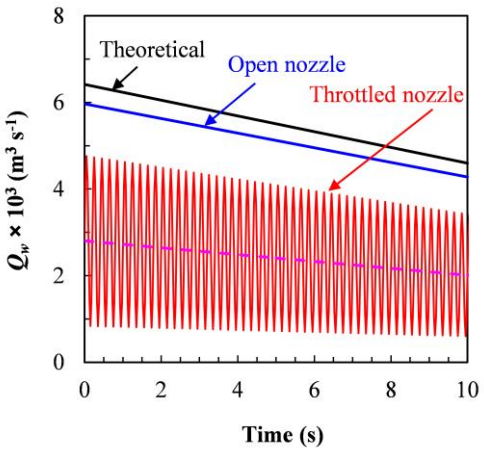

Figure 5.3 Volumetric water flow rate as a function of time for the theoretical (no friction applied), open nozzle and throttled nozzle for the full ladle, small nozzle diameter, long sprue and no nozzle extension configuration.

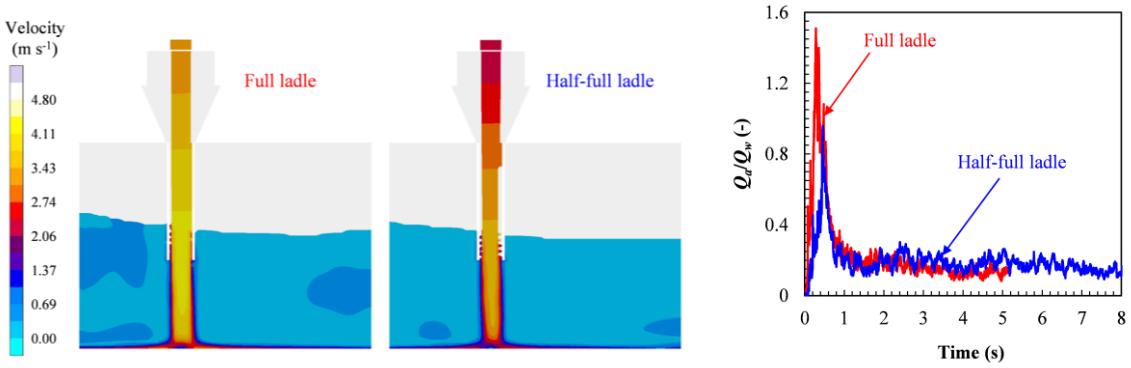

(a) (b)

Figure 5.4 Predicted relative air entrainment rate volume as a function of: (a) turbulence intensity for the full ladle, long sprue ($h_{sprue} = 0.26$ m) and no nozzle extension configuration at a frequency of $f = 10$ Hz for small and large diameters., and (b) frequency for the full ladle, small nozzle diameter ($d_N = 47.6$ mm), long sprue ($h_{sprue} = 0.26$ m) and no nozzle extension configuration at a turbulence intensity of $I = 70\,\%$.

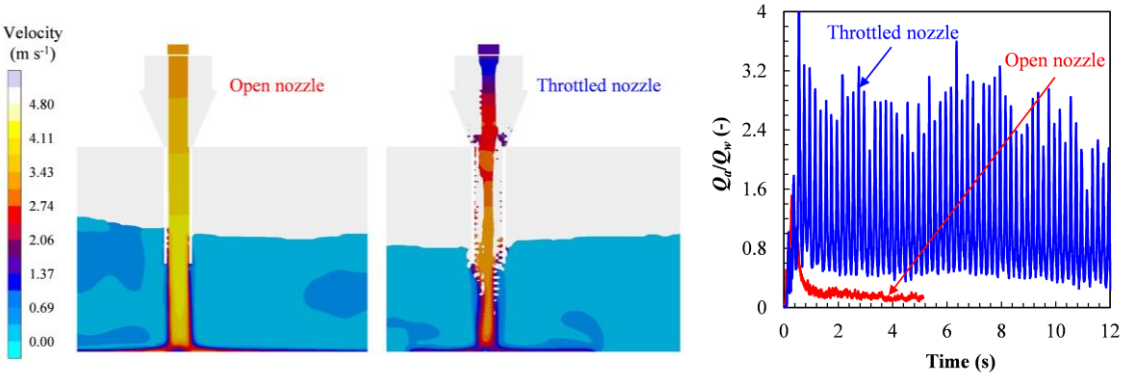

(a) (b)

Figure 5.5 Effect of the nozzle opening on the variation of the relative air entrainment rate for full ladle, small nozzle diameter ($d_N = 47.6$ mm), long sprue ($h_{sprue} = 0.26$ m) and no nozzle extension configuration: (a) The velocity contours at time of $t = 2$ s for open nozzle (left) and throttled nozzle (right), and (b) relative air entrainment rate.

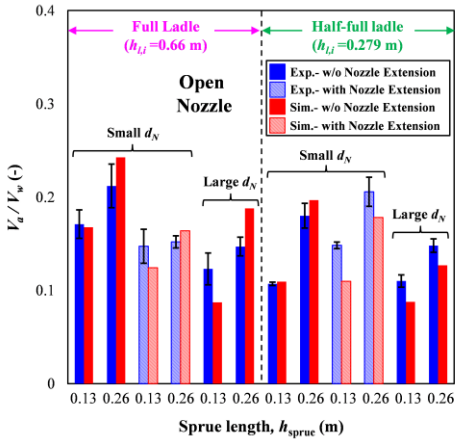

(a)

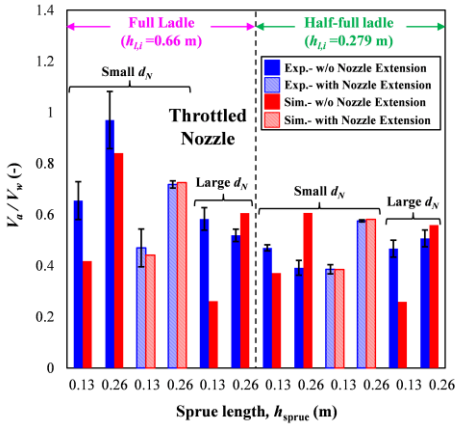

(b)

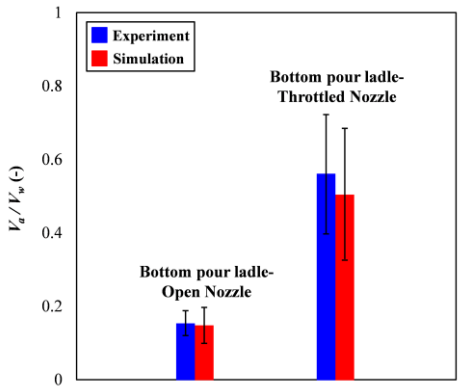

(c)

Figure 5.6 Comparison of the predicted relative entrained air volumes with measurements for bottom pour ladle configurations: (a) open nozzle, (b) throttled nozzle, and (c) average values.

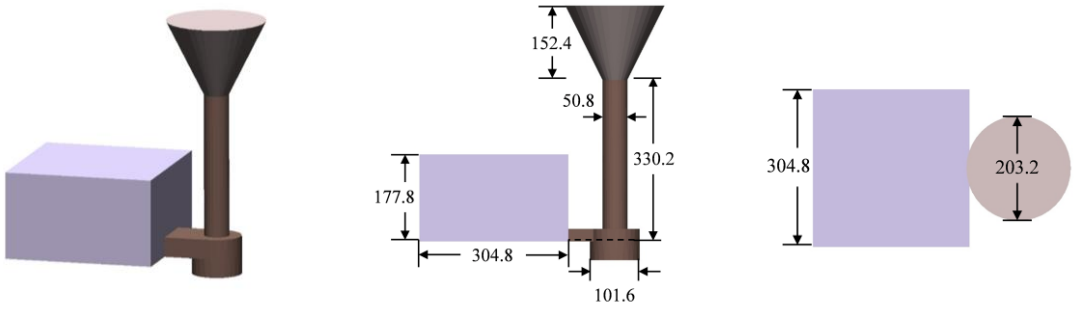

(a) (b) (c)

Figure 5.7 Gating system and casting geometry for the cone pouring cup with bottom ingate cases: (a) isometric view, (b) front view and (c) top view. All dimensions in mm.

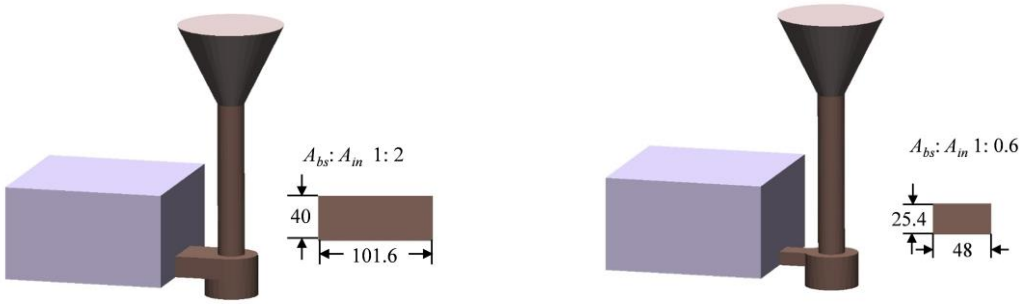

(a) (b)

Figure 5.8 Ingate geometry for (a) the non-pressurized gating system and (b) the pressurized gating system. All dimensions in mm.

(a) (b)

Figure 5.9 Geometries for (a) the side and center impact locations and (b) the two different head heights.

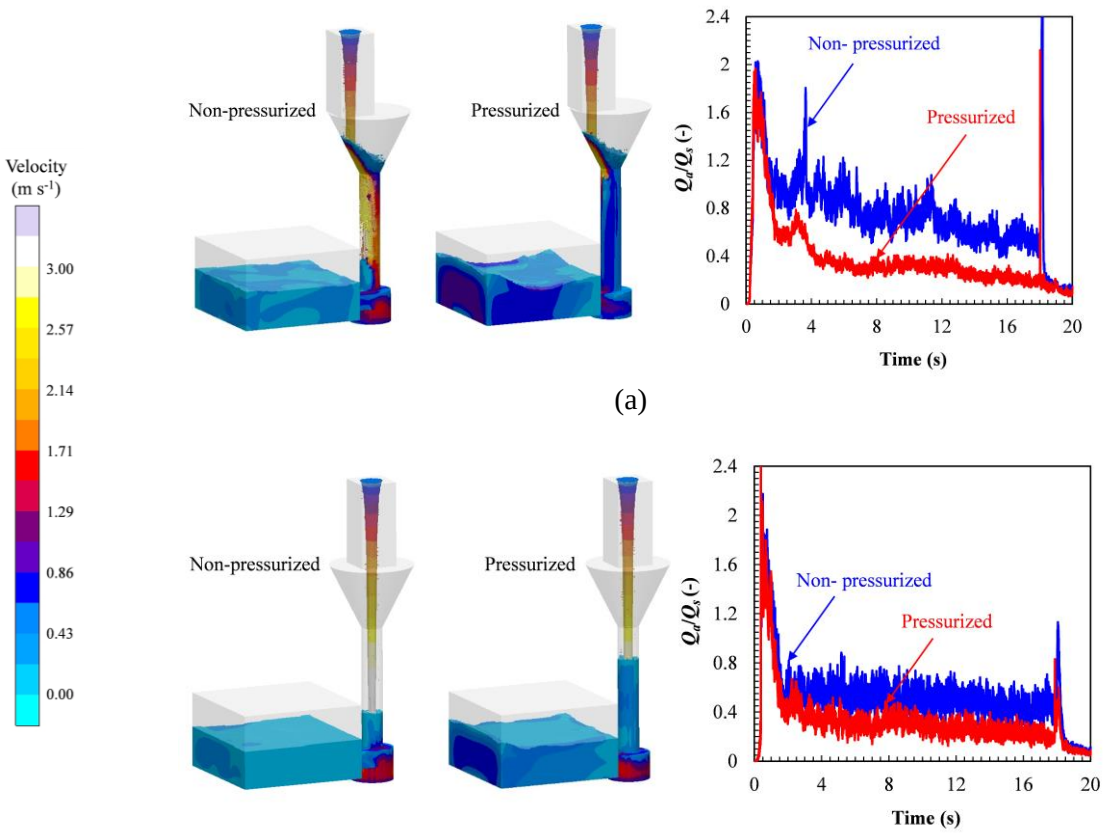

Figure 5.10 Effect of the gating system pressurization state on the variation of the relative air entrainment rate (plots on the right) for $Q_s = 1\times10^{-3}$ m^3 s^{-1} ($t_{fill} = 20$ s) and $H = 203.2$ mm: (a) side impact, (b) center impact. The velocity contours are shown at a time of 10 s.

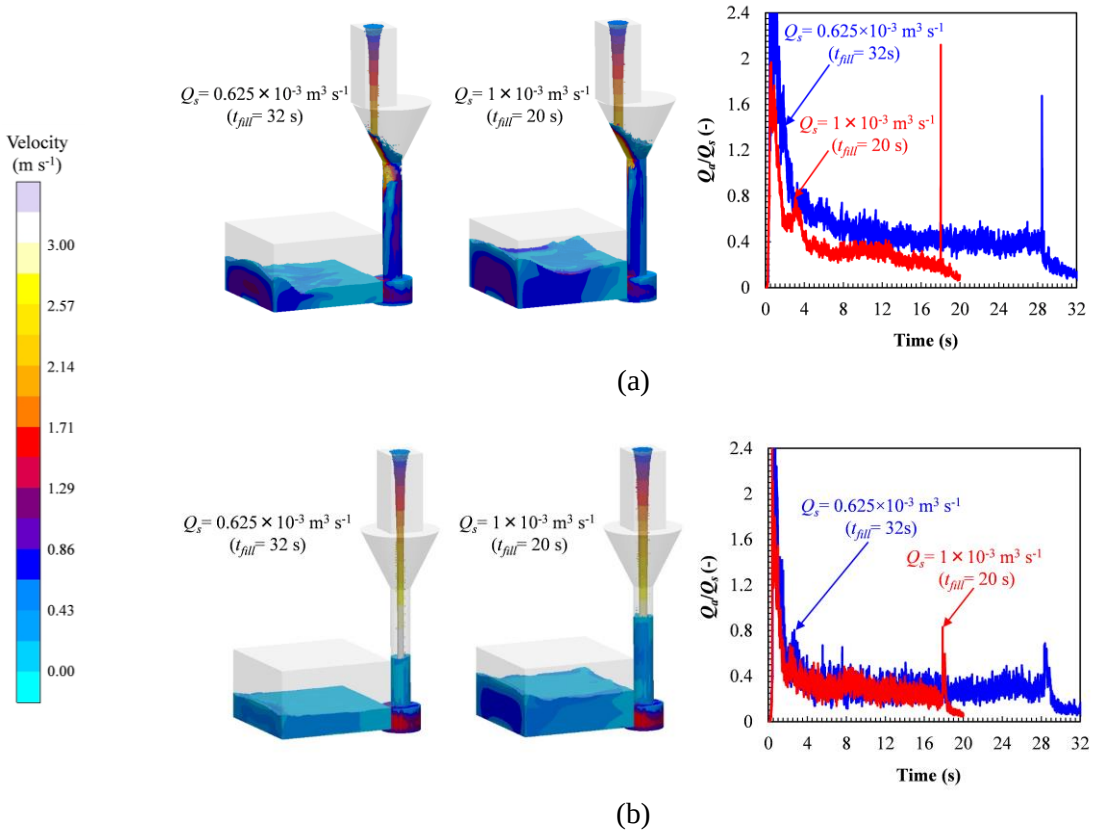

Figure 5.11 Effect of the liquid metal flow rate, Q_s, on the variation of the relative air entrainment rate (plots on the right) for a pressurized gating system and $H = 203.2$ mm: (a) side impact, (b) center impact. The velocity contours are shown at a time of 10 s.

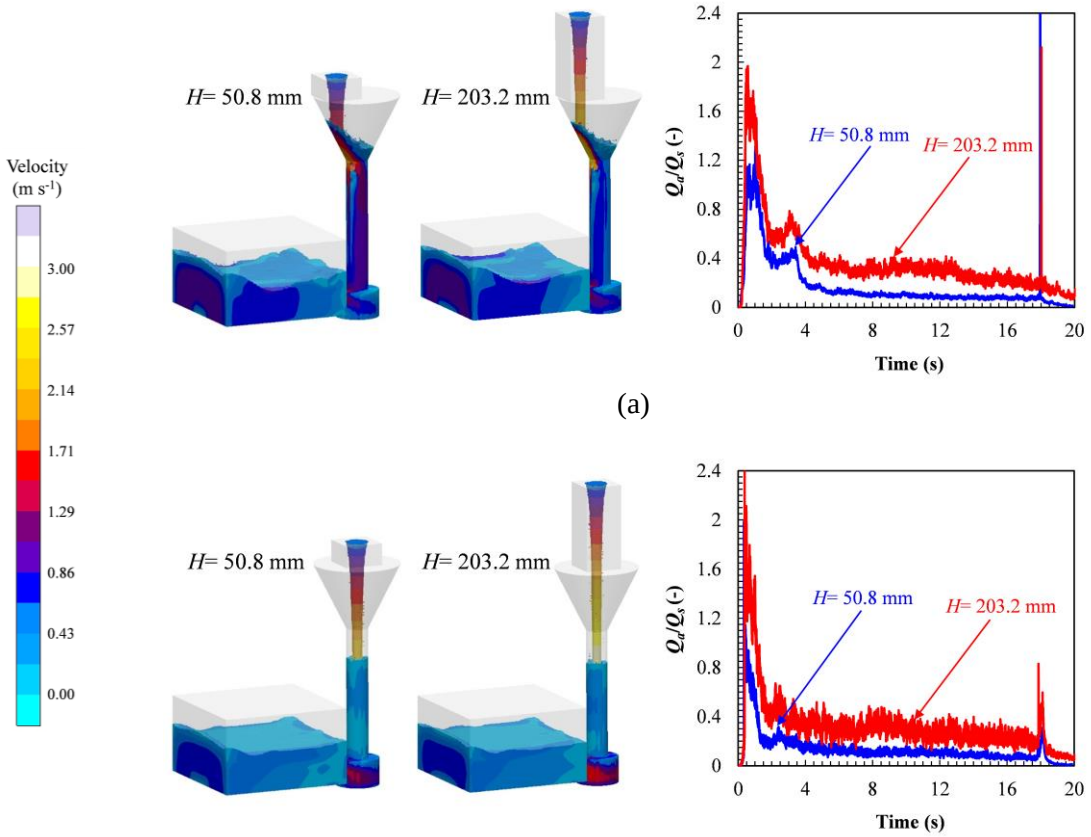

Figure 5.12 Effect of the head height, H, on the variation of the relative air entrainment rate (plots on the right) for a pressurized gating system and $Q_s = 1\times10^{-3}$ m^3 s^{-1} ($t_{fill} = 20$ s): (a) side impact, (b) center impact. The velocity contours are shown at a time of 10 s.

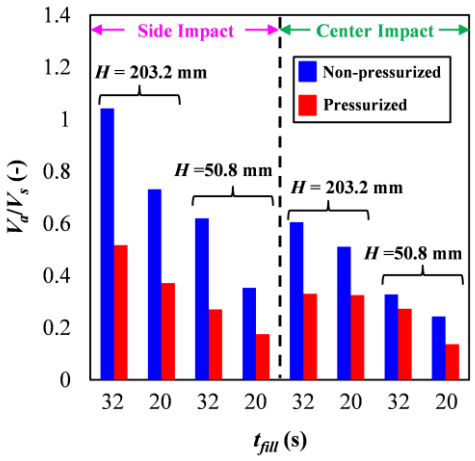

Figure 5.13 Comparison of the predicted total relative entrained air volumes for the 16 cases with a cone pouring cup and bottom ingate.

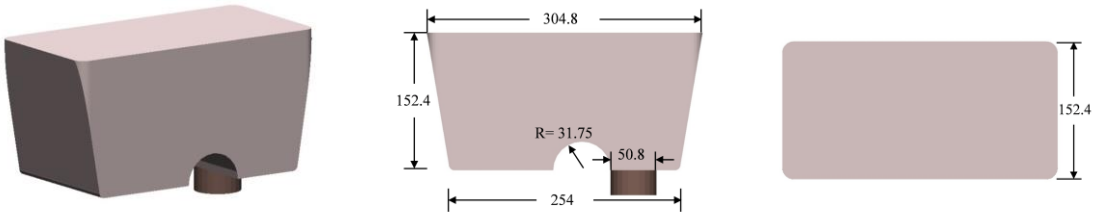

(a) (b) (c)

Figure 5.14 Geometry of the offset step pouring basin: (a) isometric view, (b) front view, and (c) top view. All dimensions in mm.

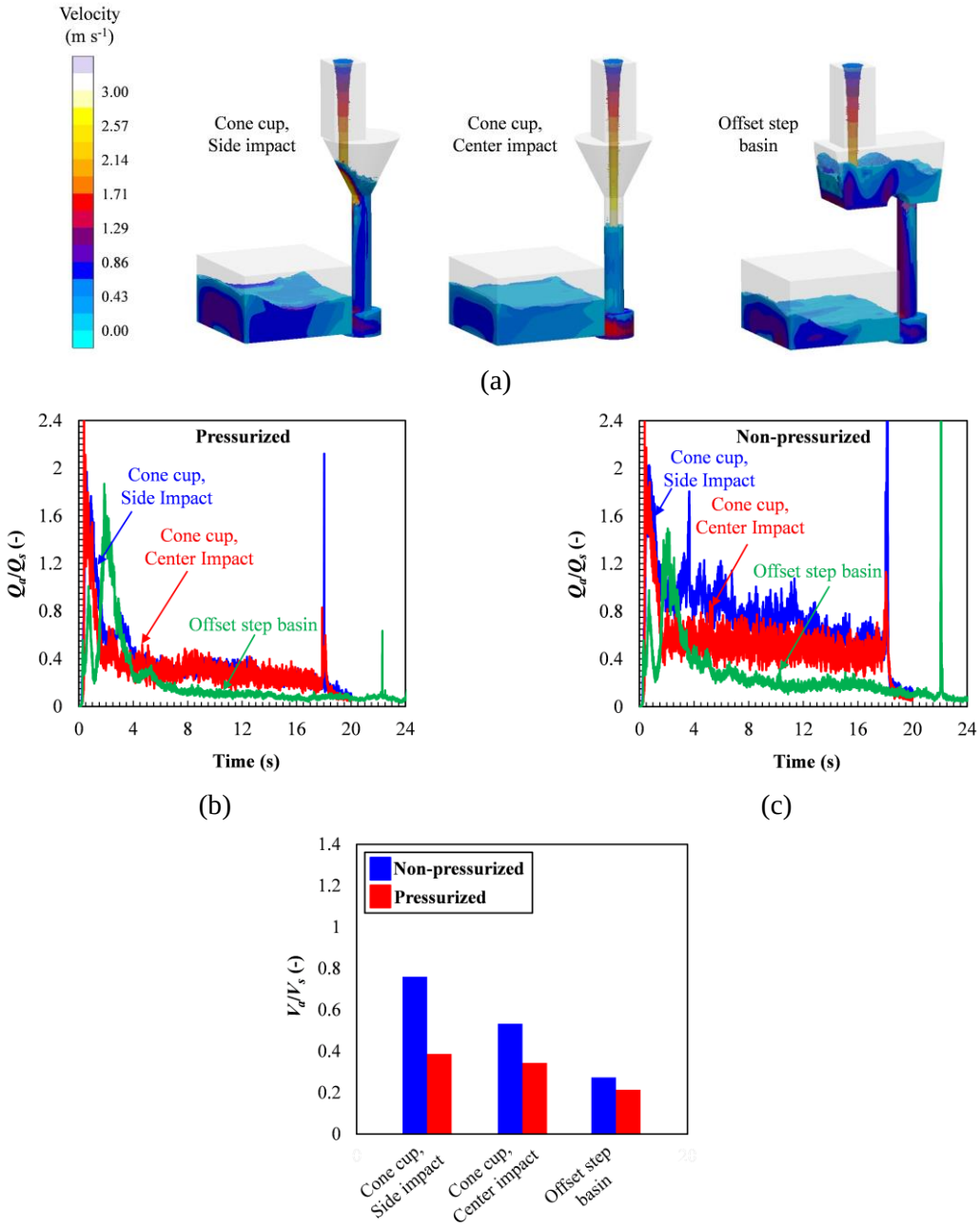

Figure 5.15 Comparison of the offset step pouring basin with the cone pouring cup (side and centre impact) for $Q_s = 1\times10^{-3}$ m^3 s^{-1} and $H = 203.2$ mm: (a) velocity contours at $t = 10$ s for a pressurized gating system, (b) variation of the relative air entrainment rates for a pressurized gating system, (c) variation of the relative air entrainment rates for a non-pressurized gating system, and (d) predicted total relative entrained air volumes.

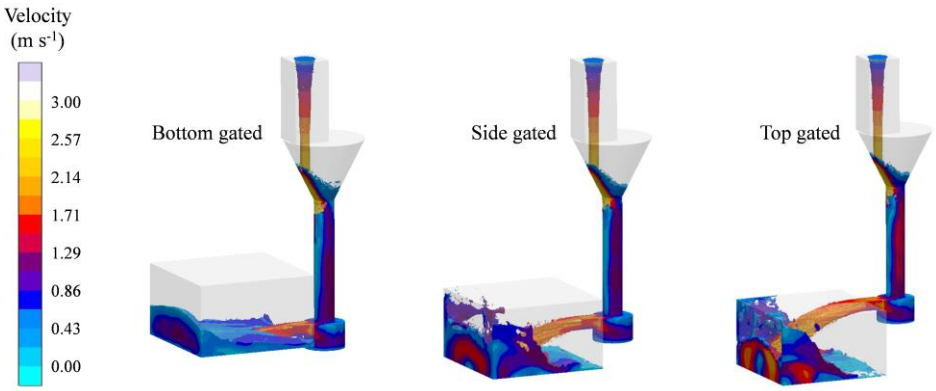

(a)

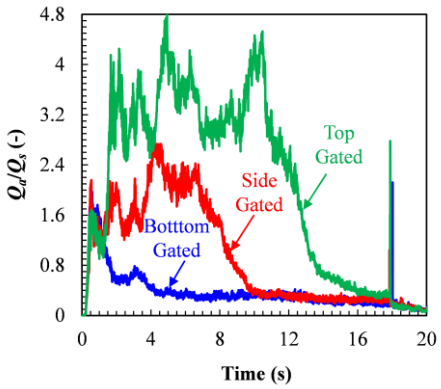

(b)

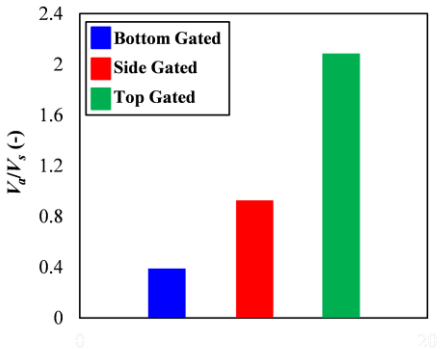

(c)

Figure 5.16 Effect of the ingate location for $Q_s = 1\times10^{-3}$ m^3 s^{-1} ($t_{fill} = 20$ s), $H = 203.2$ mm, pressurized gating system, cone pouring cup, and side impact: (a) velocity contours at a time of 4 s, (b) variation of the relative air entrainment rates, and (c) comparison of the predicted total relative entrained air volumes.

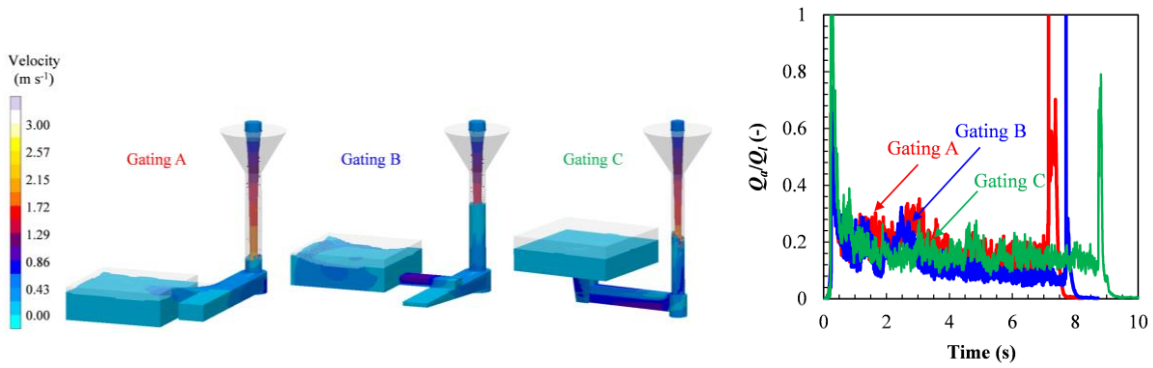

(a)

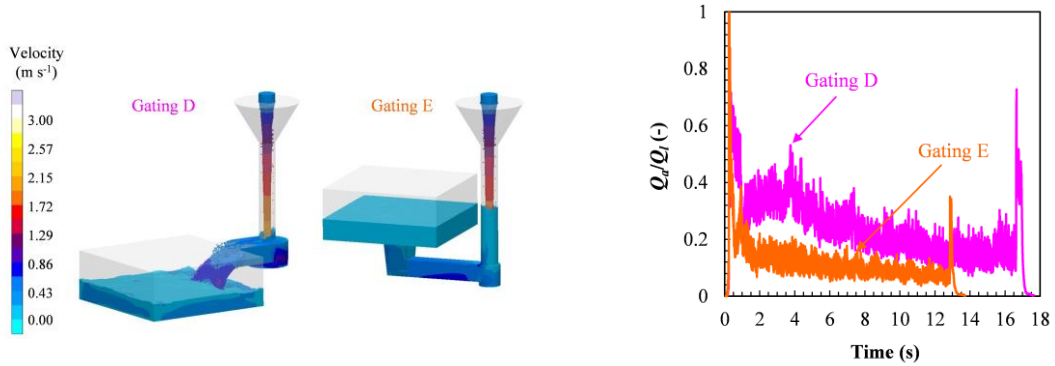

(b)

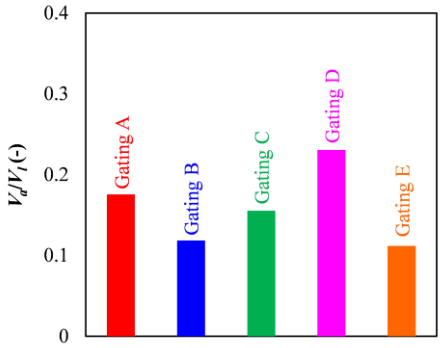

(c)

Figure 5.17 Comparison of the entrained air for different gating systems studied in ductile iron experiments, velocity contours at $t = 6\,\text{s}$ and variation of the relative air entrainment rates for: (a) gatings A, B and C, (b) gatings C and D, and (c) relative air entrainment volume for different gating systems.

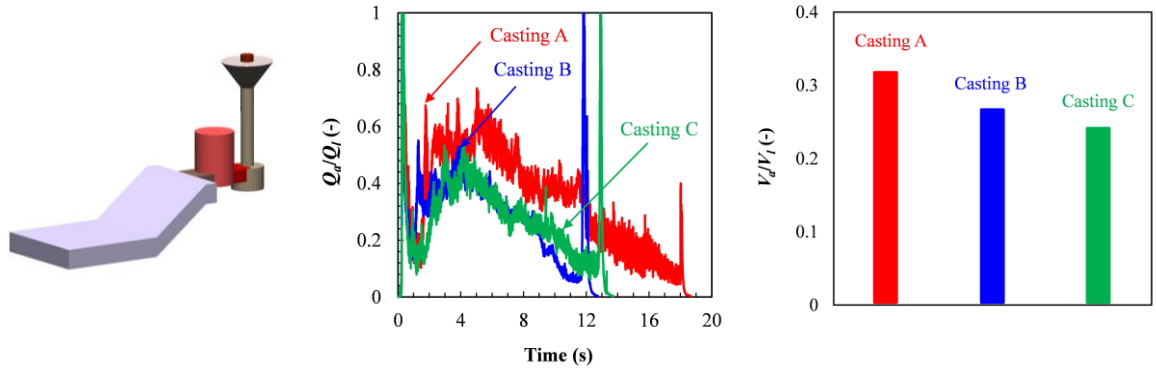

(a)

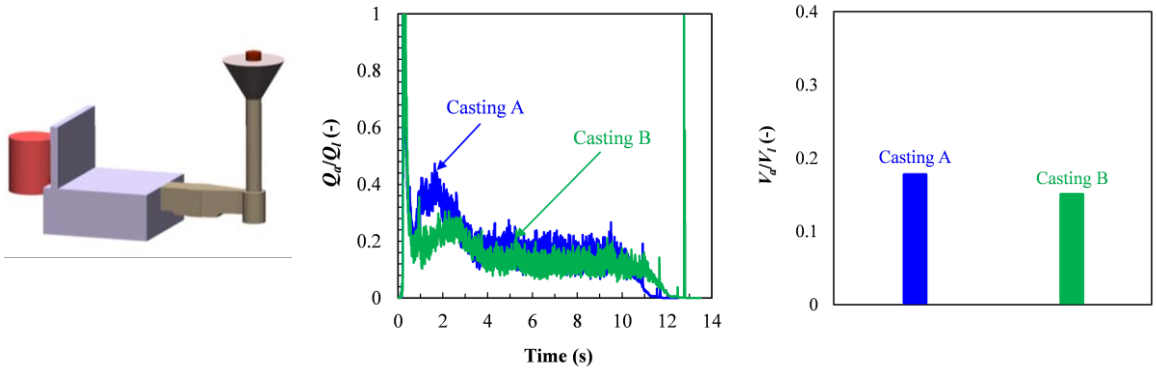

(b)

Figure 5.18 Comparison of the entrained air for casting with (a) inclined surface, and (b) thin section; left- variation of the relative air entrainment rates, and right- relative air entrainment volume.

CHAPTER 6: CONCLUSIONS AND FUTURE WORK

6.1 Conclusions

In the current study, the formation of oxide inclusion during pouring of metal castings is studied. Experiments were conducted for studying dross formation in ductile iron castings. The effect of different gating systems on the formation of dross inclusions was studied. Results show that pouring the liquid iron quiescently and with less free surface turbulence reduces the dross inclusions. In addition, castings with a variety of surface orientation and section thicknesses were poured to investigate the final location of oxide inclusions in ductile iron castings. For the castings with inclined surface, the majority of dross inclusions stick to mold walls before the returning wave reaches the inclined part of the casting. In castings with thin sections, dross inclusions are not able to enter the thin section; while the majority of inclusions stick to the mold wall at the joint location of the thin section and heavy section, few inclusions are swept away towards the ingate and the riser. Results also indicate that the addition of a filter in the runner blocks a large portion of the inclusions originated from the ladle and the gating system from entering the mold cavity. The density and molecular weights of oxide inclusions is calculated based on the chemical composition of the inclusions.

A sub-grid model is developed for predicting the air entrainment during filling of the mold cavity. In this model, the local volumetric air entrainment rate is a function of the turbulent kinetic energy and the magnitude of the normal velocity gradient at the liquid-air interface. First, an in-house solver was developed in OpenFOAM to predict the two phase bubbly flow and the entrained air at free surface discontinuities. The model was then implemented into a casting filling simulation code to calculate local air entrainment rates during mold filling. The model is validated through comparisons with experimental air entrainment measurements for a plunging water jet. Using a single

model coefficient, a good agreement is achieved between the predicted values and the measurements for different liquid jet velocities, diameters and turbulence intensities.

Once the air entrainment is calculated, the entrained air volume is converted to inclusion volume and an equivalent inclusion diameter is calculated. An inclusion is generated at the location of entrained air with the calculated diameter and density. The inclusions are then allowed to advect with the liquid metal to their final location. The final location of inclusions is determined by solving the equation of motion at each time step for each inclusion. An agglomeration algorithm is defined for reaching larger inclusions and further avoiding the generation of large number of small inclusions.

The air entrainment model is then validated for water modeling experiments. Overall good agreement is achieved between the predicted and the measured relative air entrainment volumes. Additionally, the model is applied to study the effect of different gating designs and pouring parameters on the air entrainment. Results of these studies indicate that reducing the total head height and filling time, use of an offset step pouring basin and a pressurized bottom gated filling system reduce the air entrainment during filling. Moreover, the results of the water modeling study indicate that in bottom pour ladles, adding a nozzle extension to the end of the nozzle reduces the air entrainment during filling, and that the nozzle opening has the most significant effect upon the air entrainment. A throttled nozzle applies large turbulence intensity to the flow at the nozzle exit, markedly increasing the air entrainment volume. Evaluating different filling systems solely based on a single quantitative data is essential to set an objective for the design of filling systems in metal castings. Based on the predicted relative air entrainment volume, the present model allows foundries to evaluate different gating designs and pouring parameters before the first casting is poured.

6.2 Future work

The air entrainment model is shown to be capable in predicting the free surface turbulence during pouring of metal castings. The developed model must be further validated for liquid metals. The entrainment coefficient is the key parameter which must be calibrated for liquid aluminum, iron and steel. The accurate value of entrainment coefficient is necessary to predict the correct volume of entrained air, hence oxide inclusion for each liquid. Further experiments are required to show the dependency of the entrainment coefficient to liquid properties.

In the studied cases, air entrainment and oxide inclusion formation is considered only during the filling stage, and the effect of inclusions formed prior to pouring is neglected. This is not the case in production castings, where significant oxide inclusions are formed prior to pouring. Future work must account for the entrained air during tapping the liquid metal from furnace to the ladle.

Initial steps were taken to model the formation and motion of oxide inclusions during mold filling. The model was implemented in OpenFOAM, and a number of simple configurations were simulated. After the inclusion generation and tracking model is implemented in the casting simulation software, the model capabilities should be investigated for production castings. There are still major issues regarding modeling oxide inclusion generation and motion, which require further investigation and experimental studies.

While the oxide inclusions are individually unique in shape and density, the developed model assumes a spherical shape and a constant density for all inclusions. In all the computational models, the shape of the oxide inclusions remains as spherical which contradicts experimental findings. In addition, the present model tracks the generated oxide inclusions until the end of pouring, and it does not account for the motion of these inclusions from the end of pouring to the end of solidification. Future

studies must account for the motion of the inclusions after the pouring is finished. This is particularly important for predicting the accurate final location of inclusions. Among the challenging issues is modeling the particle-particle and particle-wall interactions. The developed inclusion model agglomerates inclusions once they become in contact with each other, and assumes the inclusions stick to mold walls once they come in contact with the walls. This is not a proven assumption, and further experiments are required to observe the behavior of inclusions and the key parameters affecting the inclusion motion in the vicinity of mold walls. Moreover, the effect of porous filters on oxide inclusions requires more experiments. Commercial casting softwares usually block a certain percentage of inclusions at the filters or block inclusions above a certain size. This contradicts the results of some studies which have shown that a number of large inclusions are shredded as they pass filters. These parameters are important in predicting the final size and location of oxide inclusions.

REFERENCES

[1] Campbell J. Complete casting handbook: metal casting processes, metallurgy, techniques and design. Butterworth-Heinemann, 2015.

[2] Melendez AJ, KD Carlson, and C Beckermann. "Modelling of reoxidation inclusion formation in steel sand casting." *International Journal of Cast Metals Research* 23, no. 5 (2010): 278-288.

[3] Belden J, S Ravela, T Truscott, and A Techet. "Bubble fields in 3D (no glasses necessary)." In APS Division of Fluid Dynamics Meeting Abstracts. 2011.

[4] Ma J, AA Oberai, DA Drew, RT Lahey Jr, and MC Hyman. "A comprehensive sub-grid air entrainment model for RaNS modeling of free-surface bubbly flows." *The Journal of Computational Multiphase Flows* 3, no. 1 (2011): 41-56.

[5] Lin TJ, and HG Donnelly. "Gas bubble entrainment by plunging laminar liquid jets." *AIChE Journal* 12, no. 3 (1966): 563-571.

[6] Bińk AK. "Gas entrainment by plunging liquid jets." *Chemical Engineering Science* 48, no. 21 (1993): 3585-3630.

[7] Ervine DA, E McKeogh, and EM Elsawy. "Effect of turbulence intensity on the rate of air entrainment by plunging water jets." Proceedings of the Institution of Civil Engineers 69, no. 2 (1980): 425-445.

[8] Chanson H. "Turbulent air–water flows in hydraulic structures: dynamic similarity and scale effects." *Environmental fluid mechanics* 9, no. 2 (2009): 125-142.

[9] Sene KJ. "Air entrainment by plunging jets." *Chemical Engineering Science* 43, no. 10 (1988): 2615-2623.

[10] Cummings PD, and H Chanson. "Air entrainment in the developing flow region of plunging jets—Part 1: Theoretical development." *Journal of Fluids Engineering* 119, no. 3 (1997): 597-602.

[11] Van de Sande E, and JM Smith. "Jet break-up and air entrainment by low velocity turbulent water jets." *Chemical Engineering Science* 31, no. 3 (1976): 219-224.

[12] Brattberg T, and H Chanson. "Air entrapment and air bubble dispersion at two-dimensional plunging water jets." *Chemical Engineering Science* 53, no. 24 (1998): 4113-4127.

[13] Ma J, AA Oberai, DA Drew, RT Lahey, and FJ Moraga. "A quantitative sub-grid air entrainment model for bubbly flows–plunging jets." *Computers & Fluids* 39, no. 1 (2010): 77-86.

[14] Wanstall C, J Griffin, and CE Bates. "Water Modeling of Steel Pouring Practices." *In 47th Steel Founders' Society of America National Technical & Operating Conference*, Chicago, Illinois. 1993.

[15] Bates CE, and J Griffin. "Clean Cast Steel Technology." Research report no. 106, Steel Founders' Society of America (SFSA), Crystal Lake, IL, USA, 1994.

[16] Kuyucak S. "Sponsored Research: Clean steel casting production-Water modeling studies of bottom-pouring ladle operations." *Transactions of the American Foundrymen's Society* 114 (2006): 811-818.

[17] Afsharpour M, B Homayun, and SMA Boutorabi. "Water modelling of effects of pouring basin and sprue geometry on entrance of air bubbles into mould." *Materials Science and Technology* 30, no. 2 (2014): 152-159.

[18] Moraga FJ, PM Carrica, DA Drew, and RT Lahey. "A sub-grid air entrainment model for breaking bow waves and naval surface ships." *Computers & Fluids* 37, no. 3 (2008): 281-298.

[19] Shi F, JT Kirby, and G Ma. "Modeling quiescent phase transport of air bubbles induced by breaking waves." *Ocean Modelling* 35, no. 1 (2010): 105-117.

[20] Ma G, F Shi, and James T. Kirby. "A polydisperse two-fluid model for surf zone bubble simulation." Journal of Geophysical Research: *Oceans* 116, no. C5 (2011).

[21] Xiang M, SCP Cheung, JY Tu, and WH Zhang. "A multi-fluid modelling approach for the air entrainment and internal bubbly flow region in hydraulic jumps." *Ocean Engineering* 91 (2014): 51-63.

[22] Ma J, AA Oberai, RT Lahey, and DA Drew. "Modeling air entrainment and transport in a hydraulic jump using two-fluid RANS and DES turbulence models." *Heat and mass transfer* 47, no. 8 (2011): 911.

[23] Ma J, AA Oberai, DA Drew, and RT Lahey. "A Two-Way Coupled Polydispersed Two-Fluid Model for the Simulation of Air Entrainment Beneath a Plunging Liquid Jet." *Journal of fluids engineering* 134, no. 10 (2012): 101304.

[24] Ma J, AA Oberai, MC Hyman, DA Drew, and RT Lahey. "Two-fluid modeling of bubbly flows around surface ships using a phenomenological subgrid air entrainment model." *Computers & Fluids* 52 (2011): 50-57.

[25] Hirt CW. "Modeling turbulent entrainment of air at a free surface." Flow Science, Inc (2003).

[26] Souders DT, and CW Hirt. "Modeling entrainment of air at turbulent free surfaces." In Critical Transitions in Water and Environmental resources Management, pp. 1-10. 2004.

[27] Castro AM, J Li, and PM Carrica. "A mechanistic model of bubble entrainment in turbulent free surface flows." *International Journal of Multiphase Flow* 86 (2016): 35-55.

[28] Campbell J. "Entrainment defects." *Materials science and technology* 22, no. 2 (2006): 127-145.

[29] Lai NW, WD Griffiths, and J Campbell. "Modelling of the potential for oxide film entrainment in light metal alloy castings." Modeling of Casting, Welding and Advanced Solidification Processes- X 2003 (2003).

[30] Reilly C, NR Green, and MR Jolly. "The present state of modeling entrainment defects in the shape casting process." *Applied Mathematical Modelling* 37, no. 3 (2013): 611-628.

[31] Cuesta R, A Delgado, A Maroto, and D Mozo. "Numerically modeling oxide entrainment in the filling of castings: The effect of the webber number." *JOM Journal of the Minerals, Metals and Materials Society* 58, no. 11 (2006): 62-65.

[32] Yang X, X Huang, X Dai, J Campbell, and J Tatler. "Numerical modelling of entrainment of oxide film defects in filling of aluminium alloy castings." *International Journal of Cast Metals Research* 17, no. 6 (2004): 321-331.

[33] Reilly C, NR Green, MR Jolly, and JC Gebelin. "The modelling of oxide film entrainment in casting systems using computational modelling." *Applied Mathematical Modelling* 37, no. 18-19 (2013): 8451-8466.

[34] Dai X, M Jolly, X Yang, and J Campbell. "Modelling of liquid metal flow and oxide film defects in filling of aluminium alloy castings." In IOP Conference Series: Materials Science and Engineering, vol. 33, no. 1, p. 012073. IOP Publishing, 2012.

[35] Sato Y., I Ohnaka, JD Zhu, and H Yasuda. "Modeling of oxides entrapment during mould filling of Al-alloy castings." In D7th Asian Foundry Congress, *The Chinese Foundrymens Association*, Tapei. 2001.

[36] Yue Y. "Modelling of the effects of entrainment defects on mechanical properties in Al-Si-Mg alloy castings." PhD diss., University of Birmingham, 2014.

[37] Gagne M, M Paquin, and P Cabanne. "Dross in ductile iron: source, formation and explanation." *Indian foundry journal* 57, no. 9 (2011): 39-44.

[38] Heine RW, and CR LOPER JR. "Dross formation in the processing of ductile cast iron." *Transactions of the American Foundrymen's Society* 74 (1966): 274-280.

[39] Trojan PK, P Cuichelaar, W Bargeron, and R Flinn. "An intensive investigation of dross in nodular cast iron." *Transactions of the American Foundrymen's Society* 76 (1968): 323-333.

[40] Latona, MC, HW Kwon, JF Wallace, and JD Voss. "Factors influencing dross formation in ductile iron castings.(retroactive coverage)." *Transactions of the American Foundrymen's Society* 92 (1984): 881-906.

[41] Askeland DR, PK Trojan, and R Flinn. "Dross Forming Reactions in the System Mg-Si-O in Ductile Fe." *Transactions of the American Foundrymen's Society* 80 (1972): 349-358.

[42] Birks N, GH Meier, and FS Pettit. Introduction to the high temperature oxidation of metals. Cambridge University Press, 2006.

[43]Heine RW. "Major aspects of processing cast irons." In Ninety-Eighth Annual Meeting of the American Foundrymen's Society: *Transactions of the American Foundrymen's Society* 80 (1994): 985-1002.

[44] Roedder E. "Silicate melt systems."*Physics and Chemistry of the Earth* 3 (1959): 224-297.

[45] Alva J. "An understand source of dross in ductile (SG) iron castings." *Foundry trade journal international* 185 (2011): 317-320.

[46] Fuller AG. "Dross defects in nodular iron castings'." *BCIRA Journal of Research and Development* 7 (1958): 268.

[47] Aksay IA, JA Pask, and RF Davis. "Densities of SiO_2-Al_2O_3 Melts." *Journal of the American Ceramic Society* 62, no. 7-8 (1979): 332-336.

[48] Anderson OL, and K Zou. "Thermodynamic functions and properties of MgO at high compression and high temperature." *Journal of Physical and Chemical Reference Data*19, no. 1 (1990): 69-83.

[49] Touloukian YS. Thermophysical Properties of High Temperature Solid Materials. Volume 4. Oxides and Their Solutions and Mixtures. Butterworth-Heinemann, 1966.

[50] MAGMAsoft® v4.6, Magma GmbH, Aachen, Germany.

[51] Hunt J CR. "Turbulence structure and turbulent diffusion near gas-liquid interfaces." In Gas transfer at water surfaces, pp. 67-82. Springer Netherlands, 1984.

[52]Kobus H. "Local air entrainment and detrainment." Symposium on Scale Effects in Modelling Hydraulic Structures (1984).

[53] OpenFOAM® v2.3.1 (OpenCFD ltd. www.openfoam.org)

[54] Deshpande SS. "A Computational Study of Multiphase Flows." PhD diss., University of Wisconsin- Madison, 2014.

[55] Boyd JWR, and J Varley. "Acoustic emission measurement of low velocity plunging jets to monitor bubble size." *Chemical Engineering Journal* 97, no. 1 (2004): 11-25.